



DISSERTATION

Performance of piezoelectric MEMS resonators in liquids

zur Erlangung des akademischen Grades
Doktor der technischen Wissenschaften (Dr.techn.)

am Institut für Sensor- und Aktuatorssysteme
der Fakultät für Elektrotechnik und Informationstechnik
der Technische Universität Wien

Dipl.-Ing. Georg Pfusterschmied
Matrikelnummer: 1028200

Wien, 2018

Verteidigung: Wien, 19. April 2018

Betreuer: Univ.-Prof. Dr.rer.nat. Ulrich Schmid
Technische Universität Wien, Österreich

Gutachter: Univ.-Prof. Dr.mont. Mario Kupnik
Technische Universität Darmstadt, Deutschland

Univ.-Prof. Dr.sc. Silvan Schmid
Technische Universität Wien, Österreich

Acknowledgements

First of all, I would like to thank my doctoral supervisor Prof. Ulrich Schmid, who gave me the opportunity to work in his research group at the Institute of Sensors and Actuator Systems at TU Wien. This thesis would not have been possible without his full support and his familiar treatment by guiding me throughout my thesis. My deepest appreciation is directed to the postdoctoral researchers in our group Michael Schneider, Achim Bittner and Daniel Platz for sharing their expertise and always bringing me back on the right track.

Within this thesis 3011 resonators have been fabricated. Thousands of optical and electrical measurements have been performed in vast quantities of liquids. Tones of paper have been saturated with ink, dozens heads have been spinning and years have been spent on the data evaluation. This extraordinary achievements can never be the work of just one person but rather it is the fruit of so many people. I would like to thank my colleges and good friends Elisabeth Wistrela, Manuel Gillinger, Markus Leitgeb, Wolfgang Steindl and Martin Kucera for their professional and private support during this time. Very special thanks is directed to the good souls of the institute Martina Nuhsbaumer and Andreas Astleitner (*"Long live the Viennese snide humour"*). Above all, I would like to thank my mother Karin, father Gerhard, my brother Jürgen and Theresa for their patience and encouragement.

Abstract

Within this thesis, the optimization of piezoelectrically excited MEMS resonators for most precise sensing in liquid environment is targeted, ranging from 1 to 700 mPa·s (for comparison: typical engine oil SAE 15W40 has 390 mPa·s at room temperature). The advanced resonator design enables both, the actuation of the fundamental vibration as well as higher order modes. Additionally, a tailored electrode design for enhanced electrical read-out of specific modes facilitates high output signals. To further improve this sensing concept, the anchor structures of the resonators are optimized such that the nodal lines of the particular mode match the position of the mechanical fixtures, thus minimizing any losses to the silicon frame and enabling a quasi-free vibration.

To quantify these concepts experimentally, MEMS resonators are fabricated using silicon micromachining technology including piezoelectric aluminium nitride as active material. The tailored read-out mechanism is utilized to excite and sense the first 10 orders of a special transversal bending mode named roof tile-shaped mode, which are electrically and optically characterized in air and several liquids by key device parameters such as the resonance frequency, the quality factor and the electrical conductance peak height in resonance. With this approach, a significantly enhanced performance is achieved for higher order modes, where a decrease in viscous damping of the fluid leads to increased values of the quality factor. Additionally, the signal to noise ratio (SNR) is enhanced by a factor of 50, when comparing the 10th with the 1st order mode. The implementation of an optimized support further increases the SNR by about 20% independent of the viscosity of the fluid. These three areas of optimization are of particular interest for sensing applications targeting either physical properties of high viscous liquids with dynamic viscosities > 500 mPa·s, or any mass changes on the resonator surface. In the last chapter of this thesis a potential application for this highly optimized sensor elements is introduced. Thereby,

the piezoelectric excited resonators are used to monitor the minimal physical changes during grape must fermentation, enabling the distinction between ordinary and potential stuck fermentation processes.

Kurzfassung

Im Rahmen dieser Arbeit wurden piezoelektrisch angeregte MEMS Resonatoren für Anwendungen in der Flüssigkeitssensorik in einem Bereich von 1 bis 700 mPa·s (zum Vergleich: SAE 15W40 als typisches Motoröl hat 390 mPa·s bei Raumtemperatur) optimiert. Das bevorzugte Resonator-Design ermöglicht sowohl eine Anregung der Grundschiwingung als auch Schwingungen höherer Ordnung. Es kommt ein maßgeschneiderter Ansatz zur Auslegung der Elektrodenstruktur zum Einsatz, um beim Auslesen der elektrischen Sensorsignale eine möglichst hohe Sensitivität für jede Schwingungsmoden zu gewährleisten. Zusätzlich wird die mechanische Aufhängung der Mikroresonatoren an die Knotenlinien der jeweiligen Schwingungsform angepasst, um Ankerverluste ins Substrat zu minimieren und einen minimal von der Aufhängung beeinflussten Schwingungszustand zu erreichen.

Um diese Optimierungsansätze experimentell zu untersuchen, wurden MEMS Resonatoren mit Standard-Prozessen der Silizium-Mikromechanik hergestellt und in Luft sowie in verschiedenen Flüssigkeiten elektrisch und optisch charakterisiert. Die dabei zum Einsatz kommende piezoelektrische Aluminiumnitrid-Schicht ermöglicht sowohl die Anregung als auch das elektrische Auslesen wichtiger, bauelemente-bezogener Kenngrößen, wie die Resonanzfrequenz, den Gütefaktor und die Konduktanzsignalthöhe in Resonanz. Im Zuge der Resonatorcharakterisierung zeigte sich, dass höhere Schwingungsmoden deutlich weniger von der Viskosität der umgebenen Flüssigkeit gedämpft werden und dadurch höhere Gütefaktoren aufweisen. Das maßgeschneiderte Ausleseverfahren sorgt für eine Erhöhung des Signal-zu-Rauschabstandes (SNR) um ein 50-faches für die zehnte Schwingungsordnung im Vergleich zur Grundschiwingung. Des Weiteren konnte durch gezieltes Optimieren der Resonatoraufhängung der SNR-Wert um weitere 20% erhöht werden. Diese drei Optimierungsansätze sind nicht nur für Sensorikanwendungen in hochviskosen Flüssigkeiten mit einer dynamischen

Viskosität $> 500 \text{ mPa}\cdot\text{s}$, sondern grundsätzlich für hochgenaue Messungen von z.B. Massenänderungen des Sensors in Flüssigkeiten und in Gasen von großer Bedeutung.

Im abschließenden Kapitel dieser Dissertation wird eine vielversprechende Anwendung dieser optimierten Sensorelemente vorgestellt. Die piezoelektrisch angeregten MEMS Resonatoren werden verwendet, um minimale Änderungen insbesondere in der Dichte während des Gärungsprozesses von Trinkwein zu detektieren und dadurch mögliche fehlgeleitete Gärungsprozesse frühzeitig zu erkennen.

Contents

Acknowledgements	iii
Abstract	v
Kurzfassung	vii
Contents	ix
1 Introduction	1
1.1 Motivation	2
1.2 Extent to previous works	4
1.3 Outline of the thesis	5
2 Fundamentals of resonators	7
2.1 Single degree of freedom (SDOF) system	7
2.2 Electro-mechanical analogy	13
2.3 Damping mechanisms	14
2.4 Free vibrational bending of beams	15
3 Piezoelectricity	19
3.1 History	20
3.2 Fundamentals	21
3.3 Material aspects	22
4 Fluid-Structure interaction	25
4.1 Reynolds number	25
4.2 Temperature dependence of fluid properties	29
5 Fabrication	31

6	Actuation and sensing techniques	35
6.1	Piezoelectric actuation and sensing	35
6.2	Laser Doppler vibrometry	41
7	Influence of the mode order	45
7.1	Introduction	46
7.2	Terminology: Responsivity and sensitivity	46
7.3	Design considerations and methods	47
7.4	Electrical characterization in liquids	48
7.5	Conclusions	58
8	Influence of the anchor design	61
8.1	Design considerations	62
8.2	Electrical and optical characterization in air	63
8.3	Electrical characterization in liquid media	65
8.4	Conclusions	67
9	Influence of the quasi free-free support	69
9.1	Design considerations	70
9.2	Mode shape analysis	73
9.3	Electrical characterization in liquid media	76
9.4	Conclusions	78
10	Wine fermentation monitoring	79
10.1	Introduction	79
10.2	Experimental details	81
10.3	Results	86
10.4	Conclusions	92
11	Conclusions and Outlook	95
11.1	Conclusions	95
11.2	Outlook	96
A	Supplemental materials	97
A.1	Tables of the fluid properties	97
A.2	Electrical conductivity values	102
A.3	Table collection for Chapter 7	103

<i>CONTENTS</i>	xi
A.4 Program code for sensitivity estimation	106
List of Figures	107
List of Tables	113
List of Abbreviations	117
Bibliography	127

Chapter 1

Introduction

Parts of this chapter have already been published in Ref. [1]

Transducers, converting energy from one form to another, are as old as life itself. The human eyes and ears are two prominent examples, where light or sound waves are converted into electrical signals which are then transmitted to the human brain. Transducers, receiving and responding to a signal or stimulus from a physical system, are named sensors [2]. Others, that convert control signals to movement or other physical quantities, as it is the case for engines or pumps, are termed actuators [3]. The miniaturization of such devices and the progress in micro and nanoelectronics over the last decades have substantially contributed to the basis of today's information and communication technology, penetrating our everyday life. For the field of miniaturized sensors and actuators, this development started more than 30 years ago, when Petersen studied the mechanical properties of silicon [4], which put the research field on micro-electromechanical system (MEMS) into motion. From that on, electrical and mechanical components were merged into one single miniaturized device or even system and can nowadays be found in applications such as airbag systems [5] or cochlear implants [6], just to mention two most prominent success stories which are available as products since many years.

The measurand, which is the particular quantity subject to the measurement e.g. distance, mass, temperature, acceleration or pressure, can be determined using different sensing techniques. Capacitive approaches are regularly used in surface micromachined devices, such as in touch displays [7], where minimal changes in the distance between plates are detected. In contrast, piezo-resistive read-out is typically implemented in bulk micromachined devices applying a

Wheatstone bridge configuration for strain sensing in e.g. pressure sensors [8]. And optical or laser-based sensing is widely used in diagnostics such as atomic force microscopy [9]. All these techniques, have their specific advantages and drawbacks. As for instance, capacitive tactile sensors are known as very sensitive devices but with non-linear behavior including pull-in effects and the requirement of an external supplying voltage [10]. Piezo-resistive approaches are known as cheap in production but tend to show a high cross-sensitivity to temperature [11]. Optical read-outs instead are considered to be very accurate and flexible, but with the drawback of making the measurement setup bulky and expensive, thus making a flexible integration almost impracticable [12]. Therefore, the deployed sensing technique has to be cautiously chosen with the specific application in mind. A very versatile approach is named piezoelectric sensing, where piezoelectric materials such as aluminium nitride (AlN) respond to mechanical strain with the generation of electrical charges and is mainly used for dynamic-mode applications. A large variety of piezoelectric materials, lower temperature dependence in the standard automotive temperature range (-40-125°C) compared to piezo-resistive approaches and a high integration potential are only a few key benefits. Compared to the capacitive sensing technique, an external supplying voltage is not a prerequisite, which qualifies piezoelectric sensing for low power or even ultra-low power applications. Probably the most advantageous aspect is the reversibility of the piezoelectric effect. For that reason, piezoelectric materials are able to serve for both sensing and acting purposes at the same time, thus making the integration of so called bi-direction transducers in a MEMS device for a compact design most attractive.

1.1 Motivation

Generally speaking, with decreasing dimensions of objects, the surface to volume ratio increases drastically and surface related effects become more and more dominant, which usually increases the response¹ of a sensor [13]. It is therefore of particular interest to further decrease the dimensions of sensing elements down to the nanometer range. Such systems, analog to MEMS, are named nanoelectromechanical systems (NEMS) and enable the detection of single molecules [14] or proteins [15]. Especially, dynamic-mode resonators have

¹Sensor response or sensor responsivity: Ratio of sensor output to sensor input.

become a reliable platform for various sensing applications, such as density and viscosity sensing of liquids [16–22], pressure level sensing in gaseous environment [23] or so called bio-recognition agents [24–28]. The latter approach is a chemical sensing procedure, where bindings from e.g. an analyte to a chemically activated resonator surface cause a detectable mass change of the resonators. So called fluidic channel resonators [29, 30], in which the fluid passes through a fluidic channel in the moving part of the resonator, are beneficial due to their high precision capabilities especially for molecular detection [31] or blood coagulation [32]. Only tiny amounts of liquid (e.g. 5 μL [33]) are needed and masses can be detected down to the attogram-regime [34].

In most of these sensing techniques only the resonator is micro- or nanoscaled, whereas the external actuation hardware is macroscopic what makes the integration into portable systems impracticable. A miniaturization of the actuator, however, is often targeted, but challenging to realize, as with a decrease in size also the actuator potential² decreases. This is of particular interest for piezoelectric transducers, where the sensing element also serves as actuator implying a contrary tendency of the sensor responsivity and the actuator potential over size as illustrated in Figure 1.1. For these systems, the reduction in size is often self-defeating and other mechanisms have to be found to optimize sensing and actuation performance, simultaneously. Especially for sensing applications in liquid environments, the miniaturization of piezoelectric resonators leads to actuation problems, because with decreasing dimensions viscous effects become more and more dominant and causes a high damping of any vibrational movements [35]. Therefore it is of particular interest, how both, sensor and actuator performance of piezoelectric transducers immersed in a liquid can be improved at the same time to achieve compact and portable devices with high output signals.

²Actuator potential \mathcal{P} : Ratio of actuation output to actuation input.

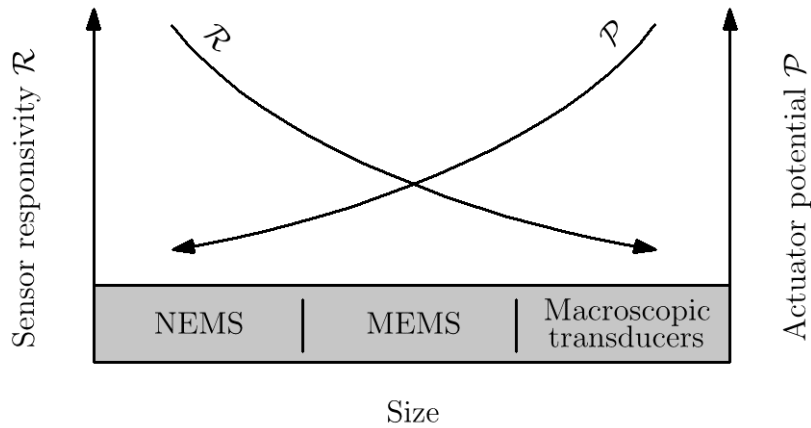


Figure 1.1: Comparison of the sensor responsivity \mathcal{R} and the actuator potential \mathcal{P} for NEMS, MEMS and macroscopic transducers.

1.2 Extent to previous works

Basically, fundamental concepts investigated in this work are motivated by the outcomes presented in the thesis of Kucera [36]. To provide a clear view on the achievements presented in the present thesis, the most relevant aspects in Kucera's work are discussed and the most important conclusions are summarized in this section.

Kucera fabricated and characterized differently sized piezoelectric aluminium nitride-resonators in liquid media. One main part was to study the performance of laterally vibrating resonators, where he clearly demonstrated the size dependent performance of piezoelectric MEMS resonators in liquids [37]. Within this study, Kucera observed special transversal bending modes with superior quality factors compared to standard out of plane modes [38]. He named this class roof tile-shaped modes, due to their specific shape. Furthermore, he used the resonators, designed for the in-plane study [37] for characterizing the first 10 orders of the roof tile-shaped mode [39]. Quality factors above 300 were obtained for the 10th order mode in deionized water. However, significant charge compensation effects occurred for higher order modes, resulting in low electrical conductance peak values so that resonator characterization was only possible in low viscous liquids such as deionized water. To exploit the full potential of the roof tile shaped modes and to ensure applications in high viscous liquids such as engine oils, Kucera proposed in the outlook section a redesign of the piezo-

electric MEMS resonators including a customized electrode patterning for each mode order. Furthermore, he suggested a specific design of the anchor plate geometry to enhance the mechanical surface stress in the suspended plate.

1.3 Outline of the thesis

It is the objective of this thesis to critically address the impact of the following three design considerations on the performance for self-actuated, piezoelectric MEMS resonators in liquid environments.

- Consideration of higher order modes
- Consideration of tailored electrodes for each mode
- Consideration of different supported resonators

In Chapter 2 the fundamental theory of resonators is derived by means of a single degree of freedom (SDOF) system including the definitions of fundamental parameters such as the damping ratio, the quality factor and different damping regimes and mechanisms. The Euler-Bernoulli beam theory is introduced and used to calculate the mode shapes for beams with different clamping conditions. In Chapter 3, the mechanism of piezoelectricity is explained in detail with the special focus on aluminium nitride. In Chapter 4 the fluid-structure interaction of MEMS resonators is discussed by means of the Reynolds number. A well-established theoretical model is introduced to predict the fluid-structure interaction of resonators operating at higher order modes. In Chapter 5, a brief review of the fabrication process is given including the most important manufacturing steps, followed by the deployed actuation and sensing techniques in Chapter 6. The impact of the excitation at higher mode orders on the responsivity and sensitivity of the fabricated resonators are critically studied in Chapter 7. Additionally, the importance of a tailored electrode design is pointed out and compared to non-ideal actuation. In Chapter 8, the importance of an optimized mechanical support of resonators even when targeting the performance in liquid environments is investigated for resonators with clamped-free, clamped-clamped and quasi free-free support boundary conditions. Because of the great potential of quasi free-free supported resonators, this type of clamping is investigated in detail for higher order modes and the corresponding results

are presented in Chapter 9. Finally, a potential application for the investigated sensing concept is introduced in Chapter 10. Thereby, the gathered information about the performance of self-actuated piezoelectric MEMS resonators in liquid environments are utilized to realize a sensor element, which is capable to monitor minimal physical changes during the fermentation process in wine making. A summary and an outlook are given in Chapter 11.

Chapter 2

Fundamentals of resonators

In this chapter the mathematical basics to predict theoretically vibrational spectrum of a structure are introduced featuring a single degree of freedom (SDOF) system as simplest approximation. The fundamental parameters, such as the damping ratio ζ , quality factor Q and the different regimes of damping are introduced from a mechanical perspective, followed by the description of the electro-mechanical analogy. Finally, the different damping mechanisms and dynamic modes are introduced, with respect to cantilever-like resonators.

2.1 Single degree of freedom (SDOF) system

A damped single degree of freedom (SDOF) system can be illustrated by a mass m , a spring with a spring constant k and a damper with a damping constant c . Such a system is schematically depicted in Figure 2.1, where m and k represents the kinetic and potential energy stored in the system and the damper c can be interpreted as mechanical load. When such a system is placed into motion, the mass is experiences a certain displacement $x(t)$. According Hook's law, $x(t)$, being a function of time t is proportional to a force F_k and can be described as

$$F_k = kx(t). \quad (2.1)$$

According to Newton's second law F_k causes an acceleration in the opposite direction of the displacement and is expressed as

$$F_m = m\ddot{x}(t). \quad (2.2)$$

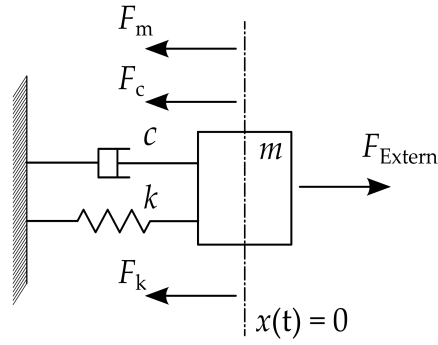


Figure 2.1: Single degree of freedom system.

If a viscous damping force acts on the mass, it can be expressed as

$$F_c = c\dot{x}(t). \quad (2.3)$$

From this assumptions and the free-body diagram in Figure 2.1, the equation of motion is seen to be

$$F_m + F_c + F_k = F_{\text{extern}} \quad (2.4)$$

where F_{extern} represents all external forces. After inserting Equations 2.1, 2.2 and 2.3 into Equation 2.4,

$$m\ddot{x}(t) + c\dot{x}(t) + kx(t) = F_{\text{extern}} \quad (2.5)$$

or

$$\ddot{x}(t) + \underbrace{\frac{c}{m}}_{a_1} \dot{x}(t) + \underbrace{\frac{k}{m}}_{a_2} x(t) = \frac{F_{\text{extern}}}{m}, \quad (2.6)$$

result with two constants a_1 and a_2 . For the case of a free vibration, meaning in the absence of any external forces ($F_{\text{extern}} = 0$), the system vibrates according to

$$\ddot{x}(t) + \underbrace{\frac{c}{m}}_{a_1} \dot{x}(t) + \underbrace{\frac{k}{m}}_{a_2} x(t) = 0. \quad (2.7)$$

This homogenous differential equation of the second order can be solved assuming a solution of the form

$$x(t) = Ce^{\lambda t}, \quad (2.8)$$

where λ and C are constants. Upon first and second differentiation of Equation 2.8

$$\dot{x}(t) = \lambda C e^{\lambda t} \quad (2.9)$$

$$\ddot{x}(t) = \lambda^2 C e^{\lambda t} \quad (2.10)$$

and substitution into Equation 2.7,

$$C e^{\lambda t} (\lambda^2 + a_1 \lambda + a_2) = 0 \quad (2.11)$$

is obtained, which is satisfied for all values of t if

$$\lambda^2 + a_1 \lambda + a_2 = 0 \quad (2.12)$$

and is known as the characteristic equation. Solving the quadratic function from Equation 2.12 using

$$\lambda_{1,2} = -\frac{a_1}{2} \pm \sqrt{\frac{a_1^2}{4} - a_2} = -\frac{c}{2m} \pm \sqrt{\left(\frac{c}{2m}\right)^2 - \frac{k}{m}}. \quad (2.13)$$

Equation 2.10 can then be rewritten as

$$x(t) = A_1 e^{\lambda_1 t} + B_1 e^{\lambda_2 t} \quad (2.14)$$

and

$$x(t) = e^{-(c/2m)t} \left(A_1 e^{\left(\sqrt{(c/2m)^2 - k/m}\right)t} + B_1 e^{-\left(\sqrt{(c/2m)^2 - k/m}\right)t} \right), \quad (2.15)$$

respectively. The first term $e^{-(c/2m)t}$ is an exponentially decaying function of time. The influence of the terms in the parentheses, however, depends on whether the numerical value within the radical is positive, negative or zero.

1. $(c/2m)^2 > k/m$: When the damping term $(c/2m)^2$ is larger than k/m , the exponents are real numbers and no oscillations are possible. Such a system is called denoted as over-damped.
2. $(c/2m)^2 < k/m$: In this case the exponents become imaginary numbers. Due to the Euler's formula $e^{i\varphi} = \cos(\varphi) + i \sin(\varphi)$, the terms of Equation 2.15 within the parentheses are oscillatory. Such a system is called under-damped.

3. $(c/2m)^2 = k/m$: In this case the damping term $(c/2m)^2$ is equal to k/m and indicates the transition between the oscillatory and non-oscillatory regime. Such a system is known as critical-damped, with

$$c_c = 2m\sqrt{\frac{k}{m}} = 2m\omega_0, \quad (2.16)$$

where ω_0 is known as eigenfrequency [13]. Any damping c can then be expressed by the so called damping ratio

$$\zeta \equiv \frac{c}{c_c} = \frac{c}{2m\omega_0} \quad (2.17)$$

and Equation 2.13 then becomes

$$\lambda_{1,2} = \left(-\zeta \pm \sqrt{\zeta^2 - 1}\right) \omega_0. \quad (2.18)$$

The three cases of damping discussed in this part can now be described by the damping ratio ζ and the natural angular frequency ω_0 . In the case of an oscillatory motion ($\zeta < 1$) and substituting Equation 2.17 into Equation 2.14, the general solution becomes

$$x(t) = e^{-\zeta\omega_0 t} \left(A_1 e^{i\sqrt{1-\zeta^2}\omega_0 t} + B_1 e^{-i\sqrt{1-\zeta^2}\omega_0 t} \right). \quad (2.19)$$

This equation can be also written as

$$x(t) = e^{-\zeta\omega_0 t} \left(C_1 \sin \sqrt{1-\zeta^2}\omega_0 t + C_2 \cos \sqrt{1-\zeta^2}\omega_0 t \right), \quad (2.20)$$

or

$$x(t) = X e^{-\zeta\omega_0 t} \sin \left(\sqrt{1-\zeta^2}\omega_0 t + \varphi \right) \quad (2.21)$$

and is known as the free-vibration response of an underdamped SDOF system, where φ is the phase, C_1 and C_2 are constants and can be calculated using the initial values of $\dot{x}(t)$ and $\ddot{x}(t)$ with $t = 0$. The argument $\sqrt{1-\zeta^2}\omega_0$ is per definition the damped natural angular frequency of the system. A graphical illustration of Equation 2.21 is given in normalized form in Figure 2.2

$$\omega_d \equiv \omega_0 \sqrt{1-\zeta^2} \quad (2.22)$$

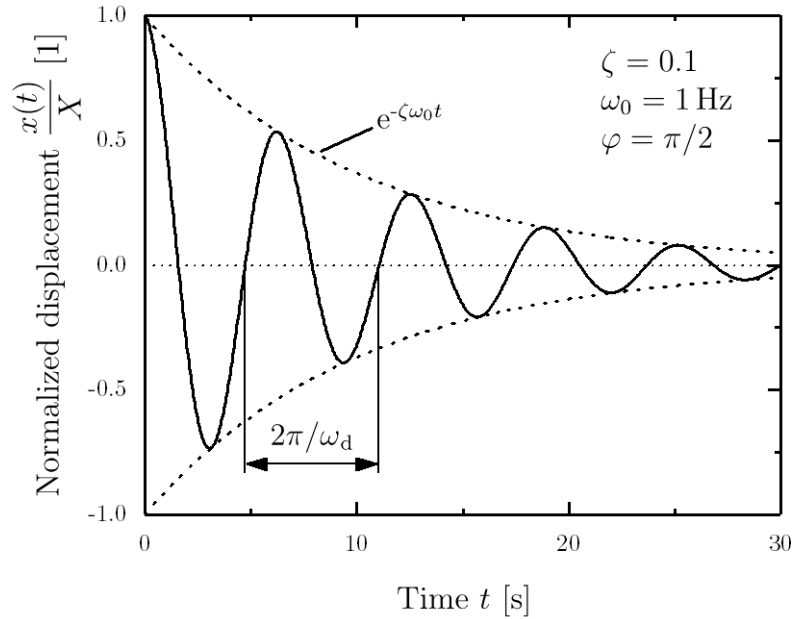


Figure 2.2: Normalized free vibration displacement response of a damped single degree of freedom system with a damping ratio $\zeta = 0.1$.

An alternative way how the energy dissipation inherent in a SDOF system can be described is by the so called quality factor Q as

$$Q \equiv \frac{1}{2\zeta} = \frac{1}{c} \sqrt{\frac{m}{k}}, \quad (2.23)$$

which provides a valid description of slightly damped systems. For highly damped vibrations, such it is the case of resonators in liquid environments an alternative description by Sader [40] is provided and is presented in Chapter 4. The solution for $x(t)$ in the case of non-oscillatory and critical damped conditions are not given in this thesis but can be looked up in Ref. [41].

Harmonically excited vibration

The equation of motion Equation 2.4 is now considered for the case in which an applied harmonic actuation force of the amplitude F_0 and corresponding frequency ω drives oscillations of the system. Therefore Equation 2.4 is rewritten as

$$m\ddot{x}(t) + c\dot{x}(t) + kx(t) = F_0 \sin \omega t. \quad (2.24)$$

The particular solution to the Equation 2.24 is a steady-state oscillation of the same angular frequency ω as that of the excitation and is of the form

$$x(t) = X \sin(\omega t - \varphi). \quad (2.25)$$

Thereby, X is the amplitude of oscillation and φ is the phase with respect to the excitation $F_0 \sin \omega t$. By substituting Equation 2.25 into Equation 2.24 X and φ are obtained and may be expressed as

$$X = \frac{F_0}{\sqrt{(k - m\omega^2)^2 + (c\omega)^2}} \quad (2.26)$$

and

$$\varphi = \tan^{-1} \frac{c\omega}{k - m\omega^2}. \quad (2.27)$$

Equations 2.26 and 2.27 can also be expressed as

$$X = \frac{\frac{F_0}{k}}{\sqrt{\left(1 - \frac{m\omega^2}{k}\right)^2 + \left(\frac{c\omega}{k}\right)^2}} \quad (2.28)$$

and

$$\varphi = \tan^{-1} \frac{\frac{c\omega}{k}}{1 - \frac{m\omega^2}{k}}. \quad (2.29)$$

In literature, Equations 2.28 and 2.29 are often expressed in non-dimensional form as

$$\frac{Xk}{F_0} = \frac{1}{\sqrt{\left[1 - \left(\frac{\omega}{\omega_0}\right)^2\right]^2 + \left[2\zeta \left(\frac{\omega}{\omega_0}\right)\right]^2}} \quad (2.30)$$

and

$$\varphi = \tan^{-1} \frac{2\zeta \left(\frac{\omega}{\omega_0}\right)}{1 - \left(\frac{\omega}{\omega_0}\right)^2} \quad (2.31)$$

using ω_0 , c_c and ζ from Equations 2.16 and 2.17, respectively. A graphically illustration of Equation 2.30 is given for different damping ratio ζ in Figure 2.3.

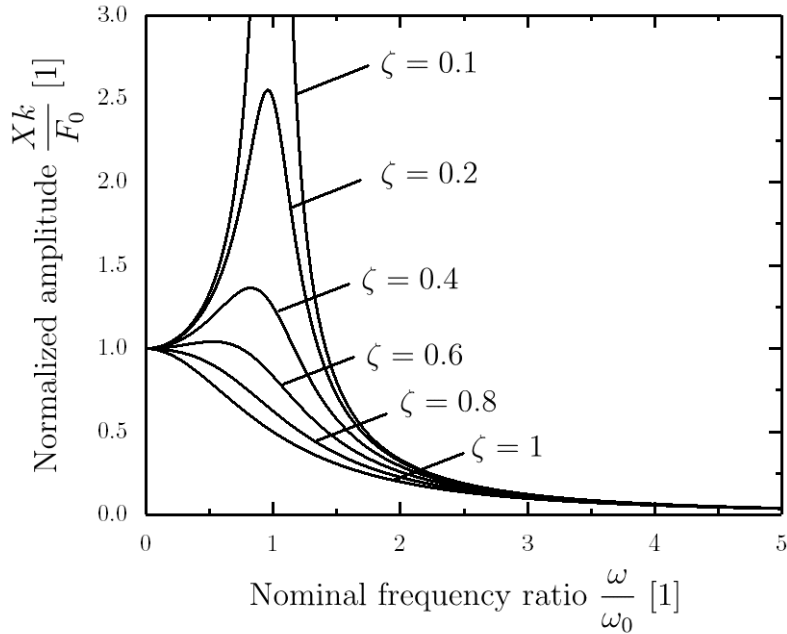


Figure 2.3: Normalized displacement response of a harmonically excited vibration with various damping ratios ζ .

2.2 Electro-mechanical analogy

For the description of oscillating electrical systems such as LC circuits, a different formulation is used, which is introduced in this section. Since the physical background behind the formulations for mechanical and electrical oscillating systems is the same, an electro-mechanical analogy can be derived, under the prerequisite, that the wavelength of the oscillation is much higher than the dimensions of the vibrating system and the validity of the Ohm's law. This analogy is of particular interest for MEMS, where mechanical and electrical components interact in one integrated system. In this manner, the mechanical parameters c , m and k can also be described by electrical components as depicted in Figure 2.4, representing the electrical load by an ohmic resistor R_m , the stored magnetic energy by an inductor L_m and the stored electrical energy by a capacitor C_m , respectively. Such an electrical description is depicted in Figure 2.4, featuring a serial connection of R_m , L_m and C_m and is referred to be the electro-mechanical analogy of the first order. With respect to the mechanical description in Figure 2.1 the electro-mechanical coupling is deduced and the coupled parameters are listed in Table 2.1. Using this analogy the natural

angular frequency ω_0 and the quality factor Q from Equations 2.16 and 2.23 can also be expressed as

$$\omega_0 = \frac{1}{\sqrt{L_m C_m}}, \quad (2.32)$$

and

$$Q = \frac{1}{R_m} \sqrt{\frac{L_m}{C_m}}, \quad (2.33)$$

respectively. This analogy can be used beneficially to characterize the frequency response of piezoelectric actuated and resonantly operating transducers and is described in Chapter 6.

Table 2.1: Electrical and mechanical parameters of the electro-mechanical analogy of the first order.

Mechanical		\leftrightarrow	Electrical	
Force	F	\leftrightarrow	Voltage	V_{exc}
Velocity	$\dot{x}(t)$	\leftrightarrow	Current	I_m
Damping	c	\leftrightarrow	Ohmic resistance	R_m
Mass	m	\leftrightarrow	Inductance	L_m
Spring	k	\leftrightarrow	Capacitance	C_m

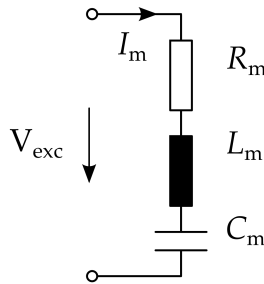


Figure 2.4: Electro-mechanical analogy of the first order.

2.3 Damping mechanisms

In the previous section the quality factor has been introduced as a coefficient between the stored and the dissipated energy per oscillation cycle of an e.g. flexural mode resonator. The dissipated energy can be caused by different

physical damping mechanisms, which will be introduced in this section. The resulting Q -factor of such a system is then obtained by the sum of the inverse quality factors as [13]

$$\frac{1}{Q} = \frac{1}{Q_{\text{intrinsic}}} + \frac{1}{Q_{\text{clamping}}} + \frac{1}{Q_{\text{medium}}} + \frac{1}{Q_{\text{other}}}, \quad (2.34)$$

where $Q_{\text{intrinsic}}$ stands for all losses within the resonator. These include friction and fundamental losses. The first category is based on the friction resulting from material imperfections located on the surface and in the bulk of the resonator. The fundamental losses are based on interactions between the strain field inside the resonator during vibration with phonons and electrons only when assuming an ideal material. The second loss mechanism is named clamping losses Q_{clamping} , which accounts for radiation of vibrational energy through the anchor of a resonator. The losses due to a surrounding medium Q_{medium} can cause substantial energy losses in a resonator and its energy dissipation can be roughly divided into three different regimes. Namely, the surrounding media can either be a viscous liquid, a viscous fluidic or a rarefied ballistic gas. Finally, Q_{other} includes all energy losses, which are not covered by the first three such as *electrical charge damping* [42] or *magnetomotive damping* [43].

2.4 Free vibrational bending of beams

The mathematical description of the mode shape of vibrating beams is based on the beam theory finalized by Leonard Euler¹ and Daniel Bernoulli² in the eighteenth century. Their theory, named *Euler–Bernoulli beam theory* allows for the exact description of eigenmode problems of slender beams, where the length of the beam greatly exceeds its thickness and under the assumption that rotational inertia and shear deformation can be neglected. The equation of motion can then be derived by means of the equilibrium of forces for an infinitesimal small piece of the beam. Assuming small deflections $z(x, t)$, in combination with a linear elastic material, the equation of motion is given by [44]

$$\rho_b A \frac{\partial^2 z(x, t)}{\partial t^2} + \mathcal{E} \mathcal{I} \frac{\partial^4 z(x, t)}{\partial x^4} = 0, \quad (2.35)$$

¹Leonard Euler (15 April 1707 – 18 September 1783): Swiss mathematician, physicist, astronomer, logician and engineer

²Daniel Bernoulli (8 February 1700 – 17 March 1782): Swiss mathematician and physicist

where ϱ_b is the areal mass density, A donates the cross section area, \mathcal{E} is the Young's modulus and \mathcal{I} represents the moment of inertia of the beam. The solution of Equation 2.35 can be obtained by separation of variables

$$z(x, t) = \sum_{n=1}^{\infty} Z_n(x) \cos(\omega t), \quad (2.36)$$

where n stands for the modal number and ω is the angular frequency of motion. The general solution of $Z_n(x)$ can be described as

$$Z_n(x) = C_1 \cos(\beta_n x) + C_2 \sin(\beta_n x) + C_3 \cosh(\beta_n x) + C_4 \sinh(\beta_n x) \quad (2.37)$$

with

$$\beta_n = \frac{\varrho_b A \omega_n^2}{\mathcal{E} \mathcal{I}}, \quad (2.38)$$

where C_1 - C_4 are constants, β_n is known as wavenumber and ω_n is called natural angular frequency for a specific modal number n . By using Equation 2.37, the displacement of the beam can be calculated for arbitrary modal number n , under the consideration of boundary conditions, which are listed in Table 2.2 for a clamped-free, clamped-clamped and free-free supported beam. For single side clamped beams, non-trivial solutions of Equation 2.37 exist if

$$\cosh(\beta_n L_b) \cos(\beta_n L_b) + 1 = 0. \quad (2.39)$$

For a clamped-clamped or free-free configuration, non-trivial solutions exist if

$$\cosh(\beta_n L_b) \cos(\beta_n L_b) - 1 = 0. \quad (2.40)$$

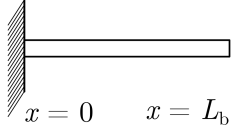
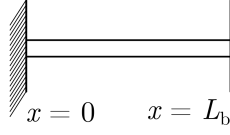
The values for the normalized wavenumber $\beta_n L_b$ can then be calculated numerically and are listed in Table 2.3. Considering the boundary values for a single side clamped beam from Table 2.2, it can be concluded that $C_1 + C_3 = 0$ and $C_2 + C_4 = 0$. Therefore, Equation 2.37 is reduced to

$$Z_n(x) = C_1(\cos(\beta_n x) - \cosh(\beta_n x)) + C_2((\sinh(\beta_n x) - \sin(\beta_n x))). \quad (2.41)$$

Considering $Z_n(x)'' = 0$, the ratio C_2 and C_1 can be expressed as

$$\frac{C_2}{C_1} = -\frac{\cosh(\beta_n x) + \cos(\beta_n x)}{\sinh(\beta_n x) + \sin(\beta_n x)}, \quad (2.42)$$

Table 2.2: Boundary values for the solution of the displacement function of beams with clamped-free, clamped-clamped and free-free support. The quotation marks ' , ' ' and ' ' ' represent the first, second and third deviation over x ($\frac{\partial}{\partial x}$, $\frac{\partial^2}{\partial x^2}$ and $\frac{\partial^3}{\partial x^3}$), respectively.

	clamped	free	clamped	clamped	free	free
						
	$x = 0$	$x = L_b$	$x = 0$	$x = L_b$	$x = 0$	$x = L_b$
$x = 0$	$Z_n(x) = 0$		$Z_n(x) = 0$		$Z_n(x)'' = 0$	
	$Z_n(x)' = 0$		$Z_n(x)' = 0$		$Z_n(x)''' = 0$	
$x = L_b$		$Z_n(x)'' = 0$		$Z_n(x) = 0$		$Z_n(x)'' = 0$
		$Z_n(x)''' = 0$		$Z_n(x)' = 0$		$Z_n(x)''' = 0$

and Equation 2.37 becomes

$$Z_n(x) = C_1 \left[\cosh(\beta_n x) - \cos(\beta_n x) + \frac{\cosh(\beta_n L_b) + \cos(\beta_n L_b)}{\sinh(\beta_n L_b) + \sin(\beta_n L_b)} \left(\sin(\beta_n x) - \sin(\beta_n x) \right) \right] \quad (2.43)$$

For a beams with clamped-clamped and free-free support the same procedure is applicable, which leads under the consideration of the corresponding boundary values from Table 2.2 to the displacement functions of the beam as

$$Z_n(x) = C_1 \left[\cos(\beta_n x) - \cosh(\beta_n x) - \frac{\cos(\beta_n L_b) - \cosh(\beta_n L_b)}{\sin(\beta_n L_b) - \sinh(\beta_n L_b)} \left(\sin(\beta_n x) - \sinh(\beta_n x) \right) \right], \quad (2.44)$$

and

$$Z_n(x) = C_1 \left[\cos(\beta_n x) + \cosh(\beta_n x) - \frac{\cosh(\beta_n L_b) - \cos(\beta_n L_b)}{\sinh(\beta_n L_b) - \sin(\beta_n L_b)} \left(\sin(\beta_n x) + \sinh(\beta_n x) \right) \right], \quad (2.45)$$

respectively. The solution of the displacement function Z_n is often written in normalized form as $\phi_n(x) = Z_n(x)/\max(Z_n(x))$ over a normalized beam length x/L_b . In Figure 2.5 the nominal mode shapes $\phi_n(x)$ for all three clamping conditions for $n = 1, 2, 3$ and 4 are depicted. The obtained information about the mode shape are used to determine the exact position of the nodal lines, which are considered in the design and fabrication process for the investigated resonators and are discussed in Chapters 7, 8, 9 and 10.

Table 2.3: Calculated normalized wavenumber $C_n = \beta_n L_b$ for clamped-free, clamped-clamped and free-free supported beams for arbitrary modal number n .

n	clamped-free	clamped-clamped	free-free
1	1.8751	4.7300	4.7300
2	4.6941	7.8532	7.8532
3	7.8548	10.9956	10.9956
$n > 3$	$\sim (2n - 1)\pi/2$	$\sim (2n + 1)\pi/2$	$\sim (2n + 1)\pi/2$

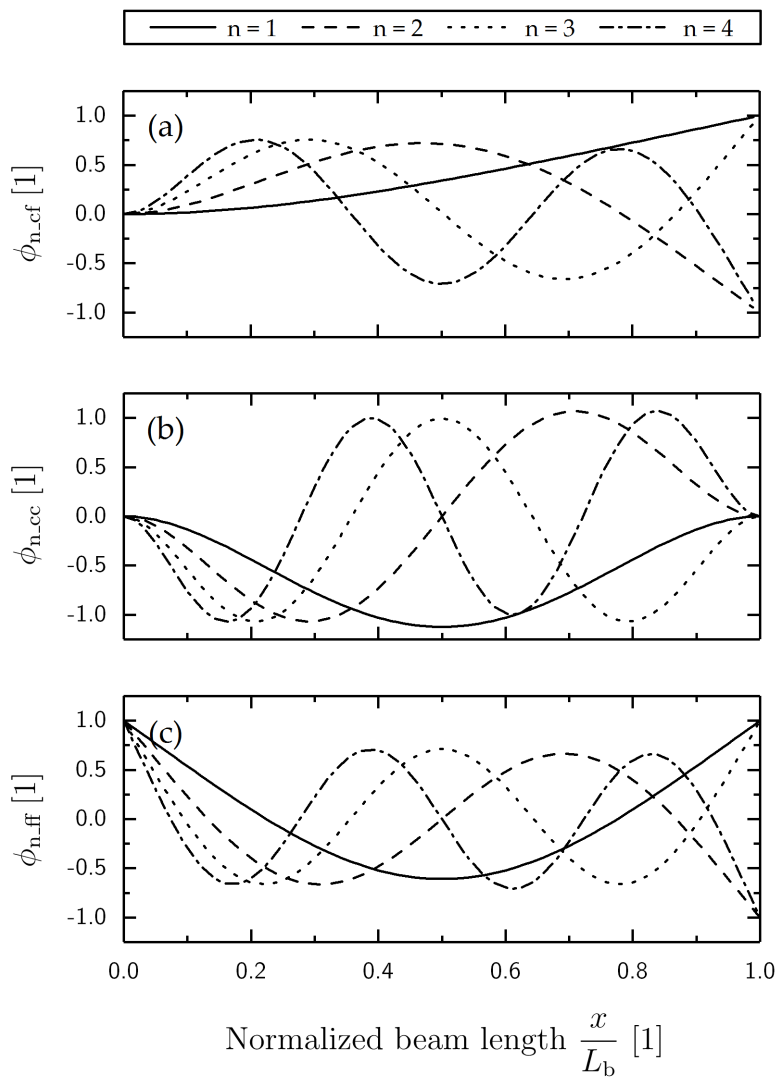


Figure 2.5: Schematic of the first four bending modes for beams with (a) clamped-free, (b) clamped-clamped and (c) free-free support.

Chapter 3

Piezoelectricity

Piezoelectricity is the property of certain crystalline materials that become electrically polarized when subjected to mechanical stress and conversely change shape when an applied electric field is applied. The word *piezoelectricity* is derived from the two greek words: *piezō*, which means to press or squeeze; and *ēlektron*, which means amber, an ancient source of electric charge. This material property can be technologically used in many applications, where a conversion of electrical signals into mechanical signals or *vice versa* is required. In the last two decades a significant technological progress in the manufacturing process of piezoelectric materials could be observed which opens new markets with turnovers of billions of dollars [45] such as information and communications [46], industrial automation [47, 48], or medical diagnostics [49]. In this chapter the fundamentals of piezoelectricity are introduced. In Section 3.1 the history from the discovery to the first applications of piezoelectricity is presented followed by a detailed description of the mechanism and requirements for piezoelectric materials. In the last section of this chapter, the most widespread piezoelectric materials in the field of MEMS are compared in terms of their piezoelectric constants, manufacturing aspects and specific application scenarios followed by a section focusing on aluminium nitride.

3.1 History

The discovery of piezoelectricity dates back to the 1880s, where the French physicists Jacques¹ and Pierre Curie² studied mechanical behavior of various hemihedral crystals. They went on to state, that

”those crystals having one or more axes whose ends are unlike, that is to say hemihedral crystals with oblique faces, have the special physical property of giving rise to two electrical poles of opposite signs at the extremities of these axes when they are subjected to a change in temperature: this is the phenomenon known under the name of pyroelectricity.” ... ”We have found a new method for the development of polar electricity in these same crystals, consisting in subjecting them to variations in pressure along their hemihedral axes.” [50].

In 1881, Gabriel Lippmann³ predicted the converse effect, which was experimentally verified by the Curie brothers within the same year [51]. The name piezoelectricity was finally proposed by Hankel [52] in 1882. The first practical application using the piezoelectric effect was developed 35 years later, during the First World War in 1917, where Constantin Chilowsky and Paul Langevin developed an ultrasonic, quartz crystal-based submarine detector [53]. In 1921 the first quartz crystal stabilized electrical oscillator was developed, leading to the first radio transmitter which was placed into service in 1924. These outstanding inventions are still part of our daily life as almost 90 years later, quartz crystal controlled oscillators are still the secondary standard for frequency and timing control. But not only for clocking, piezoelectricity finds nowadays a wide spread field of applications in micromachined sensors and actuators such as microphones [54], energy harvesters [55], nanomechanical movers [56], loudspeakers [57] and many more.

¹Paul-Jacques Curie (29 October 1856 – 19 February 1941): French physicist and professor of mineralogy at the University of Montpellier

²Pierre Curie (15 May 1859 – 19 April 1906): French physicist and husband of Marie Skłodowska-Curie.

³Gabriel Lippmann (16 August 1845 – 13 July 1921): Franco-Luxembourgish physicist

3.2 Fundamentals

The fundamental correlation between the mechanical and electrical properties of piezoelectric materials can be described by the so called Heckmann diagram [58], which is shown in its simplified representation for a constant temperature and entropy in Figure 3.1. The correlation mechanisms are illustrated by the combination of the electric displacement field

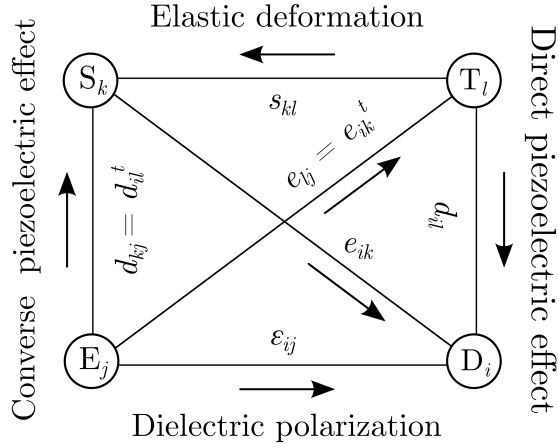


Figure 3.1: Simplified Heckmann diagram for constant temperature and entropy illustrating the piezoelectric tensors e_{jk} and d_{ik} , the corresponding transposed counterparts e_{lj}^t and d_{kj}^t , the compliance tensor s_{kl} and the permittivity tensor ε_{ij} .

$$D = \varepsilon E \implies D_i = \varepsilon_{ij} E_j \quad (3.1)$$

and the Hooke's law for a linear elastic material

$$S = s T \implies S_k = s_{kl} T_l, \quad (3.2)$$

where D is the electric displacement field, ε is the permittivity, E is the electric field strength, S is the mechanical strain, s is the compliance and T represents the mechanical stress. In the case of an isotropic and linear material, these physical quantities can be written as scalars. For anisotropic linear materials, however, all quantities have to be treated as tensors first or higher orders, which is indicated by the indices i, j, k and l . To describe the interaction between these electrical and mechanical formulations, Equations 3.1 and 3.2 are combined to

the so called coupled equations resulting in

$$S = sT + d^t E \implies S_k = s_{kl}^E T_l + d_{kj} E_j \quad (3.3)$$

and

$$D = dT + \varepsilon E \implies D_i = d_{il} T_l + \varepsilon_{ij}^T E_j, \quad (3.4)$$

where the strain S depends on the electric field strength E by the piezoelectric tensor d , and the electric displacement field D depends on mechanical stress T , representing the direct and converse piezoelectric effect, respectively. The superscripts T and E indicate constant stress or electrical field conditions. With respect to piezoelectric devices, two significant parameters can be extracted from Equations 3.3 and 3.4. The first one is the value of d_{33} , where the mechanical strain is parallel to the applied electric field strength and is called longitudinal piezoelectric coefficient. The second one is the value of d_{31} , where the mechanical strain is perpendicular to the applied electric field strength and is called transversal piezoelectric coefficient. These two coefficients can be often found in literature, allowing the comparison between different piezoelectric materials.

3.3 Material aspects

As mentioned in the introduction of this chapter, only a certain amount of crystals show piezoelectric properties. The fundamental requirement for materials to be piezoelectrically active is the absence of inversion symmetry in the unit cell. That means, that for any point in the unit cell (x, y, z) a distinguishable point $(-x, -y, -z)$ is required [59], which is the case for 20 of the 32 crystal classes. As the absence of an inversion symmetry does not determine the magnitude of the piezoelectric coupling coefficients, it can be concluded that the absence of the inversion symmetry represents a necessary, but not a sufficient requirement for the material to exhibit any measurable piezoelectric effect. Additionally, a high permittivity in a strongly polar lattice in the broad vicinity of the phase boundaries of the considered material is required to ensure large piezoelectric constants and strong elasto-electric correlation [45]. In Table 3.1, the most widespread materials are listed and compared regarding their electrical and mechanical properties.

Table 3.1: Material related electrical and mechanical properties of sputter deposited lead zirconate titanate (PZT), aluminium nitride (AlN) and zinc oxide (ZnO) thin films [60–75].

Property	Unit	PZT	AlN	ZnO
Crystal structure	-	perovskite	wurtzite	wurtzite
Rel. permittivity	[1]	980	10	9-9.7
Curie temperature	[°C]	370	1150	-
Young's modulus	[GPa]	75	243.5	250 - 360
d_{33}	[pm/V]	85	2.75 - 5.15	11
d_{31}	[pm/V]	-85 - -102	-0.75 - -2	-5.3

Aluminium nitride

Aluminium nitride (AlN) is a piezoelectric material, which has been studied over the last decades. It is a transparent solid and, due to its beneficial material properties, it is widely used as thin-film material for various applications. The most significant property of AlN with respect to a potential commercialization is probably its CMOS compatibility, which allows the integration of AlN in commonly used silicon based processes in microelectronics and MEMS [76, 77]. Its high thermal conductivity of about 3.0 W/cm·K [78] can beneficially be used for heat dissipation in high power applications [79] and due to its high thermal and chemical resistivity AlN is also often used as passivation layer [80].

Its piezoelectric properties are relatively low, compared to other piezoelectric materials such as PZT [76, 81] or ZnO [82–84]. Therefore, AlN is typically used for dynamic applications in the field of MEMS such as energy harvesters [55], microphones [54] or loudspeakers [57]. The high speed of sound in AlN of about 11400 m/s [85], in combination with its piezoelectric properties make it the preferable material for surface acoustic wave (SAW) [77] and bulk acoustic wave (BAW) devices [86]. In addition, its Curie temperature ϑ_c , which is the temperature at which the material loses its piezoelectric properties, is at 1150°C about three to four times higher compared to PZT, ensuring proper operation even at higher temperatures [76, 87].

Deposition

AlN thin films can be deposited using different techniques such as plasma enhanced chemical vapor deposition (PECVD) [88], pulsed laser deposition,

molecular beam epitaxy (MBE), atomic layer deposition (ALD) [89] as well as AC and DC magnetron sputter deposition [90]. The latter is probably the most commonly used technique for MEMS, due to its comparable low deposition temperatures in combination with high deposition rates. Additionally, by careful selection of the deposition parameters a formation of a polar axis is possible, making the typically necessary annealing step for the activation of piezoelectric materials obsolete.

Chapter 4

Fluid-Structure interaction

4.1 Reynolds number

The Reynolds number Re named after Osborne Reynolds¹ is a dimensionless quantity in the field of fluid mechanics and is used to predict the type of flow under different flow conditions. It is defined as the ratio of inertial forces to viscous forces within a fluid which is subjected to relative internal movement due to different fluid velocities

$$Re = \frac{F_{\text{inertial}}}{F_{\text{viscous}}}. \quad (4.1)$$

Thereby, the inertial forces can be considered as a factor in developing turbulent flow. The viscosity of the fluid and the corresponding fluid friction counteracts this effect as more kinetic energy is absorbed by a more viscous fluid, which is modeled by viscous forces in Equation 4.1. Consequently, the Reynolds number quantifies the relative importance of these two forces and gives an indication whether laminar or turbulent flow is present in a particular situation. In Figure 4.1 the Reynolds numbers of conventional objects and creatures at a given velocity are depicted, illustrating the change of the Reynolds number with increasing velocity and geometry. A very powerful aspect of the Reynolds number is, that objects with similar geometry and Reynolds number show similar flow behavior, which allows for modeling and testing of scaled prototypes for large objects such as aircraft or ships in wind or water channels, respectively. In

¹Osborne Reynolds (23 August 1842 – 21 February 1912): British physicist at the University of Manchester

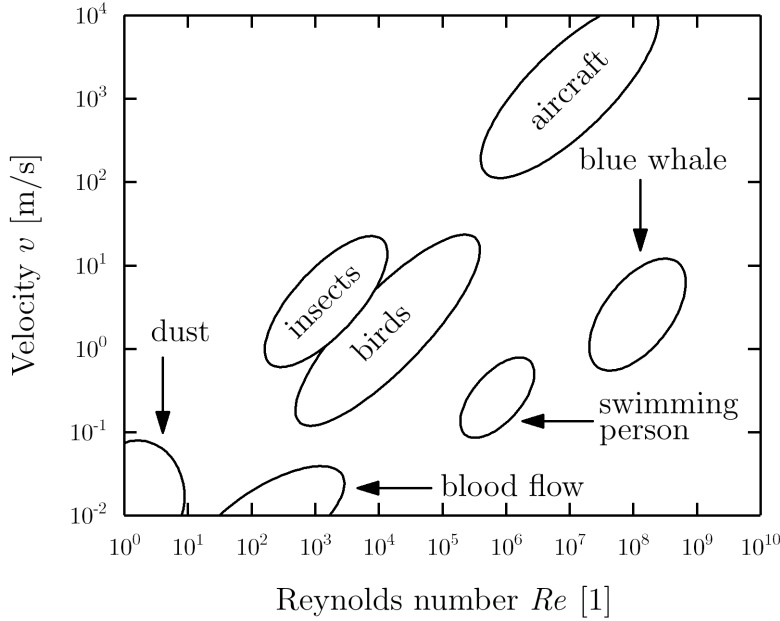


Figure 4.1: Comparison of the velocity v and Reynolds number Re for different objects in air and water [91].

literature, the Reynolds number is often written as

$$Re = \frac{\varrho v \mathcal{L}}{\mu} = \frac{v \mathcal{L}}{\nu}, \quad (4.2)$$

where ϱ , v , ν , and μ denote the density, the velocity, the kinematic and the dynamic viscosity of the fluid, respectively. The parameter \mathcal{L} represents a characteristic length related to the object. The latter is a matter of convention and differs for each particular situation. For example, the inner pipe diameter is used as characteristic length to describe the flow in a pipe [92]. For aircraft or ships, its length or width are often considered. For elastic beams, as considered in this thesis, the characteristic length of the flow is the minimum of (a) the beam width W and (b) the length scale of spatial oscillations $1/\beta_n$ [93], where β_n is the wavenumber as described in Chapter 2. For microscopic resonators, such as MEMS cantilevers with high aspect ratios operating at low modal number, the characteristic length is usually the width of the beam W [40] and Re can then be expressed as

$$Re = \frac{\varrho \omega_{\text{fluid}} W^2}{4\mu}, \quad (4.3)$$

where ω_{fluid} is the angular frequency in the fluid. From Equation 4.1 it can be concluded that in the case of large Reynolds numbers, viscous effects can be neglected and the fluid can be modeled as inviscid in nature, which is mainly applicable for macroscopic structures [94]. For such systems, Chu [95] formulated the well-known approximation of the resonance frequency ω_{fluid} in inviscid fluids as

$$\frac{\omega_{\text{fluid}}}{\omega_{\text{vac}}} = \left(1 + \frac{\pi \rho W}{4 \rho_b T}\right)^{-1/2}, \quad (4.4)$$

where ω_{vac} is the angular frequency in vacuum. However, if Equation 4.3 and Equation 2.38 from Chapter 2 are considered, it becomes evident that a decrease in the physical dimensions of the structure will result in a reduction of the Reynolds number and viscous effects become more and more important. Based on these approximations, Sader introduces a complex hydrodynamic function Γ for rigid beams allowing the estimation of the angular frequency in the fluid ω_{fluid} and the quality factor for low modal number n in non-compressive viscous fluids [40]. Equation 4.4 then becomes

$$\frac{\omega_{\text{fluid},n}}{\omega_{\text{vac},n}} = \left(1 + \frac{\pi \rho W^2}{4 \rho_b A} \Gamma_r(\omega_{\text{fluid},n})\right)^{-1/2} \quad (4.5)$$

and the mode-dependent quality factors can be expressed as

$$Q_n = \frac{\frac{4\mu}{\pi \rho W^2} + \Gamma_r(\omega_{\text{fluid},n})}{\Gamma_i(\omega_{\text{fluid},n})}, \quad (4.6)$$

where the index $_r$ and $_i$ indicate the real and imaginary part of the hydrodynamic function, respectively. This approach for non-compressive viscous fluids is expected to be valid for the fundamental mode and the first few harmonics, where the acoustic wavelength λ_{sound} greatly exceeds the characteristic length of the flow \mathcal{L} [96] and has been experimentally validated for numerous theoretical models based on incompressible flow in Refs. [97–99]. For the operation at higher modal number n , however, the assumptions regarding the characteristic length have to be reassessed as with increasing modal number also the length scale of spatial oscillations $1/\beta_n$ decreases and the spatial wavelength of the beam will eventually set the characteristic length of the object. These considerations have been studied by Van Eysden *et al.* [93], who investigated the change in the acoustic wavelength and spatial wavelength of the beam for higher modal

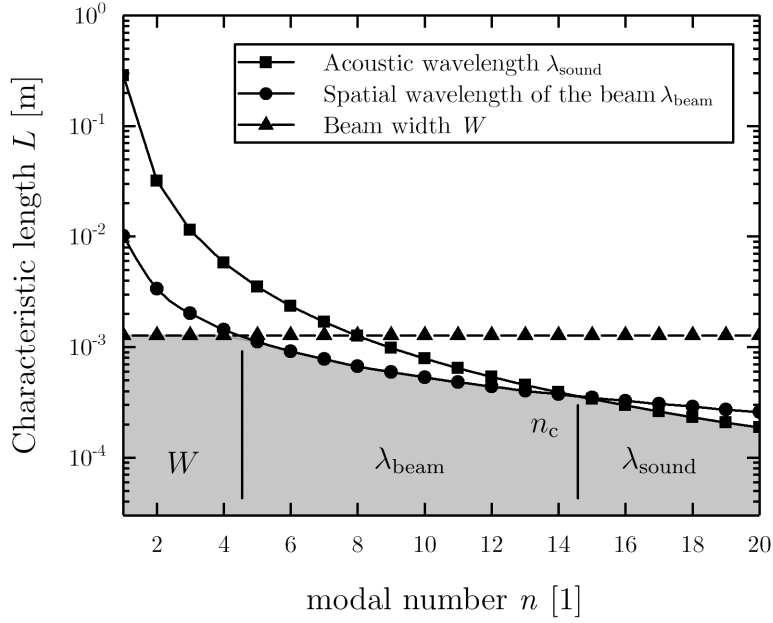


Figure 4.2: Experimentally estimation of the dominant characteristic length \mathcal{L} for a cantilever beam with a length L_b of $2500 \mu\text{m}$, a width W_b of $1200 \mu\text{m}$, a fundamental resonance frequency in vacuum of $\sim 5 \text{ kHz}$ and a speed of sound v_c of $\sim 1000 \text{ m/s}$.

number n , where he estimated the acoustic wavelength as

$$\lambda_{\text{sound}} = \left(\frac{\beta_1}{\beta_n} \right)^2 \frac{v_c}{f_{\text{vac},1}} \approx \frac{1.425}{(2n-1)^2} \frac{v_c}{f_{\text{vac},1}}. \quad (4.7)$$

and the spatial wavelength of the beam as

$$\lambda_{\text{beam}} = \frac{2\pi\mathcal{L}}{\beta_n} \approx \frac{4\mathcal{L}}{2n-1}, \quad (4.8)$$

where $f_{\text{vac},1}$ is the resonance frequency for the fundamental mode ($n = 1$). From Equations 4.7 and 4.8 it can be seen, that λ_{beam} obtains a weaker dependency on n than the acoustic wavelength. Therefore, λ_{sound} and λ_{beam} become comparable at higher values of n and compressibility is no longer negligible, as it can be seen in Figure 4.2. At the so-called coincidence point, where λ_{sound} is equal to λ_{beam} , a critical modal number n_{crit} can be derivative from Equations 4.7 and 4.8 and can be expressed as

$$n_{\text{crit}} \sim \frac{0.178v_c}{f_{\text{vac},1}L_b}. \quad (4.9)$$

In Figure 4.2 an exemplary estimation of the critical modal number for a cantilever beam with a length L_b of 2500 μm , a width W_b of 1200 μm , a resonance frequency of the fundamental mode in vacuum of 5 kHz, vibrating in a liquid such as acetone with a speed of sound v_c of ~ 1000 m/s is given. It can be seen, that the dominant characteristic length for the fundamental and the first few harmonics is the width of beam W , which, at $n \sim 4$, becomes the spatial wavelength of the beam λ_{beam} as already mentioned above. Furthermore, due to the different dependencies on the modal number of spatial and acoustic wavelengths of the beam, the latter becomes the dominant characteristic length at $n = n_{\text{crit}} \sim 14$.

4.2 Temperature dependence of fluid properties

The specific parameters of fluids such as the density ρ_{fluid} , the kinematic viscosity ν_{fluid} or the dynamic viscosity μ_{fluid} show different temperature dependencies. But in most cases values of ρ_{fluid} , ν_{fluid} and μ_{fluid} are only known at certain key temperatures. To obtain the actual value at a specific temperature apart from the key temperature, at least empirical estimations are required. In the following two sections such approximations of the fluid properties at different temperatures are reported. Thereby, ν_{fluid} , μ_{fluid} and ρ_{fluid} are estimated in a temperature range from 0°C up to 100°C. This is done using a double logarithmic approach for ν_{fluid} , μ_{fluid} and a linear function for ρ_{fluid} .

Ubbelohde-Walther equation

The non-linearity between the viscosity and the temperature of fluids can be described using a double logarithmic function with the empiric relation [100]

$$\lg(\lg(\nu_{\text{fluid}} + 0.8)) = K_f - m_f \lg(\vartheta), \quad (4.10)$$

where ν_{fluid} is the kinematic viscosity of the fluid, K_f and m_f are fluid dependent constants and ϑ is the temperature of the fluid. This relation is known as the *Ubbelohde-Walther equation*, named after the German chemist Leo Ubbelohde (1877-1964). To calculate the unknown parameters K_f and m_f of a certain fluid, viscosity values at two different temperatures are required. As a next step, ν_{fluid}

can be calculated at any temperature using

$$\nu_{\text{fluid}} = 10^{10^{K_f - m_f \lg(\vartheta)}} - 0.8. \quad (4.11)$$

This evaluation of the kinematic viscosity of the fluid is also valid for the dynamic viscosity of the fluid μ_{fluid} . From Equation 4.11 it can be concluded, that both the kinematic and the dynamic viscosity of fluids show a strong dependency on temperature.

Density approximation

The increase in temperature of a fluid leads to thermal expansion and causes a decrease in the density ρ_{fluid} . This relation can be described using a linear function such as

$$\rho_{\text{fluid}} = k_f \vartheta + d_f. \quad (4.12)$$

The unknown parameters k_f and d_f , can again be calculated using two density values at two different temperatures. Finally, the value at a specific temperature can be calculated using Equation 4.12. Using these formulations, the kinematic and dynamic viscosities as well as the densities are calculated in a temperature range from 0 up to 100°C and the corresponding values are listed in the Appendix A.1.

Chapter 5

Fabrication

Parts of this chapter have already been published in Refs. [36, 101]

One main part of this thesis was the manufacturing of piezoelectrically excited MEMS resonators, which are based on the process introduced by M. Kucera and E. Wistrela in Refs. [36]. The applied techniques are based on the well-established micro fabrication technologies such as lithography using image-reversal resist [102], thermal evaporation [103], sputter deposition [83], lift-off processes [104], deep reactive-ion etching (DRIE) [83] and wafer dicing [83]. In this chapter a summary of this fabrication process is illustrated by a schematic process flow in Figure 5.1, followed by a description of the specific designs and materials deployed in this work.

Substrate

To start of the fabrication process a double side polished 100 mm (4 inch) SOI prime silicon wafer with a crystal orientation of $\langle 100 \rangle$ is used. The wafer consists of a 20 μm thin device layer, which serves as support layer for the piezoelectric stack including electrodes, thus being a key component of the resonator, a 500 nm thin buried silicon oxide (SiO_2) and a 350 μm thick handle wafer. For isolation purposes an 80 nm thin LPCVD silicon nitride (Si_3N_4) on top of a 250 nm thin LPCVD silicon oxide is deposited on both sides of the wafer. A cross-sectional views of the substrate is given in Figure 5.1 (a).

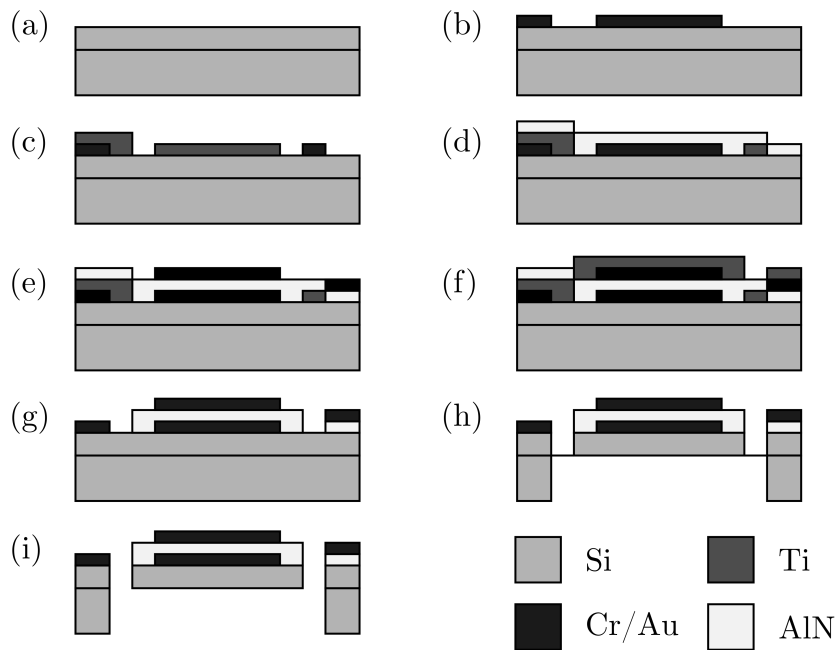


Figure 5.1: Schematic illustration of the process steps, including (a) the SOI substrate, (b) the deposition of the bottom electrode, (c and f) the deposition steps of the two titanium sacrificial layers, (d) the deposition of the piezoelectric AlN thin film, (e) the deposition of the top electrode, (g) the AlN lift-off process, and (h) the front and (i) the back side release.

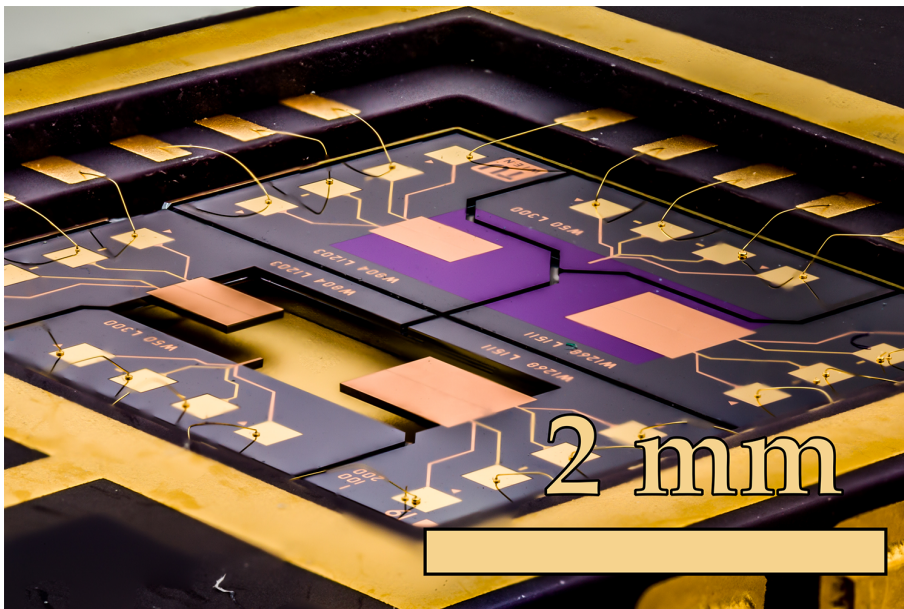


Figure 5.2: Optical micrograph of the finished fabricated bi-directional transducers featuring resonators with different dimensions and their non-released counterparts [105].

Bottom electrode

The deposition of the bottom electrode represents the initial step of the fabrication process. Thereby, the patterning of the bottom electrode is transferred to the substrate by image-reversal lithography. The used resist provides negative wall profiles, which are the preferable shape for the following deposition process of 50 nm chromium and 450 nm gold by thermal evaporation, where the chromium layer is used as adhesion promoter. Due to the negative wall profiles of the resist, the formation of a closed layer coverage is prevented. This is of utmost importance for the following lift-off process, where acetone is used to dissolve the resist and hence, to lift the abundant electrode material, resulting in a patterned bottom electrode as illustrated in Figure 5.1 (b).

Aluminium nitride and top electrode

The deposition and patterning process of the aluminium nitride layer are the most critical steps in the fabrication process and is realized in a *von Ardenne*[®] sputter equipment. For detailed description of the utilized sputter deposition process please refer to Ref. [106]. A well-documented problem is the formation of micro whiskers during wet chemical etching with the result of hardly removable aluminium nitride residuals after etching [107]. To avoid these unwanted residuals, an intermediate step is introduced, using two 300 nm thin sputter deposited titanium hard masks, where the hard masks are patterned in the same way as described in Section 5 and are shown in Figure 5.1 (c) and (f). On top of the patterned titanium hard mask, a 1 μm thin aluminium nitride layer is sputter deposited, followed by another evaporated, lift-off patterned 50 nm chromium and 450 nm gold thin film which serves as top electrode and is illustrated in Figure 5.1 (d) and (e), respectively. The second titanium hard mask is now deposited to protect the top electrode from the following etching steps as shown Figure 5.1 (f). As a next step the exposed aluminium nitride surface is wet chemical etched using phosphoric acid (H_3PO_4) and hydrofluoric acid (HF), where the aluminium nitride layer is not completely etched by the H_3PO_4 . Instead, the etching is stopped manually, when H_3PO_4 reaches the underlying titanium layer. The following etching step using HF lifts the top and underlying titanium layer completely including all aluminium nitride residuals, resulting in a nicely patterned stack of two electrodes sandwiching an

aluminium nitride layer, as shown in Figure 5.1 (g).

Front and back side release

Before the vibrating structure can be released from the supporting handle wafer, the two passivation layers on both sides consisting of 80 nm silicon nitride and 250 nm silicon oxide are dry etched using a patterned resist layer in combination with a parallel plate plasma etching equipment. Next, the exposed silicon surfaces of the device layer and the handle layer are dry etched using a deep reactive ion etching process. To stabilize the mechanical structure after the front side release, the entire surface of the wafer is passivated with three layers of AZ6624 resist. In both etching steps the process stops automatically at the buried SiO₂, as illustrated in Figure 5.1 (h). Finally, the remaining boxed oxide and the stabilizing resist are removed by wet chemical etching using HF and acetone, completing the resonator fabrication process as shown in Figure 5.1 (i).

For characterization purposes, a high precision wafer saw is used to dice the resonators in dies having a size of 0.6 x 0.6 mm². Afterwards, each die is cleaned using acetone and isopropanol and dried using compressed nitrogen. The diced resonators are clued into a 24-pin dual inline package (DIP) and wire bonded, subsequently. To overcome the obstacle of parasitic current caused by the conductivity of the surrounding liquids, the entire sensor element, including bond wires and ceramic package, is optionally passivated with an amorphous silicon dioxide (SiO₂) thin film with a thickness of $\sim 4 \mu\text{m}$.

A micrograph of a finished fabricated, packaged and wire bonded resonator is depicted in Figure 5.2.

Chapter 6

Actuation and sensing techniques

In this thesis, two different measurement techniques have been used to characterize the specific properties of resonating microstructures and are therefore discussed in the following chapter. In the first section, the so called self-actuation and self-sensing technique is described, where a piezoelectric layer is utilized to actuate and sense simultaneously the oscillation. This well-established technique allows fast electrical characterization and has been primarily used in this work. To gain information about the mode shape, a second technique using a laser Doppler vibrometer is utilized and is presented in the second section of this chapter. With these two characterization methods, a complete characterization of the investigated microstructures with respect to their oscillation behavior was obtained.

6.1 Piezoelectric actuation and sensing

In piezoelectrically actuated and resonantly operating systems the piezoelectric effect can be used for actuation and sensing at the same time, which is termed as *self-actuation and self-sensing* technique. For such a system, the converse piezoelectric effect can be utilized to transduce the applied electrical voltage to a mechanical strain and enables oscillation as already described in Chapter 3. At the same time the direct piezoelectric effect causes the generation of polarization charges, which are initiated by the strain in the piezoelectric material. Therefore, the increased values in the oscillation amplitude at resonance causes

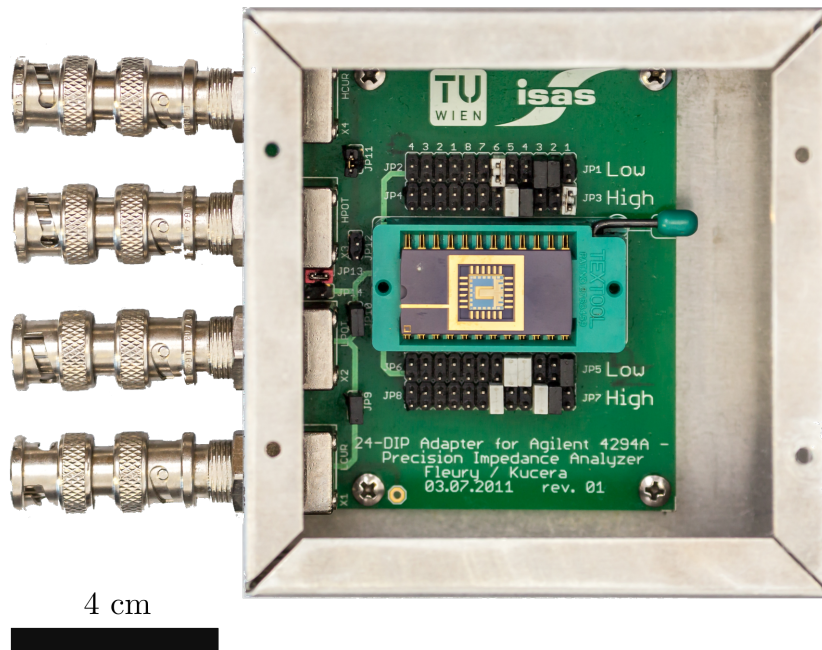


Figure 6.1: Picture of the utilized measurement box.

also increased values in the generated charges and can be measured electrically.

Impedance analysis

A convenient way to excite and sense the characteristic frequency response for the above introduced configuration is to measure the electrical impedance spectrum as a function of frequency. In this thesis an *Agilent*[®] (now *Keysight*[®]) 4294A precision impedance analyzer is used. It covers a broad frequency range from 40 Hz to 110 MHz with basic impedance accuracy of $\pm 0.08\%$. The test signal level ranges from $5 \text{ mV}_{\text{rms}}$ to 1 V_{rms} or from $200 \mu\text{A}_{\text{rms}}$ to $20 \text{ mA}_{\text{rms}}$ and the DC bias ranges from 0 V to $\pm 40 \text{ V}$ or from 0 mA to $\pm 100 \text{ mA}$. Additionally, advanced calibration and error compensation functions are implemented, enabling impedance matching of the measurement setup including cable or circuit board impedance. To reduce the setup complexity, a custom made evaluation box is used, providing a direct 4-wire connection to the impedance analyzer as shown in Figure 6.1 and Figure 6.2. The packaged transducer presented in Chapter 5 is inserted in the 24-DIP socket of the measurement box and is excited with a constant AC excitation voltage of $V_{\text{exc}} = 500 \text{ mV}_{\text{rms}}$. At the same time the current through the transducer I_{Sensing} is measured as it can be seen in

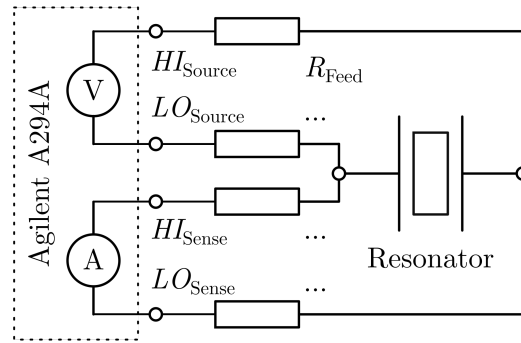


Figure 6.2: Illustration of the 4-wire measurement technique using an Agilent A294A impedance analyzer, including feed line resistances of the measurement equipment R_{feed} and the high and low potentials HI_{Source} , HI_{Sense} , LO_{Source} and LO_{Sense} .

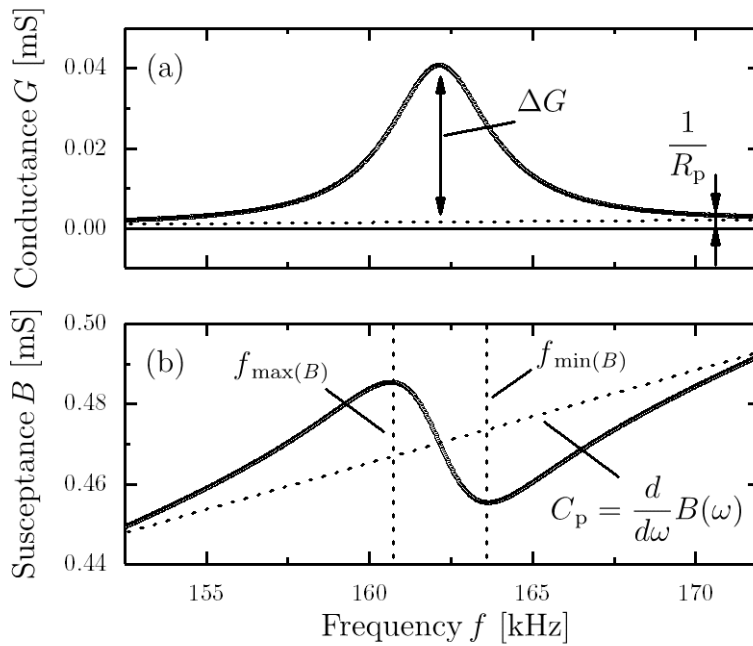


Figure 6.3: Illustration of a representative frequency response in terms of (a) the electrical conductance G and (b) the electrical susceptance B of a transducer, immersed in a viscosity standard with a density of 0.840 kg/l and a dynamic viscosity $\mu_{\text{fluid}} = 6.55 \text{ mPa}\cdot\text{s}$ at 20°C resulting in a resonance frequency of $f_{\text{res}} \sim 162 \text{ kHz}$.

Figure 6.2 and a resulting impedance Z and admittance Y are obtained using

$$Z = R + iX_e = \frac{V_{\text{exc}}}{I_{\text{Sensing}}} \quad \text{and} \quad Y = G + iB = \frac{I_{\text{Sensing}}}{V_{\text{exc}}} \quad (6.1)$$

respectively. A typical sample measurement of the admittance Y , represented by its real part G and the imaginary part B , is shown in Figure 6.3.

Advanced equivalent electrical circuit

For the frequency response of a bidirectional transducers as depicted in Figure 6.3, the electro-mechanical analogy of the first order presented in Chapter 2.2 does not provide a complete description of the system. The non-ideal material properties cause finite feed line resistivity and leakage currents through the piezoelectric layer, which result, in combination with the corresponding capacity, in a certain slope and offset in the conductance G and susceptance B . Therefore the equivalent electrical circuit from Figure 2.4 has to be adapted, which results in an advanced equivalent electrical circuit illustrated in Figure 6.4. Thereby, R_s is the feed line resistance and C_p and R_p model the capacity and the parallel resistance of the piezoelectric layer, respectively. This advanced equivalent electrical circuit, except R_s , is also known as the Butterworth van-Dyke equivalent circuit. For potential sensing applications, it has to be considered that R_s in combination with C_p act as a low-pass filter and causes a certain slope in the frequency response of the system. This property of the non-ideal system cannot be completely avoided but minimized by keeping R_s and C_p as low as possible. This is of major importance for transducers with a relatively large piezoelectric surface area and the resulting high value in C_p . If the low-pass behavior dominates over the resonator part in the frequency response, the extraction of the conductance peak from measured data becomes challenging, as shown for two frequency responses with identical values in ΔG but different values in R_s of 10Ω and 500Ω in Figure 6.5.

Data acquisition

Basically, three key parameters are in the focus of interest: these are the quality factor Q , the resonance frequency f_{res} and the height of the conductance peak ΔG . Based on the results shown in Figure 6.3, these three quantities can

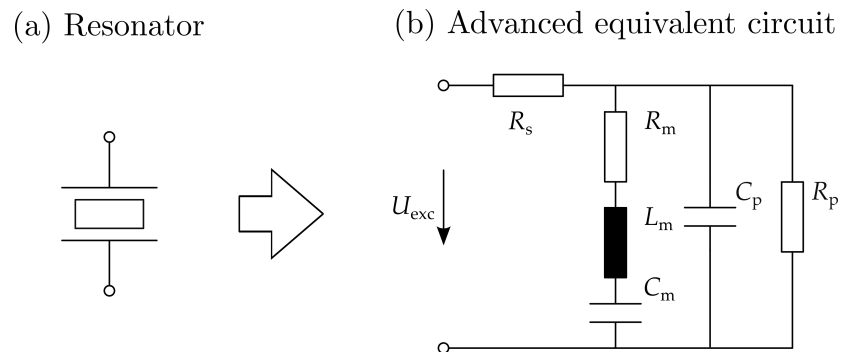


Figure 6.4: Equivalent electrical circuit of piezoelectric actuated resonator.

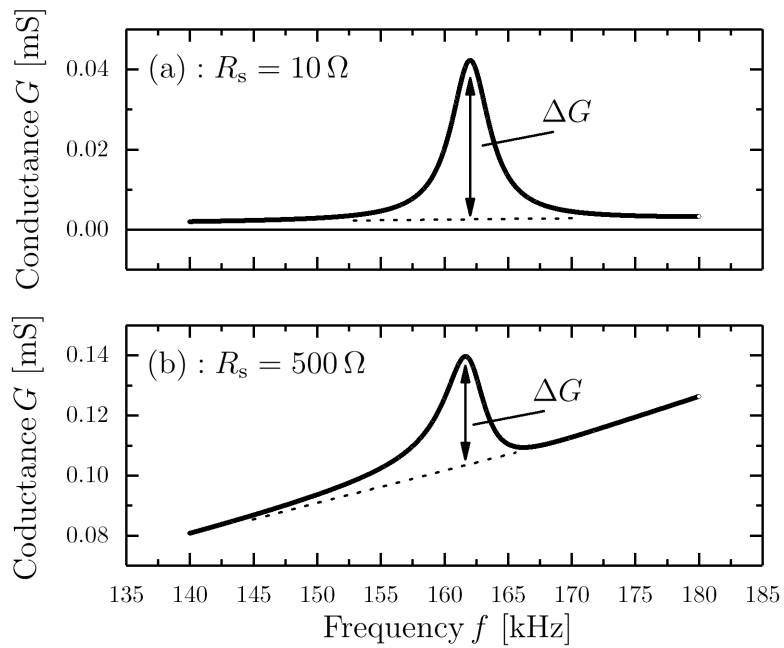
Figure 6.5: Comparison of the frequency responses for two different feed line resistances of $R_s = 10 \Omega$ in (a) and $R_s = 500 \Omega$ in (b).

Table 6.1: Typical values for the electrical components of the motional, parallel and serial part of the advanced equivalent electrical circuit.

Motional			Parallel		Serial
R_m	L_m	C_m	R_p	C_p	R_s
25.2 k Ω	1.09 H	885 fF	23.0 M Ω	462 pF	10 Ω

easily be extracted by applying a least squares fitting algorithm with *Levenberg-Marquardt* error minimization. From the fit, the resonance frequency f_{res} and the quality factor Q are calculated using the equations from Ref. [108]

$$f_{\text{res}} = \sqrt{\frac{f_{\min(B)}^2 + f_{\max(B)}^2}{2}} \quad (6.2)$$

and

$$Q = \frac{2f_{\text{res}}^2}{f_{\min(B)}^2 - f_{\max(B)}^2}, \quad (6.3)$$

where $f_{\max(B)}$ and $f_{\min(B)}$ represent the frequency at maximum and minimum susceptance B , as shown in Figure 6.3. The equivalent components R_m , L_m and C_m can be computed using Equations 6.2 and 6.3 in combination with $R_m = 1/\Delta G$ and Equations 2.32 and 2.33 from Chapter 2 under the requirement that $R_p > R_m$. The electrical conductance peak ΔG is obtained by the difference of the maximum value of G and the base line value at resonance frequency. To provide an exemplary calculation, the data evaluation technique is applied to the measured frequency response from Figure 6.3 and the results are listed in Table 6.1.

Conductance peak independence of the excitation voltage

One advantageous aspect of this sensing technique is that the conductance peak is independence of the excitation voltage V_{exc} . Indeed, different values in V_{exc} change the maximum amplitude of the oscillation $\max(x(t))$ and, as a consequence also the mechanical strain S . However, the variation in S and the corresponding change in the generated charges caused by the piezoelectric material changes the measured current I_{sensing} as well. Under these considerations and by taking Equation 6.1 into account, an independency of V_{exc} is assumed. To validate this assumption, sample measurements at V_{exc} ranging between 100

Table 6.2: Sample measurements of a piezoelectric actuated resonator at different excitation voltage V_{exc} in isopropanol, measured at 20°C.

V_{exc} [mV]	f_{res} [kHz]	Q [1]	R_{m} [k Ω]	L_{m} [mH]	C_{m} [fF]	ΔG [μ S]
100	166	63.6	16.97	1037	889	0.0589
200	166	63.5	17.01	1037	890	0.0588
300	166	63.3	17.08	1037	890	0.0586
400	166	63.1	17.10	1036	891	0.0585
500	166	63.2	17.06	1036	891	0.0586

to 500 mV have been carried out in isopropanol and the corresponding results are listed in Table 6.2.

6.2 Laser Doppler vibrometry

Laser Doppler vibrometry is a widely used, ultra-precise characterization method in the field of vibrating MEMS and NEMS enabling contactless displacement and velocity measurements of vibrating surfaces. In this thesis, a Polytec[®] MSV-400 and a MSV-500 laser Doppler vibrometer (LDV) have been utilized, allowing rapid high resolution optical velocity and displacement measurements up to 1.5 and 20 MHz, respectively. The two LDVs provide adjustable laser beams allowing for scanning procedures of plate surfaces as illustrated in Figure 6.6 (a) and (b). This scanning procedure is used to gather 3D topography images of vibrating structures to identify mode shapes as it is illustrated in Figure 6.6 (c).

The key component of a LDV is an interferometer, which is used to measure the path length difference between two laser beams, enabling displacement detection. To determine the velocity of a vibrating object, the so called Doppler shift is exploited. Both measurement techniques are described in the following two sections using the block diagram depicted in Figure 6.7.

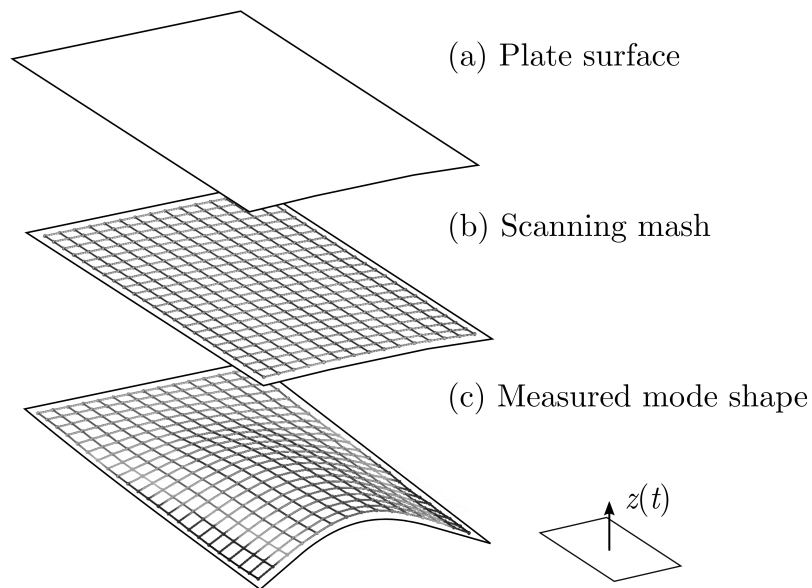


Figure 6.6: Illustration of an optical surface scan of a micro structure in (a) and a sample measurement illustration an advanced out-of-plane bending mode in (b).

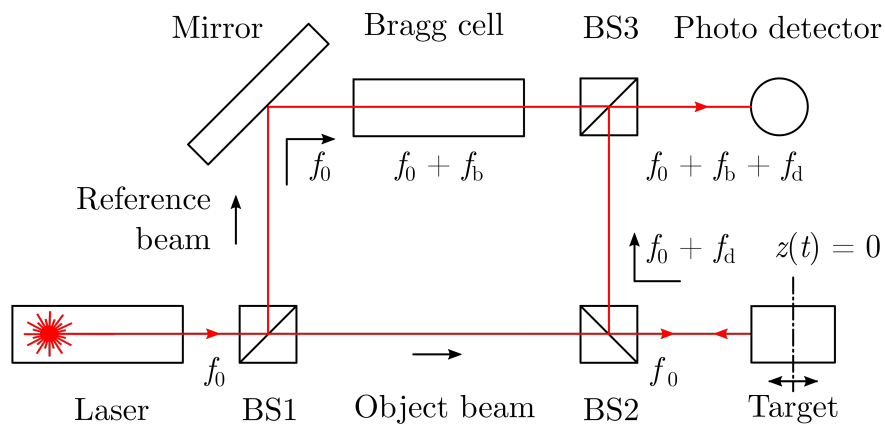


Figure 6.7: Block diagram of a laser Doppler vibrometer (LDV).

Operating principle

Displacement detection

As illustrated in Figure 6.7, a beam splitter BS1 is used to divide a coherent laser beam with a frequency f_0 into an object and a reference beam. The object beam passes another beam splitter BS2 and is focused onto the target, where the laser is scattered in all directions. The backscattered beam is deflected by BS2 and merged with the reference beam by a third beam splitter BS3 and is then directed onto the photo detector. The total intensity of the beam impinging on the detector can be described as

$$I_{\text{total}} = I_{\text{obj}} + I_{\text{ref}} + \underbrace{2\sqrt{I_{\text{obj}}I_{\text{ref}}\cos(\Delta\varphi)}}_{\text{interference term}}, \quad (6.4)$$

where I_{obj} and I_{ref} are the intensities of the corresponding beams. The so called interference term takes the phase difference $\Delta\varphi$ between object and reference beam into account and is given as

$$\Delta\varphi = 2\pi\frac{r_{\text{obj}} - r_{\text{ref}}}{\lambda_{\text{laser}}}, \quad (6.5)$$

where r_{obj} and r_{ref} are the path lengths of the corresponding beams and λ_{laser} represents the wave length of the laser. There, r_{ref} is constant over time. In the case of a change in the object displacement $z(t)$, a change in the path length r_{obj} occurs. Consequently, the total intensity I_{total} changes and causes a shift in the characteristic dark/bright pattern on the detector. Thereby, a complete dark/bright shift corresponds to an object displacement of exactly half of λ_{laser} , which is in the case of a helium neon laser a displacement of 316 nm. By counting the dark/bright pattern in combination with suitable interpolation techniques, displacements can be detected down to the pm range. As object movements towards the interferometer causes the same change in the interferometer pattern as object movements away from the interferometer, the direction of the moving object cannot be determined. For this purpose, an acousto-optic modulator, also known as Bragg-cell, is placed in the reference beam as illustrated in Figure 6.7. The Bragg-cell adds a frequency shift f_b of 40 MHz, which is shifted to higher frequencies, when the object moves towards the interferometer and is shifted to lower frequencies, when the object moves away from the interferometer. Using

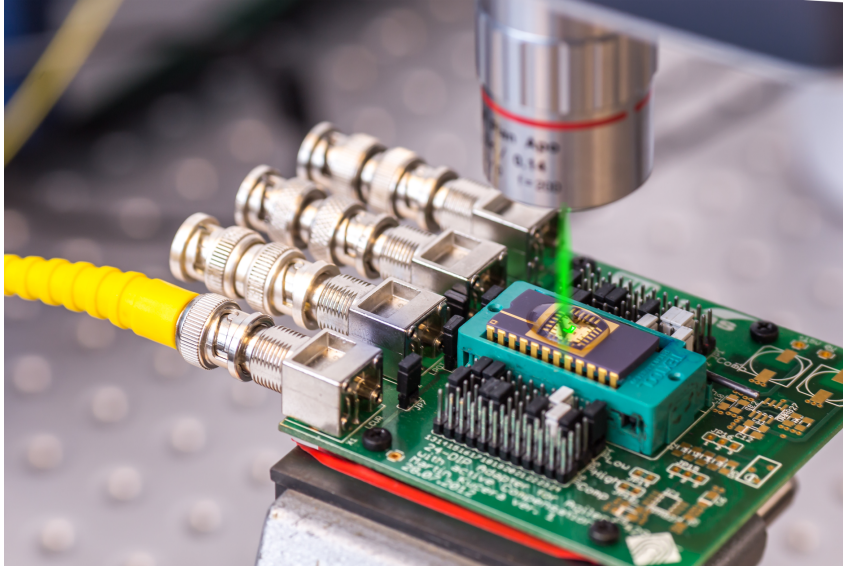


Figure 6.8: Picture of a typical laser Doppler vibrometer measurement.

this technique the direction of movement can be determined.

Velocity detection

In the case of a vibration object in z -direction, the frequency shift f_d of the laser is directly proportional to the velocity of the object. This is also known as Doppler shift and can be written as

$$f_d = 2 \frac{\dot{z}(t)}{\lambda_{\text{laser}}}, \quad (6.6)$$

where $\dot{z}(t)$ is the velocity of the object in z -direction as a function of time and λ_{laser} is the wavelength of the reflected laser beam. The reflected beam is backscattered and deflected towards the detector as described in Section 6.2, but this time with a frequency modulated Doppler shift $f_0 + f_d$. Finally, the Doppler frequency f_d can be extracted from the interferometry pattern on the detector and is converted into a voltage. Using these two methods, both, the displacement and the velocity of vibrating structures can be detected. A picture of a typical laser Doppler vibrometer measurement is illustrated in Figure 6.8.

Chapter 7

Performance of resonators operating at higher order modes in liquids

Parts of this chapter have already been published in Ref. [109]

It is the objective of this chapter to critically discuss the performance of piezoelectrically excited resonators operated at higher order modes in different liquids. Therefore, single-side clamped resonators are fabricated and excited in special out-of-plane bending modes and studied in terms of their responsibility and sensitivity. This class of vibration modes is called *roof-tile shaped modes* and features very high quality factors in liquid media and high surface strain values. To exploit the full potential of these higher order modes, a tailored electrode patterning is applied and is illustrated by means of finite element analysis. The presented approach ensures both, high quality factors in liquids in combination with high signal to noise values ($Q \sim 170$; $\text{SNR} \sim 10^4$ for the 10th order mode in sample fluid with dynamic viscosity of 5 mPa·s). The responsivity and sensitivity are investigated for the resonance frequency, the quality factor and for the electrical conductance peak, showing a decreasing relative responsivity for the resonance frequency, whereas the relative responsivity of the quality factor and the electrical conductance peak remain constant over the investigated mode range. The sensitivity evaluation yields an improved sensitivity of the resonance frequency by a factor of ~ 30 , when comparing the 1st and 10th order mode. Even higher factors of ~ 50 are obtained for the quality factor and the conductance peak, respectively.

7.1 Introduction

For most resonator-based sensing applications, a high intrinsic quality factor is desirable to ensure accurate determination of the resonance frequency. Recently, Kucera *et al.* introduced a special excitation mode [38], achieving high quality factors in liquid environments compared to commonly used out-of-plane bending vibration modes. Higher orders of this so called roof tile-shaped mode exhibit quality factors over 300 in deionized water at ~ 3.5 MHz [39]. This increase in the quality factor can be explained as with increasing mode number viscous forces decrease and hence, viscous damping became less dominant as already discussed in Chapter 4. When aiming for the sensing of physical properties of fluids such as density and viscosity, however, often the quality factor itself is utilized as measurand [105, 110–112]. In such a case, it is of particular interest, how higher order modes and the corresponding decrease in viscous forces affect the sensing performance of micromachined resonators in liquids, which is explicitly investigated in the following sections.

7.2 Terminology: Responsivity and sensitivity

To classify the performance of sensor elements often the responsivity \mathcal{R} and the sensitivity \mathcal{S} are utilized. Since the terminology differs from field to field, the specific terminology used in this thesis and in Ref. [13] is introduced. The responsivity \mathcal{R} is the slope of the sensor output as a function of the sensor input over a linear range and can be expressed as

$$\mathcal{R} = \frac{\Delta\text{output}}{\Delta\text{input}}. \quad (7.1)$$

The sensitivity \mathcal{S} is the smallest detectable change of the sensor input with respect to a specific signal to noise ratio and is expressed as

$$\mathcal{S} = \Delta\text{input}_{\min} = \frac{\Delta\text{output}_{\min}}{\mathcal{R}}, \quad (7.2)$$

where $\Delta\text{output}_{\min}$ is the smallest detectable output value and is limited by the noise of the system. In this work, $\Delta\text{output}_{\min}$ is defined as the standard deviation of the sensor output. $\Delta\text{output}_{\min}$ is often given in its relative notation $\delta\text{output}_{\min}$ in parts per million (ppm) or parts per billion (ppb) and the

sensitivity can then be expressed as

$$\mathcal{S} = \frac{\delta \text{output}_{\min}}{\delta \mathcal{R}}, \quad (7.3)$$

where $\delta \mathcal{R}$ is the relative responsivity with respect to a certain output value. As already mentioned in Chapter 1, three different sensor output parameters are in the center of interest in this thesis. These are the resonance frequency f_{res} , the quality factor Q and the electrical conductance peak ΔG . With the special focus on liquid sensing, the input parameter investigated in this chapter is the inverse viscosity-density product χ which is defined as

$$\chi = \frac{1}{\sqrt{\rho_{\text{fluid}} \cdot \mu_{\text{fluid}}}}, \quad (7.4)$$

where ρ_{fluid} and μ_{fluid} are the mass density and the dynamic viscosity of the investigated fluid, respectively.

7.3 Design considerations and methods

In this chapter the first 10 orders of the so called roof tile-shaped mode are investigated. The corresponding mode shapes are simulated utilizing finite element modeling (FEM) and are illustrated in side view in Figure 7.1 and in front view as well as in top view in Figure 7.2. From the front view of the 1st order mode in Figure 7.2 (a) can be seen that there is no point of inflection in the mode shape along the x-axis, with the consequence of no change in the sign of curvature. The second order mode of the roof tile-shaped mode is depicted in Figure 7.2 (b), showing one point of inflection in the front view leading to an additional nodal line along the center of the plate in y-direction and hence, to a change in the sign of curvature. Higher orders continue this series and the number of nodal lines increases, as illustrated in Figure 7.2 (c-j). To classify these special out-of-plane modes, Leissa's nomenclature [113] is used and the number of nodal lines in y- and x-direction are counted, identifying the fundamental mode in (a) as 12-mode, the first harmonic in (b) as 13-mode, (c) as 14-mode, etc.. Due to the changes in curvature of the mode shape also the sign of the local top surface strain is changing, which is indicated in Figure 7.2 by blue (“-“, compressive) and red (“+“, tensile) color. With respect to potential piezoelectric sensing applications, this change in the sign of the surface strain along the x-axis favors

the realization of separated, tailored electrodes along the y-axis, as reported in Ref. [109, 114], which are indicated by black rectangles in Figure 7.2. This approach leads to the required amount of electrodes $n_{\text{electrodes}} = n_{\text{nodal_lines}} - 1$, where $n_{\text{nodal_lines}}$ is the number of nodal lines along the x-axis. The position of the nodal lines and the dimensions of the electrode patterning are estimated using the Euler–Bernoulli beam theory as described in Chapter 2. To quantify this concept experimentally, piezoelectric plate-type resonators with a length $L_{\text{plate}} = 2524 \mu\text{m}$, a width $W_{\text{plate}} = 1274 \mu\text{m}$ and a thickness of $T_{\text{plate}} = 20 \mu\text{m}$ are fabricated using the fabrication guidelines presented in Chapter 5. For actuating and sensing, an aluminium nitride (AlN) thin film with a thickness of $1 \mu\text{m}$ is sputter deposited onto the plates sandwiched between 500 nm thin gold electrode stripes. For every mode order shown in Figures 7.1 and 7.2, a separate resonator with the corresponding electrode patterning is fabricated. In Figure 7.3 an optical micrograph of a typical die layout ($6 \times 6 \text{ mm}^2$) packaged in a 24-pin DIP (dual inline package) is illustrated for a single-side clamped resonator with 9 tailored electrode stripes for the 10th order mode, as shown in Figure 7.2 (j) with the corresponding top view as an inset. The fabricated resonators are immersed in several model solutions from Paragon Scientific (D5, N10, N35, N100 and D500) and are characterized electrically utilizing an Agilent 4294A impedance analyzer (excitation voltage $V_{\text{exc}} = 500 \text{ mV AC}$). The corresponding properties of these model solution are given in the Appendix A.1. A detailed description about the measurement technique is given in Chapter 6. As mentioned above, three key sensor output parameters are in the center of attention. These are the resonance frequency f_{res} , the quality factor Q , and the electrical conductance peak ΔG . To maximize the sensor response in terms of the conductance peak, the tailored electrode stripes from Figure 7.2 are separately read out such that all tensely and all compressively strained areas are connected. This technique ensures the collection of all piezoelectrically generated charges without cancellation as published in Ref. [109].

7.4 Electrical characterization in liquids

Signal to noise ratio (SNR)

The measurement procedure presented in the previous section and in Chapter 6 is used to evaluate the frequency responses of the first 10 order modes of

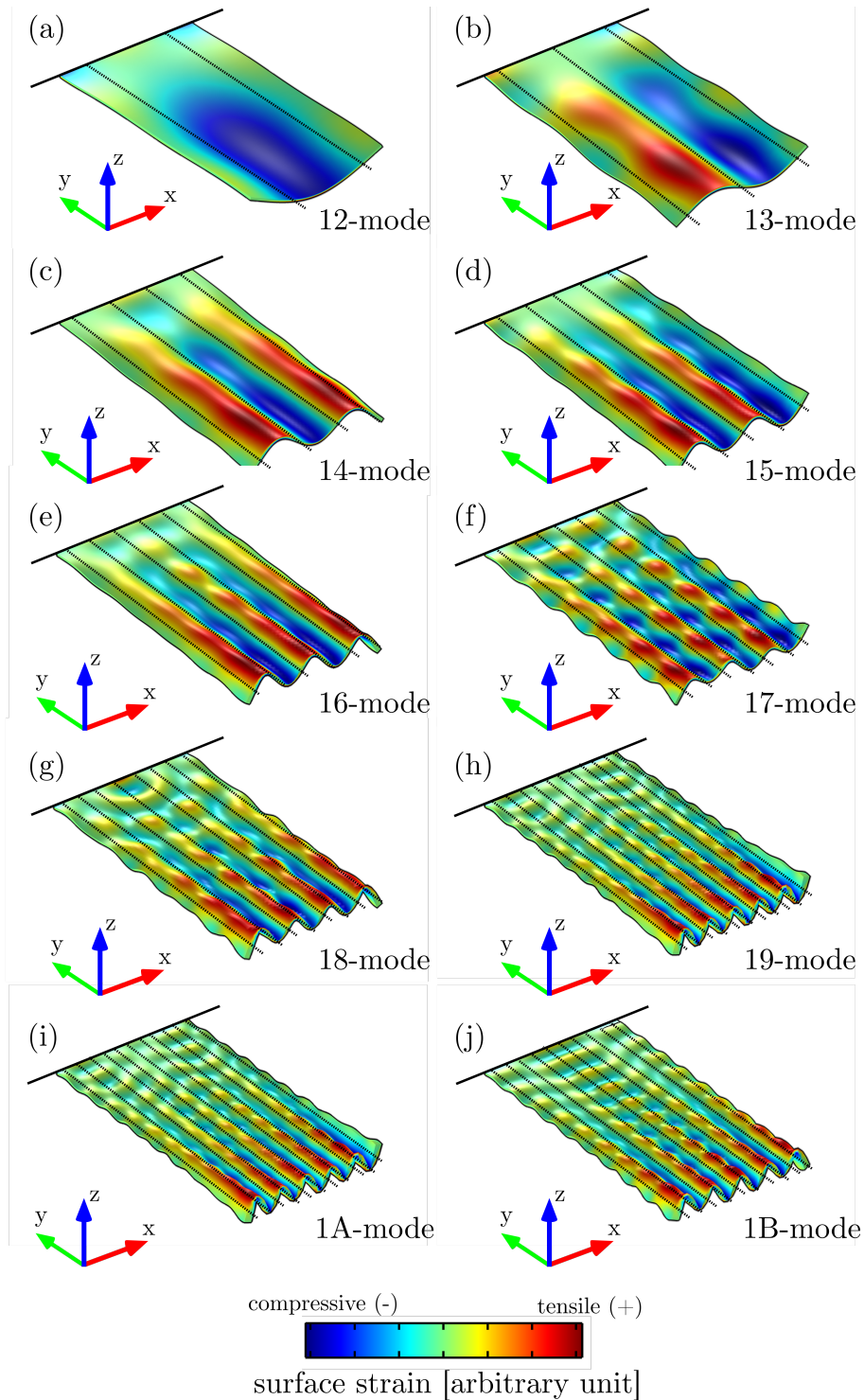


Figure 7.1: Cross-section illustration of FEM eigenmode analysis for the first ten orders (a-j) of the roof tile-shaped mode of single-side clamped plates ($2524 \times 1274 \times 20 \mu\text{m}^3$).

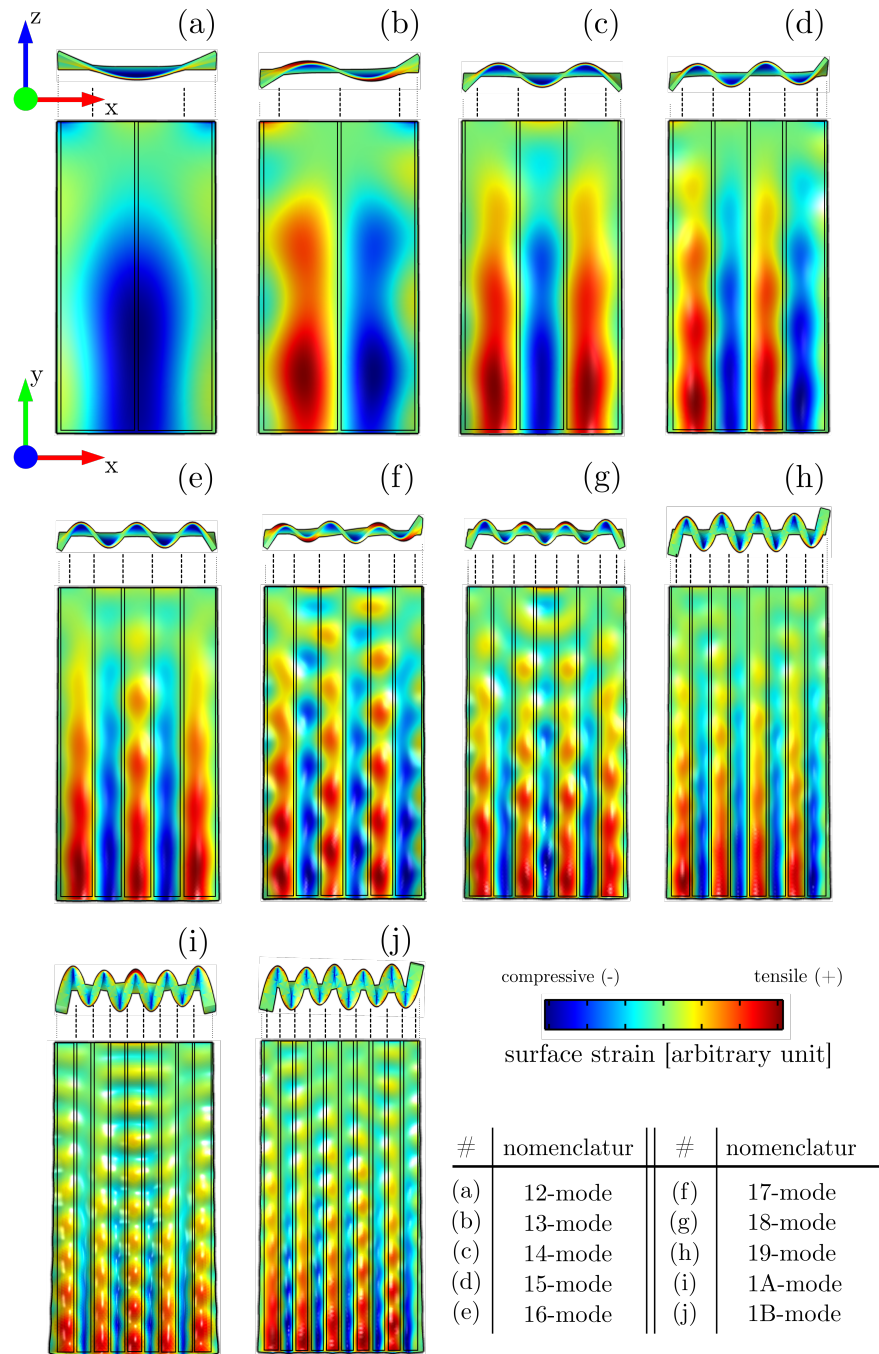


Figure 7.2: Illustration of FEM eigenmode analysis for the first ten orders (a-j) of the roof tile-shaped mode of single-side clamped plates ($2524 \times 1274 \times 20 \mu\text{m}^3$) both in front (upper) and top view (lower).

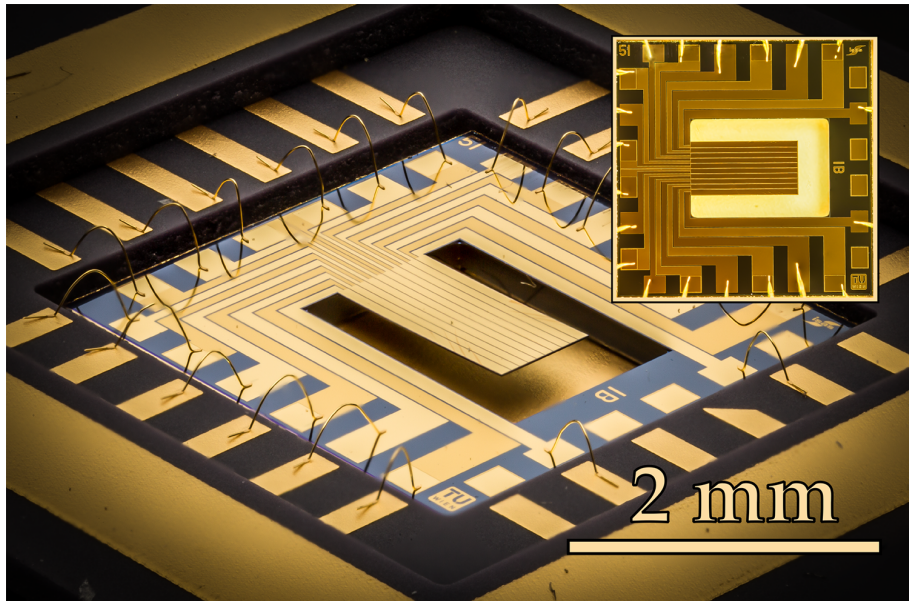


Figure 7.3: Optical micrograph of a typical die layout ($6 \times 6 \text{ mm}^2$), packaged and wire bonded in a 24-pin dual in line package, containing one single-side clamped plate ($2524 \times 1274 \times 20 \mu\text{m}^3$) with an electrode design optimized for the 10th order (1B-mode).

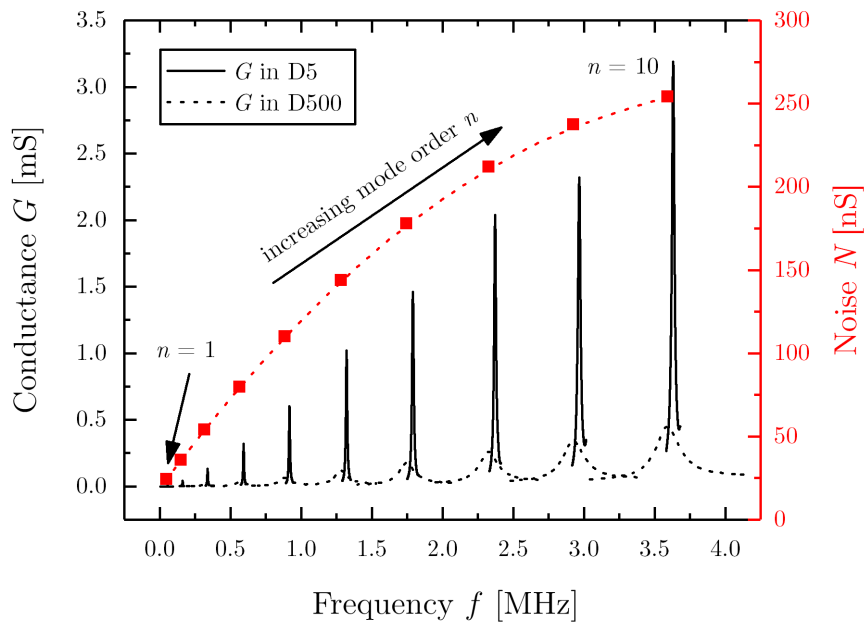


Figure 7.4: Conductance and noise characteristics for the first ten orders of the roof tile-shaped mode in D5 and D500 at 20°C .

Table 7.1: Mode dependency of the resonance frequency f_{res} , the quality factor Q , the electrical conductance peak ΔG and the ratio $\Delta G/Q$ measured in D5 at 20°C. The values in the last column are reference values taken from Ref. [39]

#	f_{res} [kHz]	Q [1]	ΔG [mS]	SNR [1]	$\Delta G/Q$ [μS]	$\Delta G/Q$ [39] [μS]
1	55.69	25	0.006	$2.19 \cdot 10^2$	0.24	0.126
2	162.17	44	0.040	$1.07 \cdot 10^3$	0.90	0.791
3	338.79	62	0.13	$2.36 \cdot 10^3$	3.73	0.393
4	593.44	85	0.32	$3.89 \cdot 10^3$	5.81	0.0517
5	918.00	102	0.59	$5.31 \cdot 10^3$	8.13	0.454
6	1321.70	123	1.00	$6.91 \cdot 10^3$	11.27	1.22
7	1790.69	129	1.45	$8.10 \cdot 10^3$	13.49	0.540
8	2372.12	146	1.97	$9.26 \cdot 10^3$	14.24	0.0742
9	2967.05	138	2.23	$9.37 \cdot 10^3$	16.21	0.438
10	3631.54	171	3.03	$1.19 \cdot 10^4$	17.73	1.211

the roof tile-shaped modes in D5, N10, N35, N100 and D500. As being representative for similar measurements at other liquids, the results obtained in D5 and D500 are compared in Figure 7.4. It can be seen, that the frequency response in D5 are sharp and obtain high values in ΔG . In contrast, significantly wider and lower conductance peaks are obtained in the more viscous fluid D500, leading to a hardly measurable conductance peaks for low mode numbers n . As expected, the strain related conductance peak ΔG increases with increasing mode number. This results in a ~ 500 times higher value in ΔG for the 10th order mode at ~ 3.5 MHz compared to the first order mode at ~ 50 kHz for both liquids. The noise level represented by the standard deviation of the entire system also increases with increasing frequency, resulting in 20 nS at 100 kHz and 260 nS at 4 MHz as it can be seen in Figure 7.4. By comparing the conductance peaks with the corresponding noise levels, a ~ 50 times higher signal to noise (SNR) ratio is achieved for the 10th order compared to the first order mode. A compact overview of the results gathered in D5 for all investigated mode orders is listed in Table 7.1. It can be seen, that besides the resonance frequency f_{res} and the conductance peak ΔG , also the quality factor Q , the ratio $\Delta G/Q$ and the SNR increases, which is in excellent agreement with literature [115]. The highest value of the signal to noise ratio is obtained for the 1B-mode ($\text{SNR}_{1\text{B-mode}} = 1.19 \cdot 10^4$). Additionally, the ra-

tios $\Delta G/Q$ are compared to similarly performed measurements in DI-H₂O of identically constructed resonators of the same size from Ref. [39]. Basically, the measurements of the 12 and 13-mode are performed with the same electrode configuration as in Ref. [39], thus obtaining similar results in the $\Delta G/Q$ values. However, significantly higher values are obtained for the 4th to 10th order modes, which are achieved by fully exploiting the tailored electrode design for each mode, resulting in up to 200 times higher $\Delta G/Q$ values (19-mode) compared to those published in Ref. [39]. For the sake of completeness, a detailed collection, including all f_{res} , Q , ΔG and $\Delta G/Q$ values for all investigated modes and fluids is listed in the Appendix A.3

Responsivity

In Figure 7.5 the three sensor output parameters resonance frequency f_{res} , the quality factor Q and the conductance peak ΔG are plotted as a function of the mode number n . In (a) the resonance frequency is normalized to the resonance frequency in air $f_{\text{res}}(\text{air})$, showing a decreasing spread in the $f_{\text{res}}(\text{fluid})/f_{\text{res}}(\text{air})$ values for varying χ in different liquids with increasing mode order, which indicates a decreasing responsivity for increasing values of n . Contrary results are obtained for Q and ΔG , as can be seen in Figures 7.5 (b) and (c). These results fit very well to the theoretical model reported by Van Eysden and Sader [115]. They predict a decrease in viscous forces for increasing mode number n as already elaborated in Chapter 4. To illustrate the responsivity of the sensor output parameters as shown in Equation (1), $f_{\text{res}}(\text{fluid})$, Q and ΔG are plotted over the sensor input χ in Figure 7.5 (d-f). It can be seen, that $f_{\text{res}}(\text{fluid})/f_{\text{res}}(\text{air})$ in (a) exhibits a non-linear behavior over the investigated χ range. Therefore, two separate responsivities for $f_{\text{res}}(\text{fluid})$ are estimated for $\chi < 0.14$ and $\chi > 0.14 \text{ (mPa}\cdot\text{s}\cdot\text{kg/l)}^{-0.5}$, respectively. For Q and ΔG , however, a linear behavior and hence, a constant responsivity across the entire χ -range is determined, as it is illustrated in Figures 7.5 (e) and (f). Furthermore, the responsivities in (e) and (f) are increasing with increasing mode number n . In Figure 7.6 the relative responsivities for $f_{\text{res}}(\text{fluid})$, Q and ΔG are depicted as a function of mode number n . Doing so, all three output parameters are normalized to the corresponding value in the viscosity standard D5. It can be seen, that the relative responsivities of $f_{\text{res}}(\text{fluid})$ for low and high values of χ decrease over n as already shown in Figure 7.5 (d). Despite the reduction in viscous forces

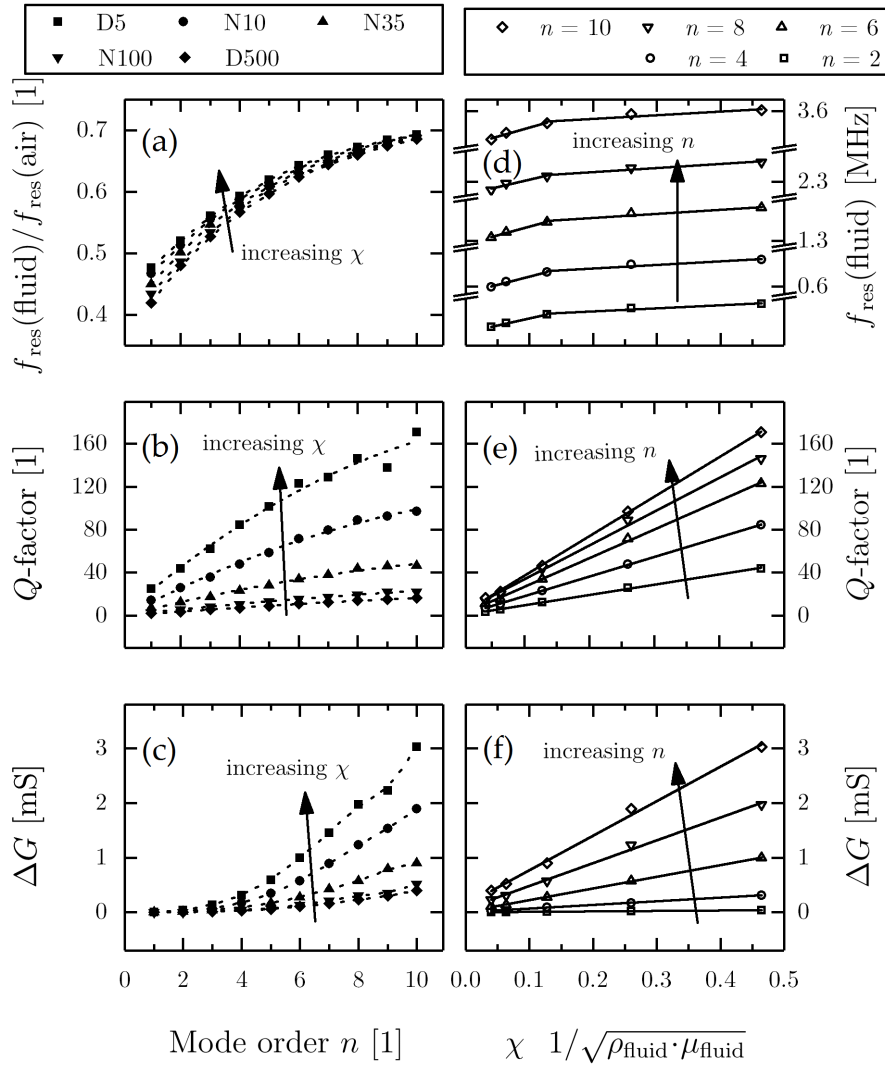


Figure 7.5: Sensor output parameter ($f_{\text{res}}(\text{fluid})/f_{\text{res}}(\text{air})$, quality factor Q and electrical conductance peak ΔG) over the mode order n for all investigated liquids (i.e. D5, N10, N35, N100 and D500) in (a-c) and over the sensor input parameter χ for even order modes in (d-f), respectively.

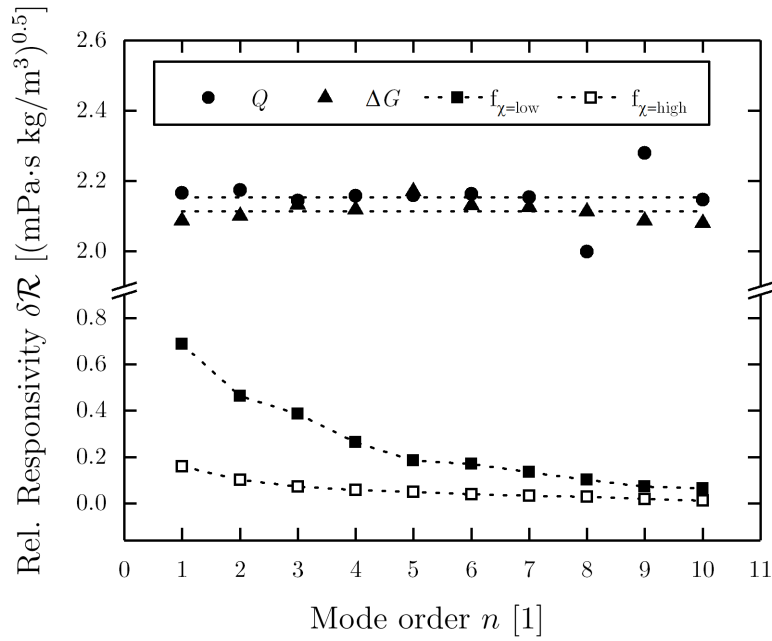


Figure 7.6: Relative responsivity grouped into the two resonance frequency regimes (i.e. $f_{\chi=\text{low}}$ and $f_{\chi=\text{high}}$), the quality factor Q and the conductance peak ΔG over the mode order n . The dashed lines serve as guide to the eye.

for higher mode numbers [115], the relative responsivity for Q and ΔG stays constant.

Sensitivity

To determine the minimal sensitivity, the experimental data are fitted as described in Chapter 6 and then mathematically superimposed by artificially computed white Gaussian noise. This method allows the generation of frequency responses with SNR values between 1 and 50000. Additionally, the quality factor is adjusted between 1.5 and 500 by manually changing the equivalent resistance R_m . These calculations are computed using *MATLAB*[®] and the most important code snippet is given in the Appendix A.4. A representative artificially noised frequency response for three different SNR values is presented in Figure 7.7. The evaluation procedure, presented in Chapter 6, is again applied to the artificially noised data sets for 2500 times, causing relative standard deviations σ for Q , ΔG and f_{res} , which are equal to δoutput . The results are illustrated as contour plots in Figure 7.8 (a-c). In addition representative histograms at $\text{SNR} = 200$ and $Q = 25$ are depicted for f_{res} in Figure 7.8 (d), for

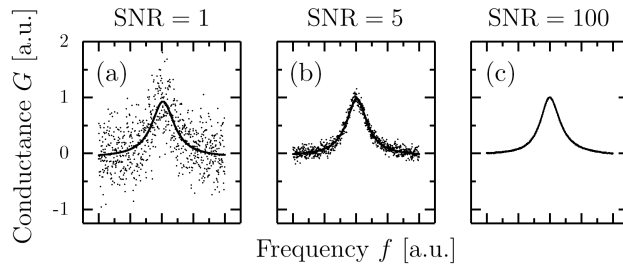


Figure 7.7: Frequency response with artificially generated white Gaussian noise for (a) SNR = 1, (b) SNR = 5 and (c) SNR = 100.

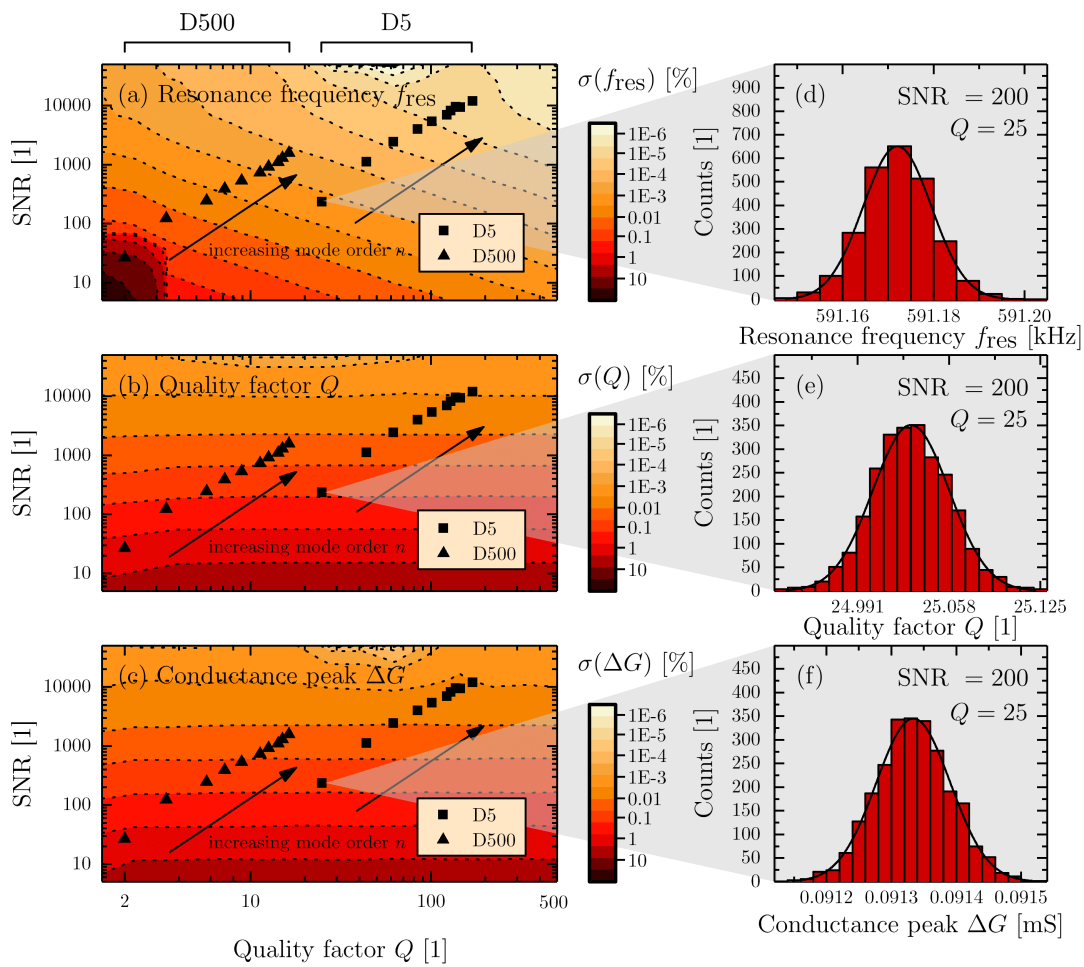


Figure 7.8: Relative standard deviations σ over SNR and quality factor of the resonance frequency in (a), the quality factor in (b) and the conductance peak in (c) and representative histograms at SNR = 200 and $Q = 25$ in (d), (e) and (f).

Q in Figure 7.8 (e) and for ΔG in Figure 7.8 (f). The relative standard deviation for the resonance frequency $\sigma(f_{\text{res}})$ decreases for increasing values of both SNR and Q , as shown in Figure 7.8 (a). For relative standard deviation of the quality factor $\sigma(Q)$ in (b) and the conductance peak $\sigma(\Delta G)$ in (c), however, no dependency with respect to the quality factor is observed. This result, in combination with the constant relative responsivity from Figure 7.6, indicates, that for sensing of fluid properties such as density and viscosity, where the quality factor itself is utilized as measurand, the absolute value of Q is irrelevant for the sensitivity of the sensor element, as long as $Q > 1$. Furthermore, the actual values in SNR and Q for all investigated modes in D500 and D5 are highlighted in Figure 7.8, indicating, that higher order modes obtain significantly lower σ values for all three parameters (f_{res} , Q and ΔG). These values are considered to calculate the actual sensitivities of the investigated resonators using Equation 7.3 and the corresponding results are depicted in Figure 7.9. Basically, the sensitivity in f_{res} can be improved by a factor of ~ 30 for both regimes ($f_{\chi=\text{low}}$ and $f_{\chi=\text{high}}$), when comparing 1st and 10th order mode in D5. The sensitivity in Q and ΔG are improved by factors of ~ 50 . These results let conclude, that higher orders of the roof tile-shaped yield an enhanced sensitive response as they are associated with higher resonance frequency values, quality factors and the conductance peak heights, respectively.

Performance limitations of higher order modes

The performance increase, enabled by the consideration of higher order modes is limited due to certain sound dissipation effects via the surrounding liquid media as theoretically described in Chapter 4. The likelihood of this effect is directly correlated with the mode order and the density of the surround fluid. For every resonator design, operating at higher order modes in liquid media it is therefore of particular interest, at which mode number sound dissipation becomes important and how it affects the frequency response of the resonator. To experimentally quantify this energy loss mechanism, resonators are excited up to the 16th order mode in N1 and D5, two solutions with relatively low density values of 0.785 kg/l and 0.840 kg/l at 20°C. In Figure 7.10 the obtained quality factors are illustrated, showing a significant decrease in the quality factor Q at the critical mode numbers $n_{\text{crit}} = 8$ for N1 and 9 for D5, and a subsequently increase in Q at $n = 10$ in N1 and 12 in D5, which is in excellent agreement with

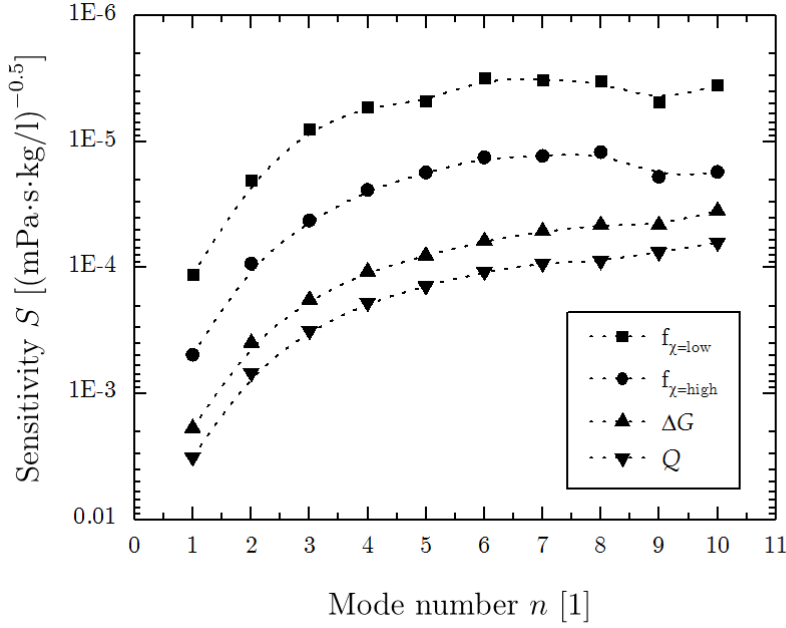


Figure 7.9: Sensitivity \mathcal{S} over mode order n for the two resonance frequency regimes ($f_{\chi=\text{low}}$ and $f_{\chi=\text{high}}$), for the conductance peak ΔG and for the quality factor Q in D5 at 20°C. The dashed lines serve as guide to the eye.

the results presented in Ref. [93]. Due to the fact, that $n_{\text{crit}}(\text{D5})$ is higher than $n_{\text{crit}}(\text{N1})$, it can be concluded, that for liquids with even higher density values such as N10, N35, N100 or D500, sound dissipation effects occur not before n outreaches values > 10 . However, great potential of this usually unwanted effect can be extracted when a detailed information of the compressibility of the investigated liquid is available. As it can be seen in Figure 7.11, the margin between the two normalized angular frequencies $1 - \frac{\omega_{\text{res}}(\text{fluid})}{\omega_{\text{res}}(\text{air})}$ for D5 and N1 is much higher for $n > n_{\text{crit}}$ compared to $n < n_{\text{crit}}$, which indicates an increased responsivity in the resonance frequency for the regime: $n > n_{\text{crit}}$.

7.5 Conclusions

In summary, the responsivity and sensitivity of the first 10 orders of the roof tile-shaped mode in piezoelectrically excited MEMS resonators have been studied in different liquids. To avoid charge compensation of the electrical response for higher order modes, a tailored electrode design is applied and is illustrated by FEM eigenmode analyses. MEMS resonators based on sputter-deposited alu-

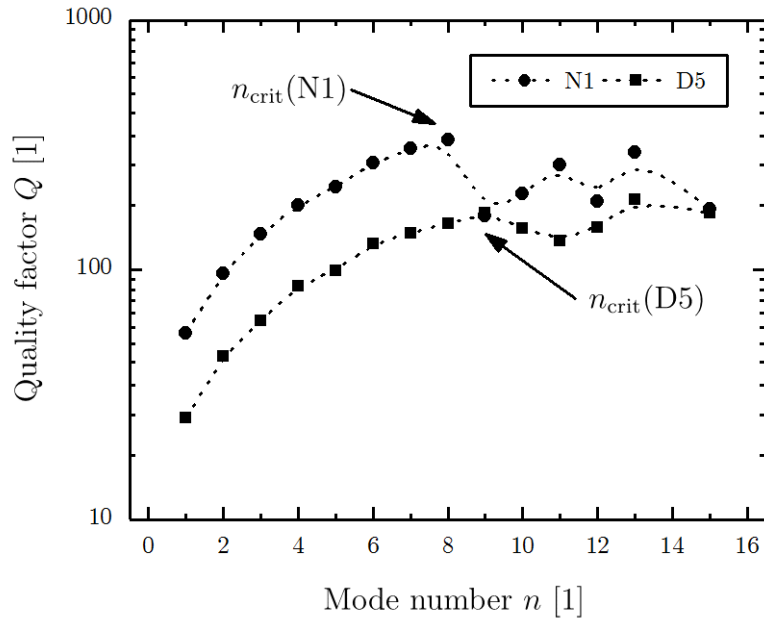


Figure 7.10: Quality factor Q over mode number n in D5 and N1 at 20°C. The dashed lines serve as guide to the eye.

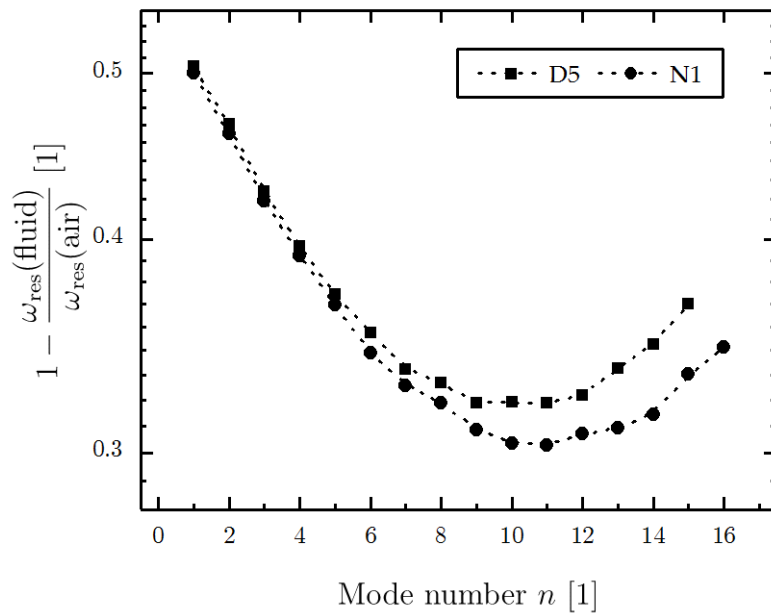


Figure 7.11: Normalized angular frequency over mode number n in D5 and N1 at 20°C. The dashed lines serve as guide to the eye.

minium nitride thin films serving for both excitation and electrical read-out by measuring the admittance spectrum were fabricated and characterized in several liquids with a dynamic viscosity range from 5 mPa·s up to 700 mPa·s. Quality factors above 170 in sample fluid D5 were achieved for the 10th order mode. A decreasing relative responsivity for the resonance frequency with increasing mode order was observed, whereas the relative responsivity of the quality factor and the electrical conductance peak stayed constant. When comparing the 1st and 10th order mode, the sensitivity in terms of resonance frequency is improved by a factor of ~ 30 , whereas the sensitivity in quality factor and the conductance peak are improved by a factor of ~ 50 . However, significant sound dissipation effects were observed for liquids with low density values at mode number $n > 8$. All in all, the constant relative responsivity and the increased sensitivity for higher order modes predestine the presented sensing concept for a broad range of applications, such as the precise sensing of any change in resonator mass even in liquid media.

Chapter 8

Performance of resonators operating with different anchor designs in liquids

Parts of this chapter have already been published in Ref. [116]

In the previous chapter it was shown, that the performance of piezoelectrically actuated resonators in liquid environments can be improved by the consideration of higher orders of the so called roof tile-shaped mode (1X-modes). These higher order modes, in combination with a tailored electrode design lead to increased values of the quality factor Q , the electrical conductance peak ΔG , the signal to noise ratio SNR and the piezoelectric response $\Delta G/Q$. To further enhance the performance of such a type of resonator in liquid media, different clamping conditions have been investigated and the results are presented in this chapter. To validate the different clamping conditions experimentally, piezoelectrically actuated MEMS resonators have been fabricated with clamped-free, clamped-clamped and quasi free-free support boundary conditions. The different resonators are compared using finite element method (FEM) analysis in combination with electrical and optical characterization, resulting in an increased piezoelectric response by $\sim 20\%$ for the resonator with quasi free-free support compared to that with a standard clamped-free support.

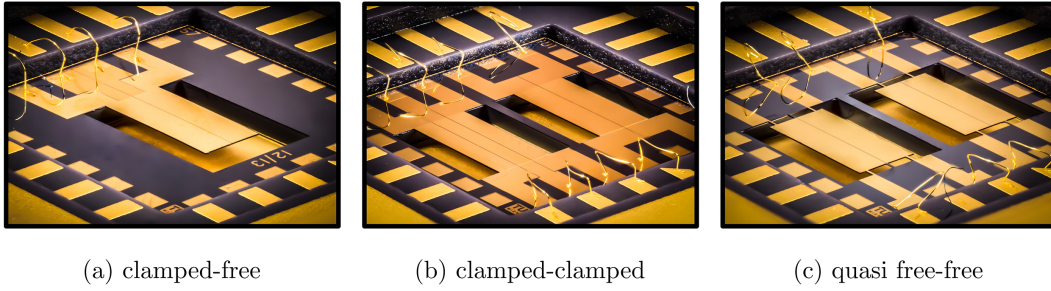


Figure 8.1: Optical micrographs of piezoelectrically actuated plate-type resonators with a length of $L_{\text{plate}} = 2524 \mu\text{m}$, a width of $W_{\text{plate}} = 1274 \mu\text{m}$, a thickness of $T_{\text{plate}} = 20 \mu\text{m}$ but with three different clamping conditions.

8.1 Design considerations

The micromachined plate-type resonators investigated in this chapter are fabricated considering the fabrication guidelines presented in Chapter 5. The manufactured piezoelectrically actuated plates feature a length of $L_{\text{plate}} = 2524 \mu\text{m}$, a width of $W_{\text{plate}} = 1274 \mu\text{m}$, a thickness of $T_{\text{plate}} = 20 \mu\text{m}$ and exhibit three different support boundary conditions (i.e. clamped-free, clamped-clamped and quasi free-free). Optical micrographs of the finished fabricated, packaged and wire-bonded devices for all three clamping conditions are illustrated in Figure 8.1. The corresponding patterning of the electrodes is designed to actuate both the 1st and 2nd order of the roof tile-shaped mode, resulting in two separated electrodes, each with a length of $2494 \mu\text{m}$ and a width of $617 \mu\text{m}$. The resonator in the foreground of Figure 8.1 (b), featuring three electrodes, has not been used within this thesis. In Figure 8.2 FEM analysis of the mode shapes of the 1st and 2nd order mode are illustrated for clamped-free ((a) and (d)), clamped-clamped ((b) and (e)) and quasi free-free ((c) and (f)) support boundary conditions. The colored surface shading represents the mechanical strain and thus, the piezoelectrically generated surface charge distribution, as described in Chapter 7. Using Leissa's nomenclature [113] by counting the number of nodal lines in y- and x-direction, these modes are named 1X-modes (see Figures 8.2 (a), (d)), 2X-modes (see Figures 8.2 (b), (e)) and 0X-modes (see Figure 8.2 (c), (f)). Apparently, the mode shape of the particular modes changes with different clamping conditions. Subsequently, also the stress distribution across the plate surface changes as it is shown in the top view illustrations of the FEM analysis in Figure 8.3. For

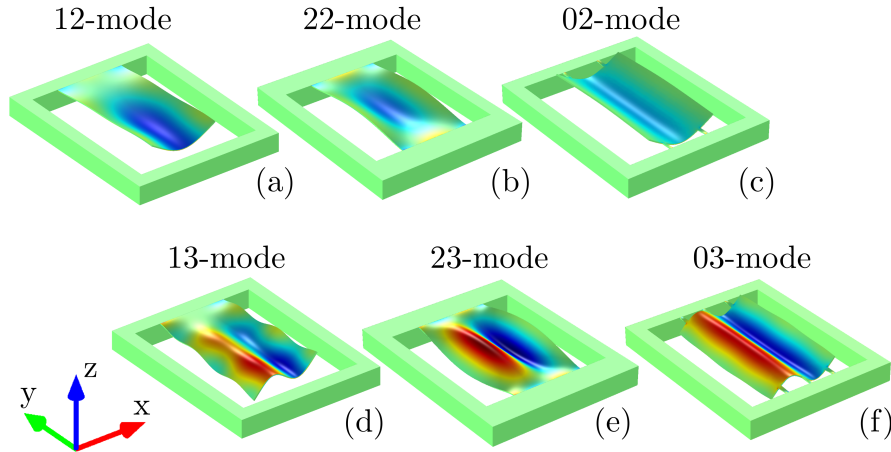


Figure 8.2: Visualization of the fundamental (a-c) roof tile-shaped modes (X2-modes) and the 2nd orders (d-e) of the roof tile-shaped mode (X3-modes) for a single-side clamped plate (a, d), a double-side clamped plate (b, e) and a free-free clamped plate (c, f), respectively. The colored areas on the cantilever surface represent the local surface strain distribution.

the clamped-free and clamped-clamped configuration, the areas with the highest strain are located only at the end and middle region of the plate surface, respectively. Only for the resonator with quasi free-free clamping (see Figure 8.3 (c), (f)), areas with high strain along the entire plate length can be achieved. The specialty of this advanced clamping condition is based on the fact that the support of the plates correlates with the position of the nodal lines of the vibration mode, enabling a quasi-free oscillation, compared to those being single-side (see Figure 8.3 (a), (d)) and double-side clamped (see Figure 8.3 (b), (e)).

8.2 Electrical and optical characterization in air

The influence of different clamping conditions have been investigated optically and electrically using a Polytec[®] MSV-400 and an Agilent[®] 4294A precision impedance analyzer, respectively. Detailed descriptions about both characterization techniques are given in Chapter 6.1. A first optical and electrical screening of all six resonators has been performed in air and the results are presented in Figure 8.4. A good match in the resonance frequencies between the optical (a) and electrical (b) characterization techniques was observed. However, sig-

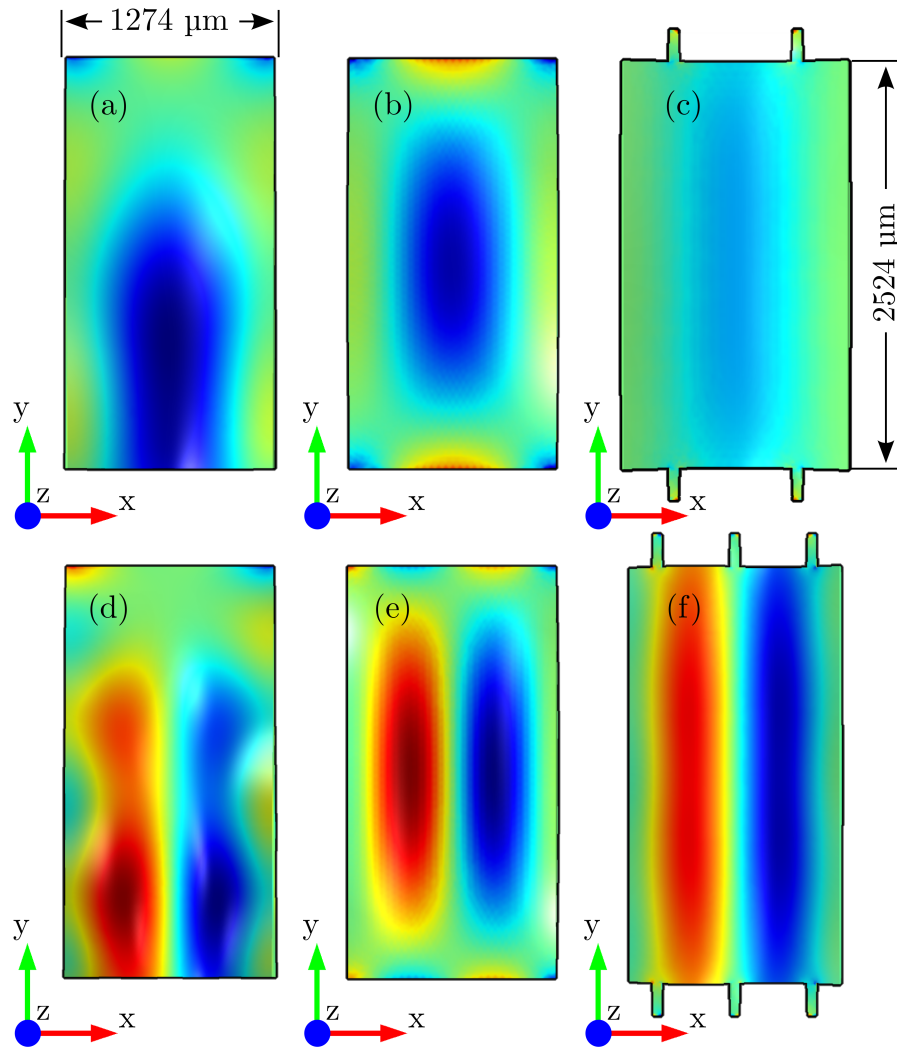


Figure 8.3: Top view of the presented roof tile-shaped modes from Figure 8.2, showing (a) the 12-mode, (b) the 22-mode, (c) the 02-mode, (d) the 13-mode, (e) the 23-mode and (f) the 03-mode. The colored areas on the plate surfaces represent the local surface strain distribution. Red indicates areas with tensile strain and blue indicates areas compressive strain, respectively.

Table 8.1: Summary of quality factor (Q), the electrical conductance peak ΔG and the piezoelectric response $\Delta G/Q$ for resonators excited in the 2nd order mode with clamped-free, clamped-clamped and quasi free-free support boundary conditions in isopropanol at room temperature.

Device	Q [1]	ΔG [μS]	$\Delta G/Q$ [μS]
clamped-free	66	41.6	0.623
clamped-clamped	67	21.2	0.316
quasi free-free	70	54.8	0.774

nificant differences in the particular peak heights were measured. The highest averaged deflection z_{avg} of 2.5 nm is obtained for the 12-mode followed by the 02-mode ($z_{\text{avg}} = 0.55$ nm) and the 22-mode ($z_{\text{avg}} = 0.4$ nm). As already mentioned in the previous section of this chapter, the strained areas for the 12/13-mode and 22/23-mode are located only at the end and middle region of the plate, respectively. Subsequently, the regions close to the anchors experience only minimal deflection and hence, less mechanical strain, leading to relatively low values in the electrical conductance peaks ΔG for the 12/13- and 22/23-mode. The highest values in ΔG are obtained for the 02- and 03-mode as shown in Figure 8.4 (b). It is important to mention, that increased values in z_{avg} do not guarantee increased values in ΔG as it can be seen by the comparison between the individual peak in Figure 8.4 (a) and (b).

8.3 Electrical characterization in liquid media

To investigate the influence of the clamping condition on the performance in liquid media, the resonators are characterized in several liquids such as isopropanol, D5, N10, N100 and D500. The corresponding density and viscosity values for all liquids are listed in the Appendix in Section A.1. In a first experiment, resonators with clamped-free, clamped-clamped and quasi free-free support are completely immersed in isopropanol and actuated in the 2nd order of the roof tile-shaped mode. The corresponding results are listed in Table 8.1, showing the highest value in ΔG for the resonator with quasi free-free support. The quality factors range in a narrow span from 66 for the clamped-free up to 70 for the quasi free-free supported resonator. Therefore, it can be concluded that the different clamping conditions make a minor contribution to

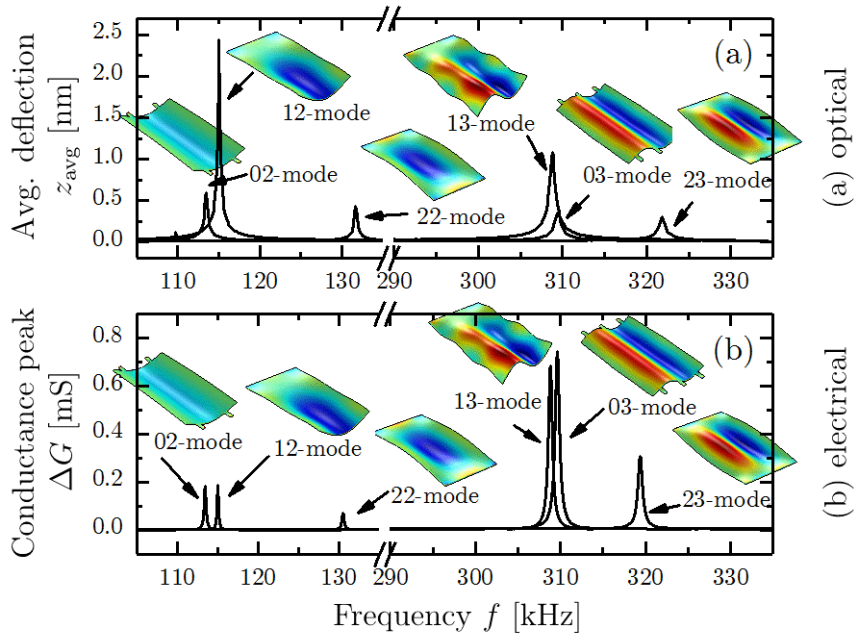


Figure 8.4: Optical (a) and electrical (b) characterization of the X2- and X3-mode in air.

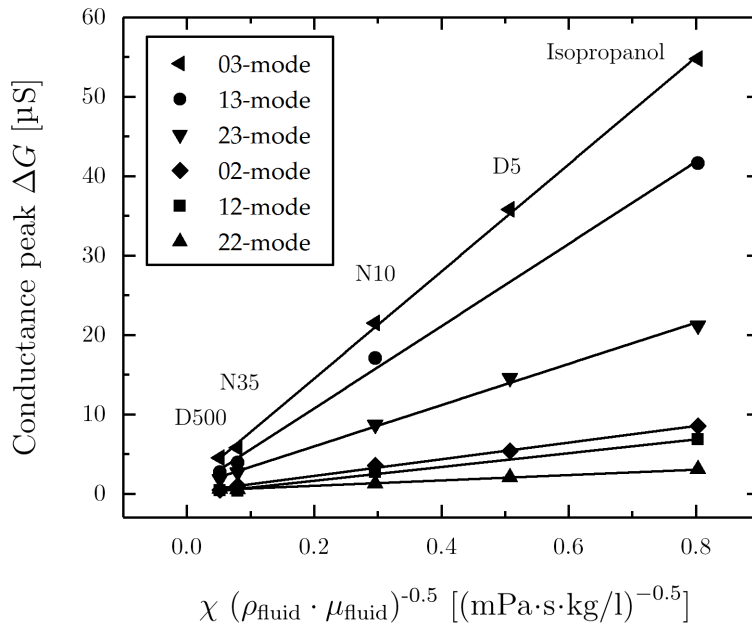


Figure 8.5: Electrical characterization of the X2- and X3-modes in different liquids represented by the conductance peak ΔG as a function of the inverse viscosity-density square root product.

the overall damping. By considering the piezoelectric response $\Delta G/Q$ in Table 8.1, it is obvious, that an increase of $\sim 20\%$ for the quasi free-free supported resonator could be achieved, when compared to the clamped-free supported resonator. In Figure 8.5 the conductance peak ΔG over $\chi = (\rho_{\text{fluid}} \cdot \mu_{\text{fluid}})^{-0.5}$ is presented, where ρ_{fluid} and μ_{fluid} represent the density and dynamic viscosity of the fluid. Superior performance for the 03-mode and the highest value in ΔG of $\sim 55 \mu\text{S}$ in isopropanol followed by the 13-mode ($\sim 41 \mu\text{S}$) and 23-mode ($\sim 21.2 \mu\text{S}$) were obtained. In Figure 8.6 the correlation between the piezoelectric response $\Delta G/Q$ and χ is depicted, indicating a fluid independent behavior, as described in Ref. [37]. The highest value for the $\Delta G/Q$ ratio is obtained for the 2nd order mode in isopropanol for the 03-mode ($0.774 \mu\text{S}$) followed by the 13-mode ($0.623 \mu\text{S}$) and the 23-mode ($0.316 \mu\text{S}$). The $\Delta G/Q$ values for 1st order modes are significantly lower compared to the 2nd order modes, but with the same sequence of 02-mode followed by 12- and 22-mode. These results are in good agreement with the simulated FEM analysis results, presented in Figures 8.2 and 8.3, where the 02/03-mode features strained areas along the entire surface. The presented $\Delta G/Q$ ratio, depicted in Figure 8.6, shows a constant behavior over a wide region from ~ 0.3 to $\sim 0.8 (\text{mPa}\cdot\text{s}\cdot\text{kg}/1)^{-0.5}$. This finding might be also applicable for high viscous liquids such as N100 or D500, but due to the low conductance peak ΔG and the resulting poor fitting procedure, high deviations in the determined quality factors and the resulting $\Delta G/Q$ values are obtained, which is discussed in detail in Chapter 7.

8.4 Conclusions

In this chapter micromachined piezoelectric resonators, equal in the physical dimensions, but with different support boundary conditions (i.e. single-side clamped, double-side clamped and quasi free-free-clamped), were presented. The resonators were actuated in an advanced roof tiled-shape mode of the 1st and 2nd order. The tailored electrode patterning, presented in Chapter 7 was implemented to enable an optimized collection of all piezoelectric charges without any compensation effect. finite element method analysis of the different clamping conditions were performed, showing strained areas along the entire surface for resonators with quasi free-free clamped boundary conditions, where the resonating plate is only supported at the nodal lines of the respective mode

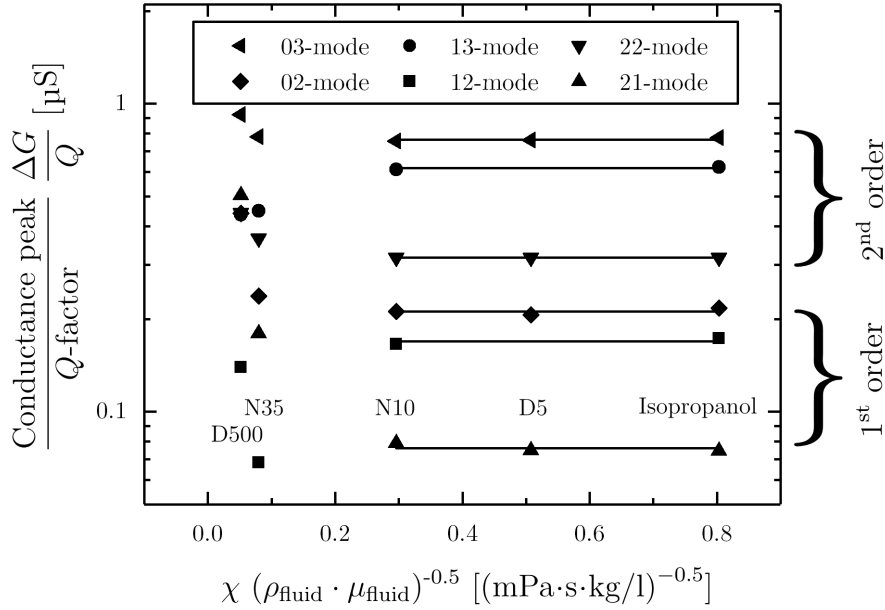


Figure 8.6: Piezoelectric response $\Delta G/Q$ over the inverse viscosity-density square root product in different liquids (isopropanol, and viscosity standards D5, N10, N100, D500).

shape. The fabricated resonators were characterized optically and electrically in air and in several liquids (isopropanol, D5, N10, N35, N100 and D500). Using optical and electrical characterization techniques, it could be pointed out that highly deflected surface areas do not likewise lead to increased values in the electrical response. Furthermore, it could be shown, that the different clamping conditions have insignificant influence on the overall quality factor in liquid media. However, the different clamping conditions affect the mode shape and the corresponding strain distribution on the plate surface, leading to significant differences in the electrical conductance peaks ΔG and the piezoelectric response $\Delta G/Q$ with the highest values for resonators with quasi free-free plate supports. Using this approach, the performance of piezoelectrically actuated plate-type resonators in terms of ΔG and $\Delta G/Q$ could be improved by $\sim 20\%$ for the quasi free-free supported resonator, compared to a resonator with clamped-free support. Due to these promising results, resonators with quasi free-free plate supports up to the 4th order mode have been fabricated and are investigated in detail in the following chapter.

Chapter 9

Performance of quasi free-free supported resonators in liquids

Parts of this chapter have already been published in Refs. [117]

In the previous two chapters it is emphasized, that the performance of piezoelectrically excited MEMS resonators in liquid environment can be improved by the consideration of high order modes and by the implementation of a quasi free-free mechanical support of the resonating structure. These very promising approaches can be merged into one resonator architecture with beneficial properties, which is presented in the following chapter. For this purpose, micromachined plate-type resonators have been fabricated for the first 4 orders of the so-called roof tile-shaped mode, featuring tailored mechanical support and electrode patterning for each mode order. The fabricated resonators are characterized electrically and optically in air and in several liquids. Modal analysis are compared to both laser Doppler vibrometer (LDV) measurements and finite element method (FEM) simulations, demonstrating an excellent agreement between the positions of the plate supports with those of the nodal lines of the specific mode, which ensures a quasi free-free vibration. The optimized electrode design (OED) from Chapter 7 is implemented and compared to non-optimized actuation, showing superior performance for plates with OED. The evaluation of the quality factor Q and the strain related conductance peak ΔG of the investigated modes results in the highest value for the 4th order mode ($Q \sim 100$; $\Delta G = 0.35 \text{ mS}$). Finally, the piezoelectric response $\Delta G/Q$ (highest value: $\sim 0.35 \text{ }\mu\text{S}$ for the 4th order mode) is presented, showing potential for a large variety of challenging resonator based physical and chemical sensing ap-

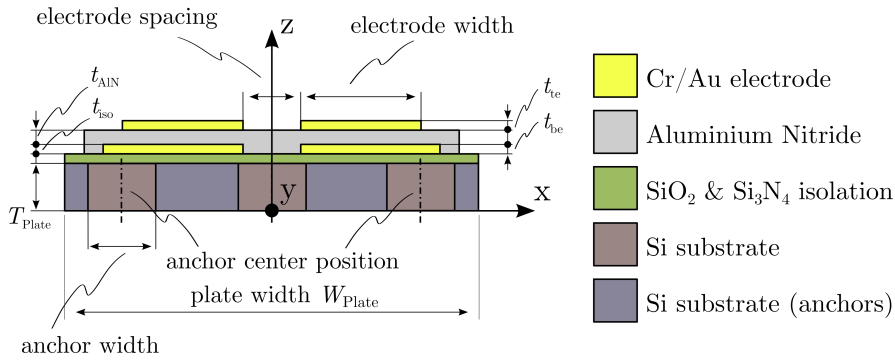


Figure 9.1: Schematic cross-sectional view of the MEMS resonator illustrating the electrode design and the plate support of the 03-mode.

plications.

9.1 Design considerations

The piezoelectrically excited and resonantly operating plates have been manufactured under the fabrication guidelines presented in Chapter 5. Thereby, the plate structures are fabricated on a 4 inch silicon-on-insulator wafer with a 20 μm thick silicon device layer, passivated with a $t_{\text{iso}} = 250/80 \mu\text{m}$ thick SiO₂/Si₃N₄ thin film as depicted in a schematic cross-sectional view in Figure 9.1. For actuating and sensing, an aluminium nitride (AlN) thin film with a thickness of $t_{\text{AlN}} = 1 \mu\text{m}$ is sputter deposited onto the plate and is sandwiched between two separated $t_{\text{be}} = t_{\text{te}} = 50/450 \text{ nm}$ thin chromium/gold thin films as illustrated in Figure 9.1. In this context, such a stack of Cr/Au | AlN | Cr/Au is labeled as "electrode" as already discussed in Chapter 7. In Figure 9.2 an optical micrograph of a typical die layout (6 x 6 mm²) packaged in a 24-pin DIP (dual in line package), including two particular clamped plates with the same geometrical dimensions and two electrodes is depicted. A pipette is used to completely immerse the packaged resonators in isopropanol and several viscosity standards (i.e. isopropanol, D5, N10, S20, N35, N100 and D500) from *Paragon Scientific*[®]. The physical properties such as density and viscosity of the individual liquids are listed in the Appendix A.1. Due to the low electrical conductivity of the investigated fluids, a passivation of the resonator surface is not required. However, air bubbles can accumulate below the quasi free-free supported plates,

Table 9.1: MEMS resonator designs: Geometrical dimensions for the 02-, 03-, 04- and 05-mode.

Description	02-mode	03-mode	04-mode	05-mode
Plate width / length / thickness		1274 / 2524 / 20 μm		
# of anchors per side	2	3	4	5
Anchor length / width / thickness		200 / 50 / 20 μm		
Anchor center position [μm]	-351 351 -	-468.5 0 468.5	-516.5 -183.5 183.5	543.5 -284 0
	-	-	516.5	284
	-	-	-	543.5
# of electrodes	2	2	3	4
Electrode width [μm]	617 617 -	617 617 -	437 350 437	335 272 272 335
Electrode length			2494 μm	
Electrode spacing			10 μm	
Actuation: OED (no OED)	-- (n.a.)	+- (n.a.)	+- (n.a.)	+- (n.a.)
			--- (---)	---- (++++)

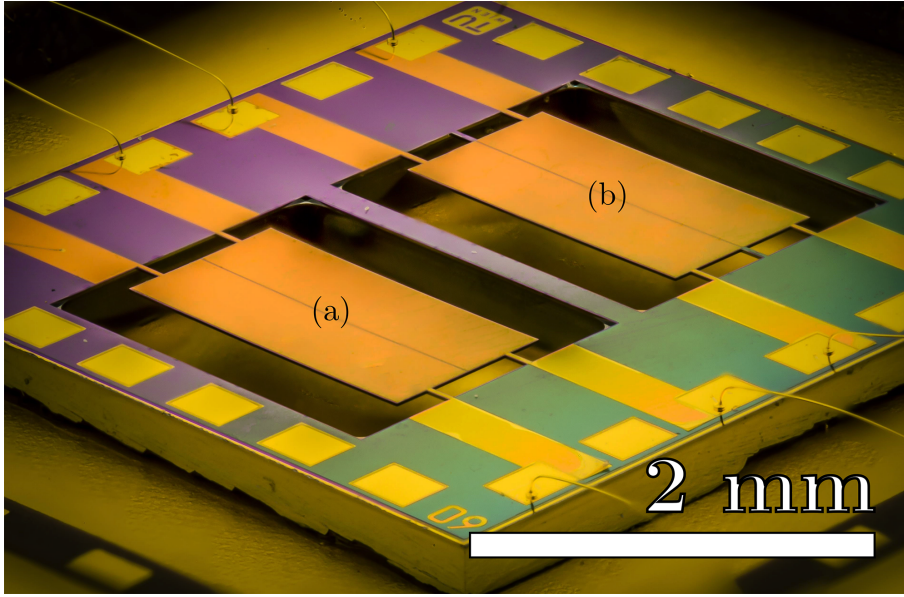


Figure 9.2: Optical micrograph of piezoelectrically excited and resonantly operating plate-type resonators with quasi free-free plate support optimized for (a) the first and (b) the second order of the 0X-modes.

Table 9.2: Performance of the higher order roof tile-shaped modes in isopropanol with and without OED excitation.

Mode	f_{res} [kHz]		Q [1]		ΔG [μS]		$\Delta G/Q$ [μS]	
	no OED	OED	no OED	OED	no OED	OED	no OED	OED
1 th	-	55.72	-	33	-	10.4	-	0.31
2 nd	-	166.6	-	70	-	54.8	-	0.77
3 rd	342.9	343.1	83	82	33.2	180	0.4	2.2
4 th	599.4	599.9	99	101	4.92	379	0.049	3.8

which may lead to a misinterpretation of the measurement results. On the other hand, the hydrophilic wetting behavior of the investigated viscosity standards with respect to the resonator surface and the bottom of the DIP reduces the occurrence of such effects. To further reduce the potential impacts of air bubbles to a minimum, every single measurement is performed twice. After each characterization step the entire package is cleaned with isopropanol and dried for 20 min at 20°C. To guarantee comparable results, all further measurements were performed in a temperature-controlled environment at 20°C \pm 0.5°C. Furthermore, device-related key parameters (i.e. quality factor and resonance frequency) are determined in air between two measurements in liq-

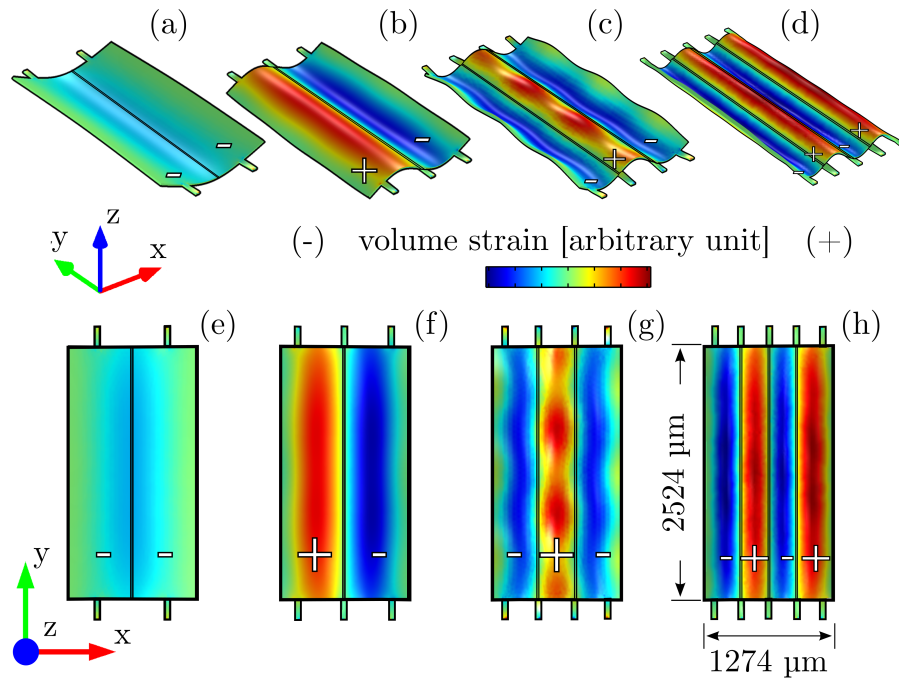


Figure 9.3: Visualization of the 1st (02-mode), 2nd (03-mode), 3rd (04-mode) and 4th (05-mode) order of the roof tile-shaped mode (a-d) and the corresponding top views (e-h). The colored areas on the plate surface represent the local surface strain distribution with tensile strain (red) and compressive strain (blue), respectively. The positive (+) and the negative (-) sign indicate, in combination with the black rectangles, the optimized electrode design and the polarity of each electrode stripe.

uids to detect and subsequently remove any possible contamination arising from any incomplete cleaning procedure in isopropanol.

9.2 Mode shape analysis

finite element method (FEM) analysis of the first four orders were performed utilizing the commercial FEM tool COMSOL Multiphysics and its results are illustrated in Figure 9.3. The elementary eigenfrequencies are determined for the first four orders of the roof tiled-shaped mode. The number of nodal lines along the x-axis increases with increasing mode order. By counting the number of nodal lines in y- and x-direction, this advanced roof tile-shaped mode is labeled in the following as 0X-mode, where $X = 2, 3, 4$ or 5 indicates the number of nodal lines along the x-axis. The particularly clamped plate support, already mentioned in Chapter 8, enables a quasi-free vibration and strained

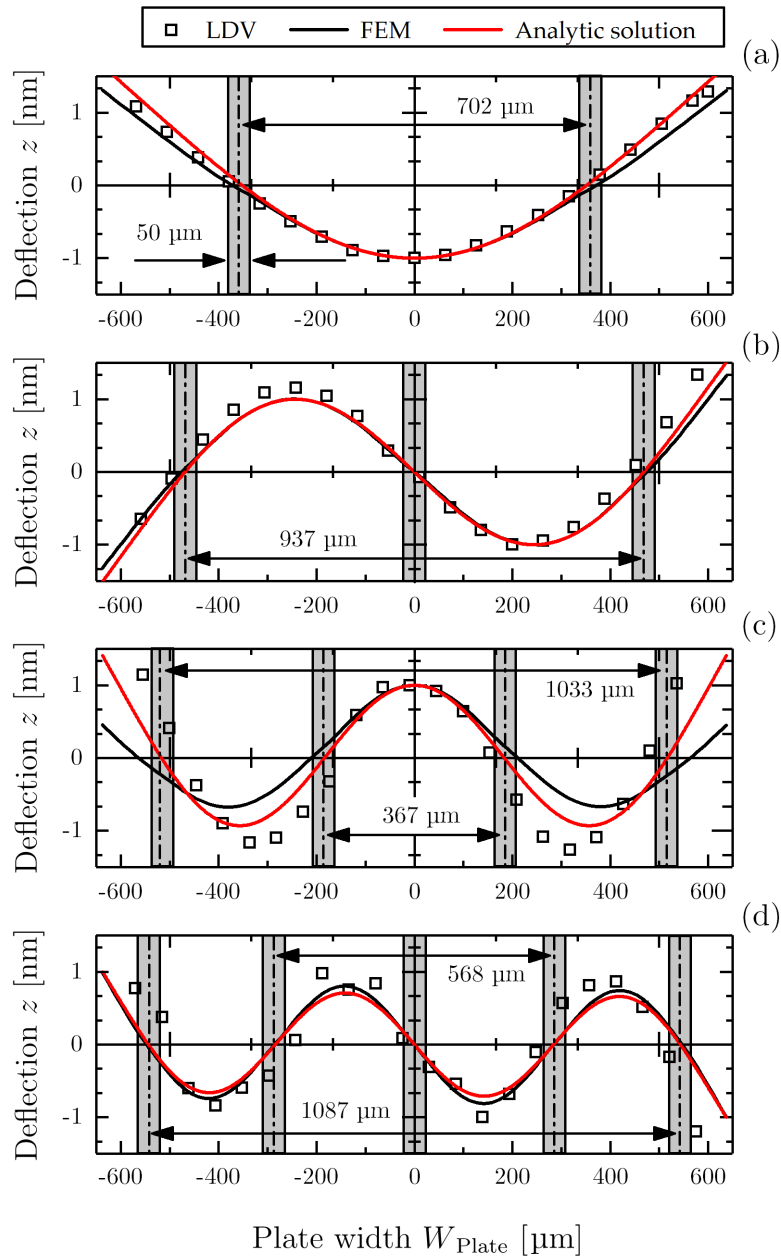


Figure 9.4: Nodal analysis of the support boundary conditions for (a) the 02-mode, (b) the 03-mode, (c) the 04-mode and (d) the 05-mode in air, including results from analytical calculations, FEM simulations, LDV measurements and the illustration of the plate-supports indicated by cyan colored areas.

areas along the entire y -axis are guaranteed. Furthermore, the implemented optimized electrode design OED from Chapter 7 is depicted by black rectangles around surface areas with surface strains of the same sign (+/-). This approach maximizes the collection of piezoelectrically generated charges of the same sign (+/-) without compensation, as published recently [109, 114] and already described in Chapter 7. In addition, the Euler–Bernoulli beam theory is applied to calculate the position of the nodal lines in vacuum as described in Chapter 2, which are considered as estimated positions of the nodal lines in liquids and are listed for all investigated modes in Table 9.1. As it can be seen in Figure 9.3, the investigated mode orders require different sized and actuated electrodes for optimal actuation. Furthermore, the amount of electrodes has to be adapted, resulting in two electrodes for the 02- and 03-mode, three electrodes for the 04-mode and four electrodes for the 05-mode. To illustrate the importance of the optimal actuation (OED), the 04- and 05-mode are additionally actuated in not ideal configurations. Thereby, the three collaterally arranged electrodes of the 04-mode are excited in-parallel (---) and the four electrodes of the 05-mode in anti-parallel (+ +--) configuration, as listed in Table 9.1. Additionally it is worth to mention, that the non-ideal actuations of the 03-mode (--) and 05-mode (----) lead to a serious charge compensation so that no measurable frequency response is detectable. Analytical nodal line analyses were performed and compared to FEM simulations and LDV measurements in air. The corresponding results are illustrated in Figure 9.4, including the 02-mode in (a), the 03-mode in (b), the 04-mode in (c) and the 05-mode in (d). The bending profile from FEM analyses and LDV measurements were evaluated close to one of the supported edges of the plate in y -direction (see Figure 9.3), showing a good match of the positions of the nodal lines with the plate supports (gray areas). Furthermore, an adequate match with the analytically calculated nodal lines is achieved for the 02-, 03- and 05-mode. However, minor deviations between the theoretical predictions and the experimental results occur for the 04-mode (see Figure 9.3 (c) and (g)), caused by its irregular curvature characteristics, which can be seen in Figure 9.4 (c).

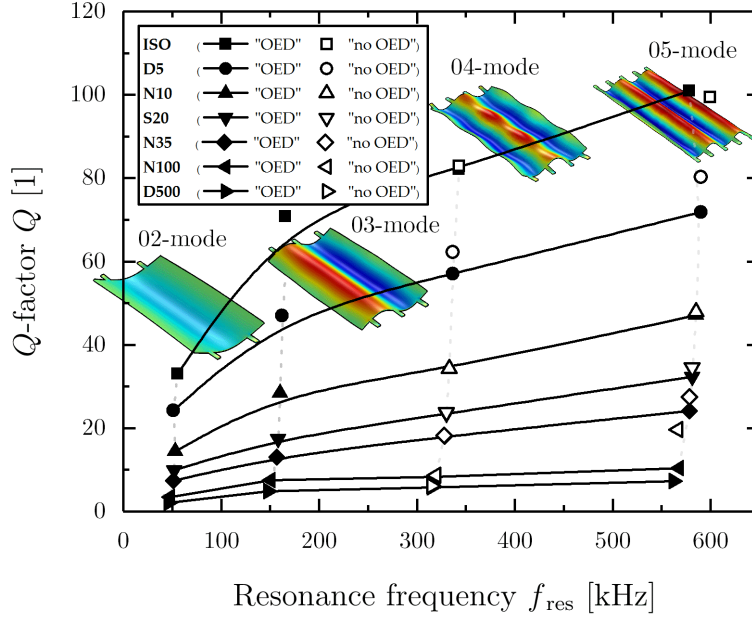


Figure 9.5: Quality factors of the 0X-modes with and without OED in different liquids.

9.3 Electrical characterization in liquid media

The electrical performance is evaluated by measuring the resonance frequency f_{res} , the quality factor Q and the conductance peak ΔG as described in Chapter 6. In Figure 9.5 the results of the Q -factor evaluation for all investigated modes with and without OED in isopropanol, D5, N10, S20, N35, N100 and D500, showing the reported square-root-like behavior when plotted over the resonance frequency, even when excited at higher order modes [23, 39]. Thereby, the Q -factor decreases for liquids with increasing viscosity and density values. The highest Q -factor ($Q \sim 100$) is achieved for the 05-mode at ~ 600 kHz in isopropanol and is in agreement with the results for a single-side clamped beam reported in [39]. A significant influence of the OED on the Q -factor could not be observed, which is in excellent accordance with literature [118]. In Figure 9.6 the electrical conductance peak ΔG is plotted over the resonance frequency f_{res} , showing significantly enhanced conductance peak heights ΔG when using OED, which confirms the theoretical pre-considerations. The highest value of $379 \mu\text{S}$ is obtained for the 05-mode in isopropanol. The importance of an OED becomes clear, as devices with OED exhibit up to 77 times higher conductance

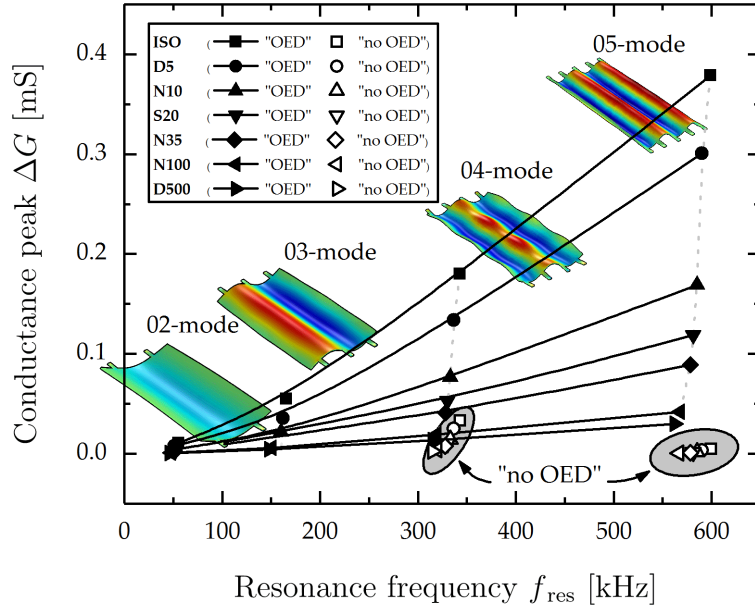


Figure 9.6: Electrical characterization of the 0X-modes with and without OED in different liquids represented by the conductance peak ΔG as a function of the resonance frequency.

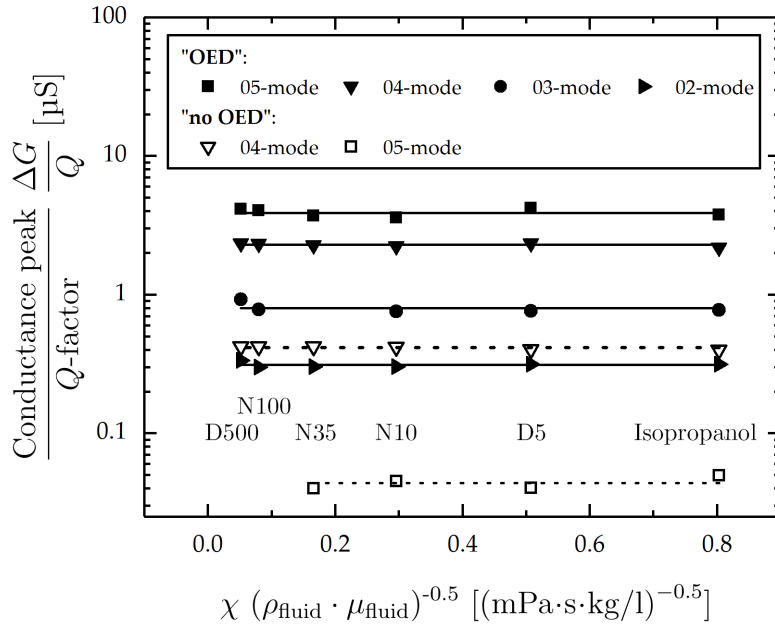


Figure 9.7: piezoelectric response $\Delta G/Q$ as a function of the inverse square root viscosity/density product with and without OED in different liquids.

peaks ΔG (05-mode) compared to those without OED (highlighted in gray in Figure 9.6). This also results in enhanced values for the piezoelectric response $\Delta G/Q$, plotted over the inverse square root viscosity/density product χ in Figure 9.7. Furthermore, a constant behavior over a wide range from $\chi \sim 0.05$ to $\chi \sim 0.8 (\text{mPa}\cdot\text{s}\cdot\text{kg}/\text{l})^{-0.5}$ is obtained, including the highest averaged value for the 05-mode ($\overline{\Delta G/Q}_{05} = 3.90 \mu\text{S}$). The constant behavior of $\Delta G/Q$ for all investigated liquids is in perfect agreement with the theoretical findings presented in Ref. [37]. A summary of electrical measurement results with and without OED obtained in isopropanol are presented in Table 9.2.

9.4 Conclusions

Micromachined piezoelectric resonators were fabricated and roof tiled-shape modes were excited up to the 4th order. The support boundary conditions of the resonators were optimized in such a way that their positions fit to those of the nodal lines of the targeted mode. This ensures a quasi free-free vibration, an extended surface strain and an increased strain related conductance peak ΔG , leading to an increased piezoelectric response $\Delta G/Q$ by $\sim 20\%$ with respect to the same device in a standard cantilever configuration. Furthermore, an optimized electrode design was used to collect most of the generated piezoelectric charges without any compensation effect. Modal analyses performed using FEM simulations, laser Doppler Vibrometry measurements as well as analytical beam theory analysis show a good match of the calculated location of the physical plate supports and the optically measured nodal lines. Quality factor evaluation was performed showing no significant impact on the optimized support design on the quality factors in liquids. Finally the conductance peak ΔG and the piezoelectric response $\Delta G/Q$ were evaluated in several liquids (isopropanol and viscosity standards: D5, N10, N35, N100, D500) and the highest piezoelectric response ($\sim 4 \mu\text{S}$) was measured in isopropanol. With the presented optimization of the support design, the electrical performance has significantly increased compared to single side clamped resonators with the same geometry and quality factor, showing great potential for a large variety of challenging physical and chemical resonator-based sensing applications.

Chapter 10

Wine fermentation monitoring

This chapter has already been published in Refs. [1, 119]

In the last chapter of this thesis a potential application for the investigated sensing concept is introduced. Thereby piezoelectric resonators are excited in advanced roof tile-shaped vibration modes and are used to monitor the fermentation process during wine making. The micro fabricated sensor features very high quality factors in liquid media ($Q \sim 100$ in isopropanol), which ensures precise monitoring of the density evolution associated with the decrease in sugar and the increase in ethanol concentrations during wine fermentation processes. To demonstrate the potential of piezoelectric MEMS resonators two sets of artificial model solutions are prepared, representing an ordinary and a stuck/sluggish wine fermentation process.

10.1 Introduction

The fermentation of grape must into wine involves the interaction between yeasts, bacteria, fungi, and viruses. This complex biochemical process has been recognized and studied since the pioneering investigations of Louis Pasteur in the 1860s. During such a fermentation process, yeasts utilize sugars and other constituents of the grape must for their growth, converting these to alcohol (ethanol), carbon dioxide, and other metabolic end products [120]. A serious problem in winemaking occurs when the yeast growth and the alcoholic fermentation stops prematurely, which results in a wine with residual, unfermented sugar and a concentration of ethanol less than expected. This is indicated in minor, but measurable deviations of the targeted physical properties, such as

density and viscosity, when compared to an ordinary fermentation, and the wine is commonly referred to as being stuck, or sluggish [121, 122]. There are several approaches to monitor such a fermentation of wine according to different parameters related to the process. El Haloui *et al.* [123], Nerantzis *et al.* [124], and Koukolitschek [125] reported on density determination based on differential pressure measurements or flexural oscillators, respectively. By monitoring the CO₂ release, the fermentation process can also be monitored, as reported in Ref. [123]. Another approach is to determine the yeast cell population evolution by means of impedance [126] or turbidity measurements [127]. The propagation velocity in grape must, determined by ultrasound measurements, can also be used for monitoring the fermentation process [128, 129]. Lastly, a reflective technique based on fiber optics was reported in Refs. [130, 131]. Basically, all of these different approaches have their specific drawbacks; some lack the requested accuracy, others have only been tested in discrete must samples and, in some cases, the sensor output performance deteriorates dramatically due to an increasing deposition of tartaric acid crystals on the active surface of the sensors [131].

In recent years, cantilever-like MEMS resonators have become a reliable platform for various sensing applications [132]. As already discussed in Chapter 1, "so-called "fluidic channel resonators", in which the fluid passes through a fluidic channel in the moving part of the resonator are intensely studied. A disadvantage of fluidic channel resonators is their low reusability, which is caused by potential clogging of the fluidic channel. Therefore, such resonators are often designed as one-time use devices, which increases the cost of the overall system. In contrast, solid resonators are often easier to clean, which increases reusability, but generally lacks in precision compared to fluidic channel resonators. The recent improvements in the field of piezoelectric solid MEMS resonators for liquid monitoring purposes predestines such a system for sensing applications, where decent accuracy is required [38, 39, 116]. The piezoelectric actuation and readout mechanism keeps the sensor device reasonably compact and does not require any further laser-based measurement equipment. In this particular field, the question arises whether a micro-machined solid resonator is capable to detect the minor deviations in the physical properties of the grape must during the fermentation process, and hence, whether it offers a promising alternative to the presented measurement approaches. Most recently, Toledo

et al. [133] introduced a phase locked loop-based oscillator circuit in combination with a commercial lock-in amplifier to track the oscillation frequency of the solid resonators. Using this measurement setup, in combination with an evaluation procedure presented in [134], it was shown that the monitoring of grape must fermentation using solid MEMS resonators is, in principal, possible [135]. In this chapter we will focus on the reliability and the re-usability of such a solid resonator and what impact potential contaminants have on the sensor characteristics despite the harsh liquid environment. Based on these investigations, an estimation of the precision of the sensor concept, evaluated by reproducibility measurements is given. Furthermore, different measurement and evaluation procedures are used to validate the data presented in [135]. Finally, test measurements in a real grape must are presented and compared to those of the artificial solutions, thus proving the suitability of the presented concept for grape must fermentation monitoring.

10.2 Experimental details

Sensor specifications

The piezoelectric resonators are manufactured under the fabrication guidelines presented in Chapter 5 and feature a length of $L_{\text{plate}} = 2524 \mu\text{m}$, a width of $W_{\text{plate}} = 1274 \mu\text{m}$ and a thickness of $T_{\text{plate}} = 20 \mu\text{m}$, and are passivated with a $t_{\text{iso}} = 250/80 \text{ nm}$ thick $\text{SiO}_2/\text{Si}_3\text{N}_4$ thin film. For actuating and sensing, an aluminium nitride (AlN) thin film with a thickness of $t_{\text{AlN}} = 1 \mu\text{m}$ is sputter deposited onto the plate surface and is sandwiched between two separated chromium/gold thin film electrodes with equal thickness for bottom and top electrode $t_{\text{be}} = t_{\text{te}} = 50/450 \text{ nm}$. In Figure 10.1, the used sensor chip after packaging and wire bonding with a released single-side clamped resonator, and its top view as an inset, is shown. The corresponding mode shape is illustrated by finite-element method (FEM) eigenmode analyses for the 4th-order (15-mode) of the roof tile-shaped mode in side view in Figure 10.2 (a) and in top view in Figure 10.2 (b). In Figure 10.3 a schematic cross-sectional view is presented, showing the electrode design optimized for the 4th-order of the roof tile-shaped mode and four electrodes ($w_o = 335 \mu\text{m}$, $w_i = 272 \mu\text{m}$) with alternating anti-parallel electric excitation to ensure in addition a collection of almost all generated polarization charges without cancellation as presented in Chapter 7. The result

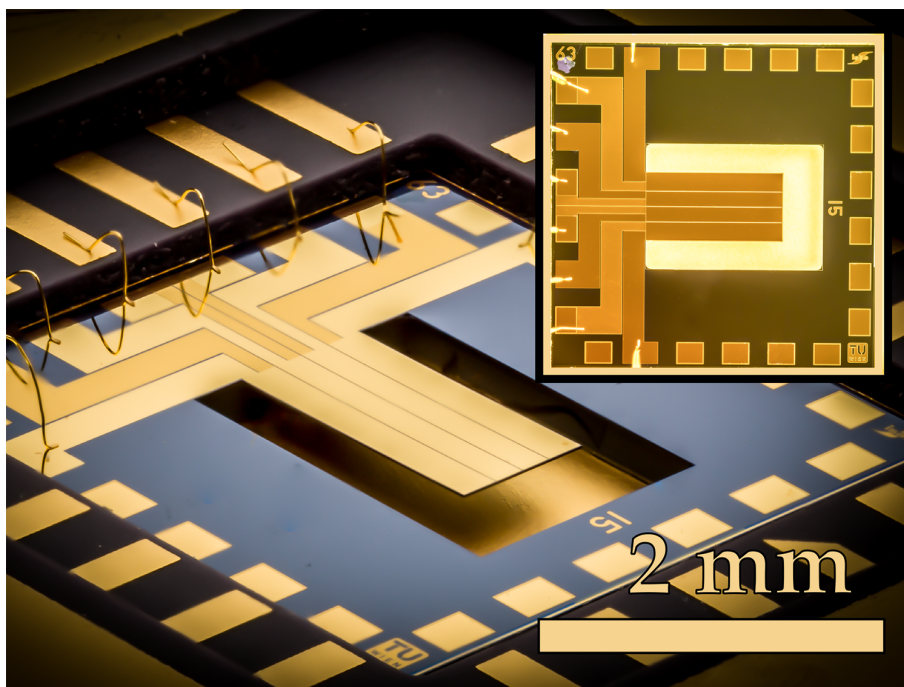


Figure 10.1: Optical micrograph of the in-house fabricated silicon die ($6 \times 6 \text{ mm}^2$), containing one piezoelectric actuated plate (dimensions: $2524 \times 1274 \times 20 \mu\text{m}^3$) using advanced electrode patterning considering the volume-strain of the modal shape presented in Figure 10.2.

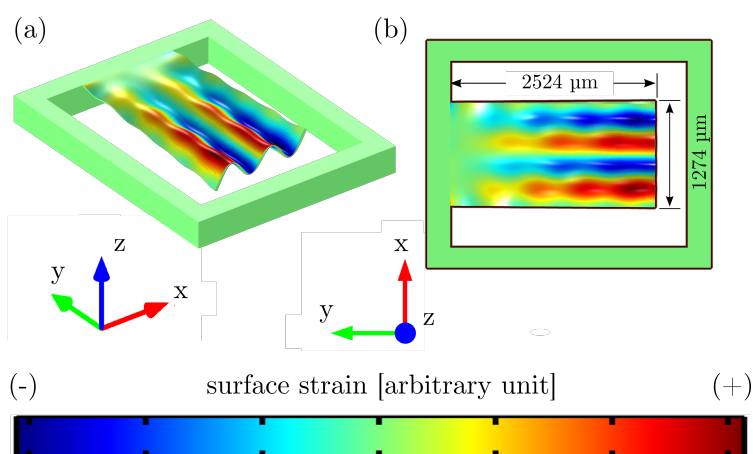


Figure 10.2: Visualization of the side view in (a) and the top view in (b) for a plate excited in the 4th order of the roof tile-shaped mode (15-mode). The colored areas on the cantilever surface represent the local volume strain distribution.

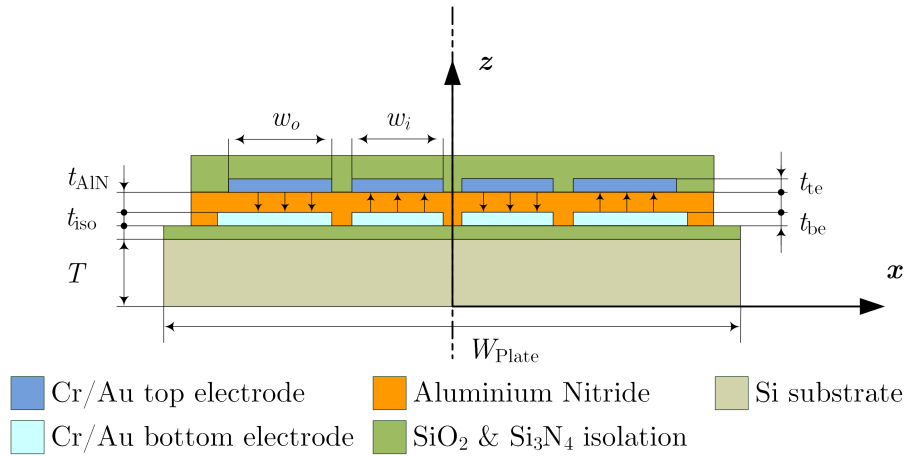


Figure 10.3: Schematic cross-sectional view on the MEMS resonator illustrating the electrode design of the 15-mode.

Table 10.1: Characterization of the resonator in air. $R_{m,\text{air}}$, $L_{m,\text{air}}$, and $C_{m,\text{air}}$ represent the unperturbed resonator in air.

f_{res}	Q	R_m	L_m	C_m
1014.1 kHz	329.6	1.365 k Ω	70.662 mH	348.77 fF

of this tailored electrode design is an increased deflection in z -direction and, in further consequence, both an increased strain related conductance peak [109] and an increased signal to noise ratio as shown in Chapter 7. Furthermore, it is worth mentioning that the resonance frequencies in liquids do not exceed 600 kHz, which simplifies the electrical measurement procedure and minimized any pressure-induced energy losses by sound waves, which requests compressive fluid properties as discussed in Chapter 4 and 7. Secondly, high quality factors above 100 are achieved with this type of mode, which facilitates a high sensitivity of resonance frequency as evaluated in Chapter 7.

Artificially aged model solutions and sensing principle

Two sets of model solutions are prepared, using a R200D microscale from Sartorius, representing an ordinary (N_{1-9}) and a stuck/sluggish (S_{1-9}) wine fermentation process, consisting of fructose, glucose, glycerol, and ethanol [136]. The specific compositions are listed in Tables 10.2 and 10.3 and show significant differences in the fructose, glucose, and ethanol concentrations, when compar-

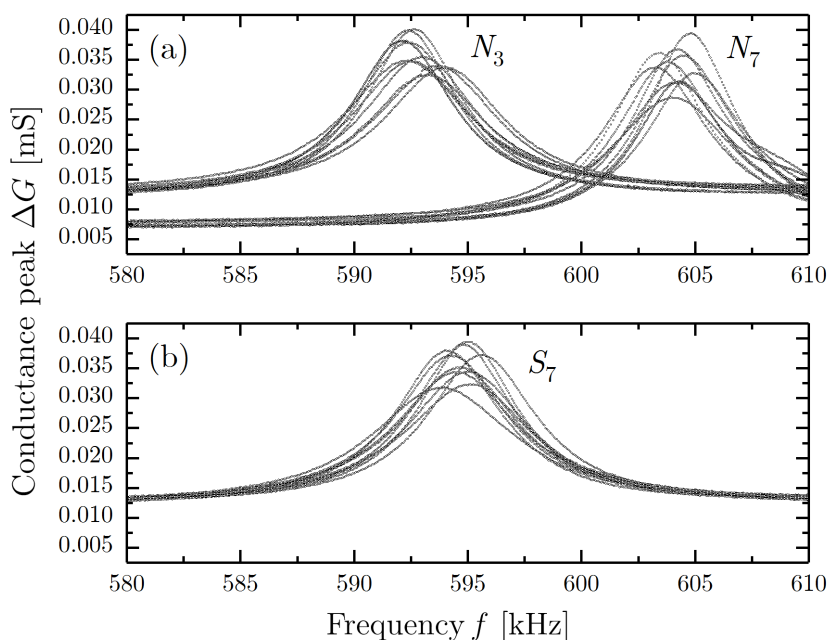


Figure 10.4: Reproducibility measurement of two model solutions of an ordinary fermented grape must (N_3 and N_7) in (a), and of a stuck fermented grape must (S_7) in (b) at 22°C.

ing ordinary and stuck/sluggish wine fermentation processes. The conductivity of both sets are obtained using a WTW LF 323-A conductivity meter and are listed in the Appendix in Table A.9. The resonator is immersed in these model solutions and actuated in the 4th order of the roof tile-shaped mode with an Agilent 4294A impedance analyzer (excitation voltage $V_{\text{exc}} = 500$ mV AC). The excitation in resonance leads to an increased average deflection and to enhanced mechanical strain on the sensor surface, respectively. Due to the piezoelectric effect, polarization charges are generated, which are detected by the impedance analyzer as an increased conductance peak ΔG as already described in Chapter 6. Subsequently, the sensor is cleaned with dish soap and isopropanol, followed by a 20 min drying process at room temperature to avoid tartaric acid crystal deposition, which is reported in [131]. From the frequency response, the resonance frequency f_{res} and quality factor Q are determined using the Butterworth-van Dyke equivalent circuit, in combination with Levenberg-Marquardt algorithm [118] as described in Chapter 6. Once f_{res} and Q are obtained for all solutions (N_{1-9} and S_{1-9}), an evaluation procedure taken from [105]

Table 10.2: Chemical composition of model solutions representing a desired wine fermentation process from N_1 (raw grape must) up to N_9 (ordinary fermented model solution) [17]. The measured values are obtained using a R200D microscale from Sartorius.

Sol.	Fructose		Glucose		Glycerol		Ethanol	
	[g/l]		[g/l]		[g/l]		[% v/v]	
-	nom.	meas.	nom.	meas.	nom.	meas.	nom.	meas.
N_1	110	109.90	100	99.90	0	0	0	-
N_2	90	89.90	80	80.00	0	0	1	-
N_3	70	69.95	30	30.03	5	4.99	6	-
N_4	60	59.97	20	19.99	5	5.00	8	-
N_5	40	39.90	10	9.95	6	5.99	9	-
N_6	20	19.90	2	2.00	7	6.97	12	-
N_7	8	8.02	2	2.00	7	6.99	13	-
N_8	5	5.00	2	2.00	7	6.99	13	-
N_9	2	2.00	1	0.99	9	8.99	14	-

is used to determine the actual density ρ_{fluid} using

$$\rho_{\text{fluid}} = \frac{\text{Im}(Z_m) - \omega_{\text{res}}L_m + \frac{1}{\omega_{\text{res}}C_m} - \text{Im}(Z_m) + R_m}{\omega_{\text{res}}d_1}. \quad (10.1)$$

Here, Z_m describes the impedance of the equivalent resonance circuit including a resistance R_m , an inductance L_m and a capacity C_m at a certain angular frequency ω_{res} in liquid. The constant parameter parameter (d_1) is determined in a calibration liquid with known viscosity and density, using

$$d_1 = \frac{\text{Im}(Z_m) - \omega_{\text{res}}L_{m,\text{air}} + \frac{1}{\omega_{\text{res}}C_{m,\text{air}}} - d_2\sqrt{\rho_{\text{fluid}}\mu_{\text{fluid}}\omega_{\text{res}}}}{\omega_{\text{res}}\rho_{\text{fluid}}} \quad (10.2)$$

with

$$d_2 = \frac{\text{Re}(Z_m) - R_{m,\text{air}}}{\sqrt{\mu_{\text{fluid}}\rho_{\text{fluid}}\omega_{\text{res}}}}, \quad (10.3)$$

where $R_{m,\text{air}}$, $L_{m,\text{air}}$, and $C_{m,\text{air}}$ are the corresponding unperturbed resonator values in air and are given in Table 10.1. For this initial calibration process values supplied by the manufacturer for μ_{fluid} and ρ_{fluid} of N_4 and S_4 are used to calculate d_1 and d_2 , as shown in Equations 10.2 and 10.3. Once these two constants are obtained, all further values of ρ_{fluid} can be determined using Equation 10.1.

Table 10.3: Chemical composition of model solutions representing a stuck wine fermentation process from S_1 (raw grape must) up to S_9 (stuck fermented model solution) [17]. The measured values are obtained using a R200D microscale from Sartorius.

Sol.	Fructose		Glucose		Glycerol		Ethanol	
	[g/l]		[g/l]		[g/l]		[% v/v]	
-	nom.	meas.	nom.	meas.	nom.	meas.	nom.	meas.
S_1	110	109.90	100	99.98	0	0	0	-
S_2	90	90.00	80	79.98	0	0	1	-
S_3	80	79.98	60	60.01	3	3.00	3	-
S_4	70	69.98	30	29.98	5	4.99	6	-
S_5	66	65.99	27	27.03	5	4.99	7	-
S_6	64	64.00	26	26.06	5	5.01	7	-
S_7	62	61.99	24	24.00	6	5.99	7	-
S_8	58	57.99	22	22.00	6	5.99	7	-
S_9	57	56.99	21	21.00	7	7.01	8	-

Real grape must fermentation

For the investigation of a real fermentation process, *Airén*¹ grapes are processed into grape must with a subsequent filtering process to avoid damaging the sensor by large grape skin particles. After this procedure, the grape must is inoculated with 0.2 g/ml of *Saccharomyces cerevisiae* strain (UCLM S325, Fould-Springer, Ciudad Real, Spain) previously rehydrated, as described in the supplier guidelines. An *Applikon*[®] cylindrical fermenter is filled with 3l of inoculated must, where the temperature was controlled at 28°C. The fermentation monitoring is carried out by means of the extraction and analysis of 7 mL-samples approximately every 5 h during the following six days. After extraction, the samples were centrifuged for one minute at 1000 rpm in a Universal 32R from *Hettich*[®] and kept refrigerated at -20°C until analysis.

10.3 Results

In Figure 10.4, the results from the reproducibility measurements are depicted in Figure 10.4 (a) for N_3 and N_7 of an ordinary fermented grape must, and in Figure 10.4 (b) for S_7 of a stuck fermented grape must. The measurement

¹Spanish white grape variety

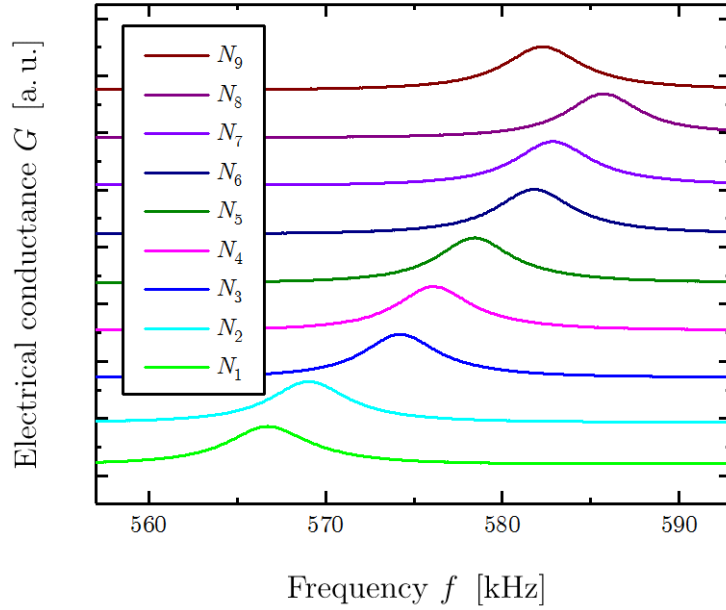


Figure 10.5: Electrical output characteristics of the piezoelectric MEMS resonator for an ordinary fermentation process N_{1-9} , starting with N_1 at the bottom and all other model solutions (N_2-N_9) stacked above. The y-axis is scaled as arbitrary unit [a.u.].

procedure, including the cleaning process presented in the previous part of this paper, is repeated 10 times. Thereby, standard deviations in the resonance frequency f_{res} of 0.102% for N_3 , 0.085% for S_7 and 0.094% for N_7 are obtained, thus showing a high potential for the targeted application. Higher standard deviations are obtained for the Q -factor ($\sim 11\%$) and the conductance peak ($\sim 12\%$), which, however, have minor impacts on the final calculation of the density values, indicated by a standard deviation of the calculated density values of 1.2% for N_3 , 1.1% for N_7 , and 1.0% for S_7 . The compositions of the artificial wine solutions for an ordinary (N_{1-9}) wine fermentation process, listed in Table 10.2, show a decrease in fructose and glucose concentration from 110 and 100 g/l (N_1) to 2 and 1 g/l (N_9), respectively. Likewise, the glycerol and ethanol concentration are increasing from zero to 9 g/l and 14% v/v. In the case of a stuck fermented wine process, as it is listed in Table 10.3, the fructose and glucose concentrations decrease to 50 and 20 g/l, respectively, and remain constant at these values. In parallel, the increase in the ethanol concentration stops as well, and does not exceed a value of 8% (v/v). These significant changes

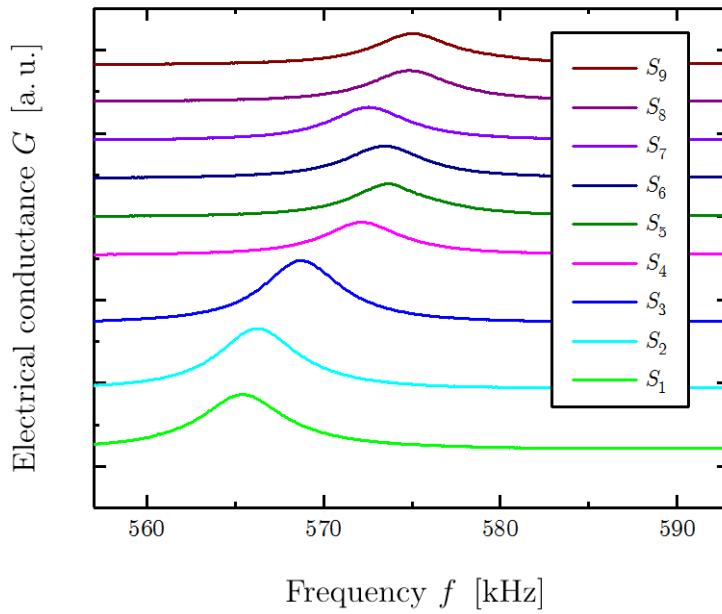


Figure 10.6: Electrical output characteristics of the piezoelectric MEMS resonator for a stuck fermentation process S_{1-9} , starting with S_1 at the bottom and all other model solutions (S_2 – S_9) stacked above. The y-axis is scaled as arbitrary unit [a.u.].

Table 10.4: Electrical parameters of ordinary(N_{1-9}) and stuck(S_{1-9}) model solutions evaluated with Agilent 4294A impedance analyzer.

Ordinary			Stuck/sluggish		
Sol.	f_{res} [kHz]	Q [1]	Sol.	f_{res} [kHz]	Q [1]
N_1	567	100	S_1	565	95
N_2	570	106	S_2	566	103
N_3	574	109	S_3	569	105
N_4	576	110	S_4	572	106
N_5	578	111	S_5	574	106
N_6	582	110	S_6	574	106
N_7	583	110	S_7	573	106
N_8	586	108	S_8	575	102
N_9	582	107	S_9	575	101

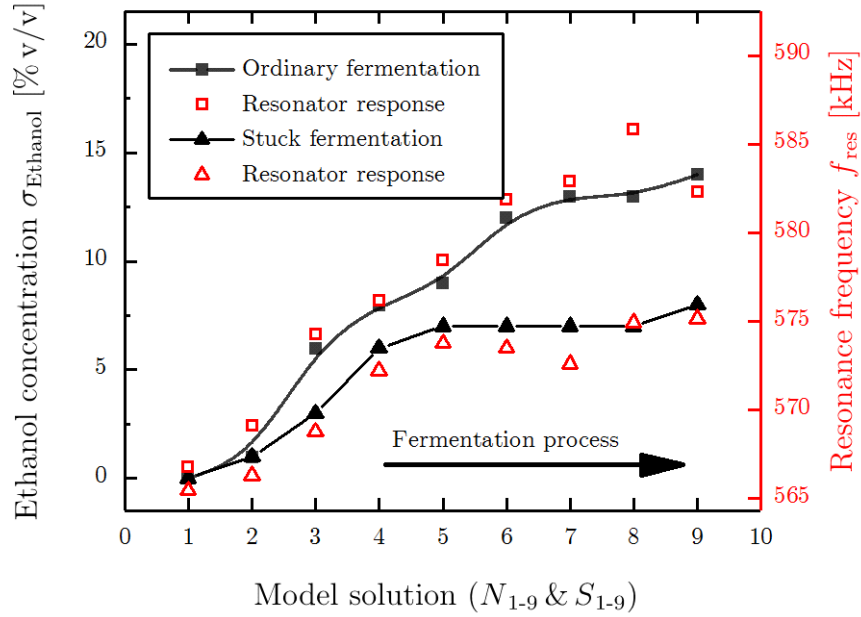


Figure 10.7: 15-mode frequency response analysis of an ordinary (N_{1-9}) and a stuck (S_{1-9}) fermentation process in comparison to the nominal ethanol concentration of the investigated model solutions. The inserted lines serve as guide to the eye.

in the composition of the model solutions affect the frequency response of the MEMS sensor as shown for both an ordinary fermentation in Figure 10.5 and a stuck fermentation in Figure 10.6. The corresponding values in Q are listed in Table 10.4. In the first case, the resonance frequency increases monotonically for the ordinary fermentation (see Figure 10.5). In contrast, the increase of the resonance frequency during the investigation of the stuck fermentation plateaus at ~ 575 kHz. In Figure 10.7, the results of the resonance response analysis are compared to the ethanol concentration σ_{Ethanol} for both sets of model solutions. Significant differences in the resonance frequencies f_{res} are evident with increased σ_{Ethanol} values when comparing ordinary and stuck fermentation, as well as a good correlation between σ_{Ethanol} and f_{res} . The combination of unfermented sugars and lower concentration of ethanol in a stuck fermentation (see Table 10.3) leads to a flat resonance characteristics, allowing to detect this unwanted status. The results from the repeatability measurements of N_3 , N_7 , and S_7 from Figure 10.4 are used to estimate the reproducibility of the MEMS sensor. For a further analysis of this particular progress a second resonator with

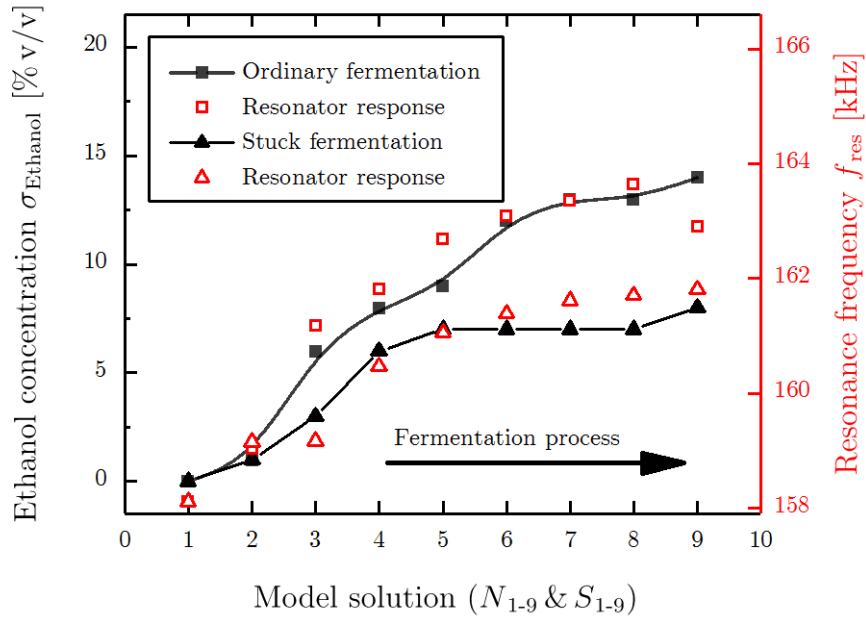


Figure 10.8: 12-mode frequency response analysis of an ordinary and a stuck fermentation process in comparison to the nominal ethanol concentration of the investigated model solutions. The inserted lines serve as guide to the eye.

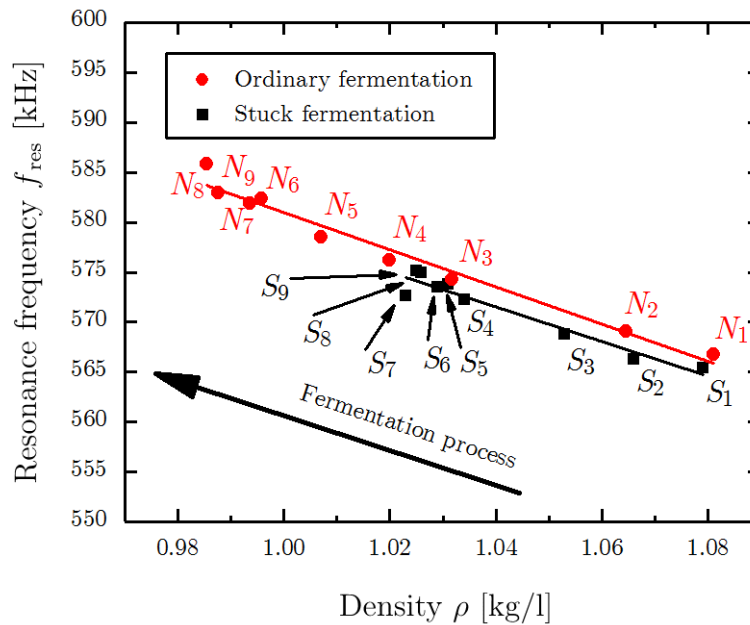


Figure 10.9: Correlation between the calculated density and the measured resonance frequency for an ordinary (red) and a stuck (black) fermentation process. The inserted lines serve as guide to the eye.

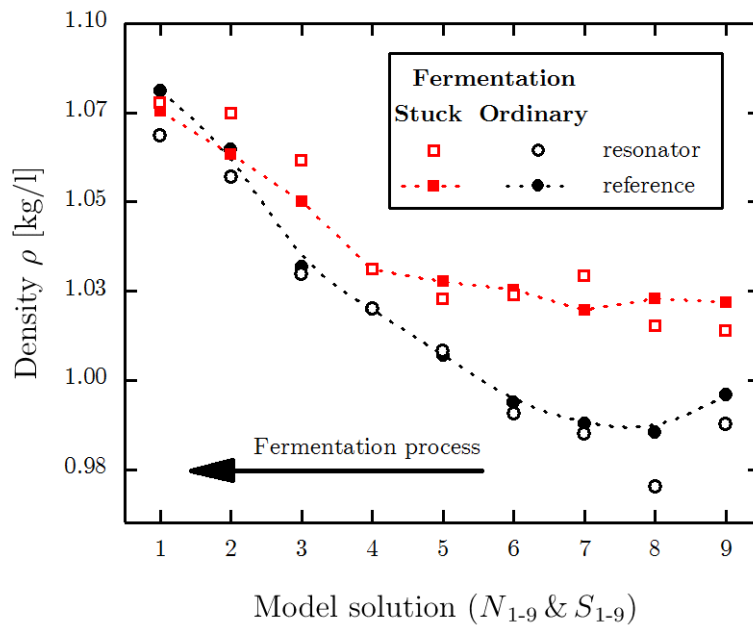


Figure 10.10: Density values for ordinary (N_{1-9}) and stuck (N_{1-9}) fermented model solutions evaluated with the presented resonator (unfilled dots) and its reference values obtained with a Stabinger viscometer SVM3000 (filled dots). The inserted dashed lines serve as guides to the eye.

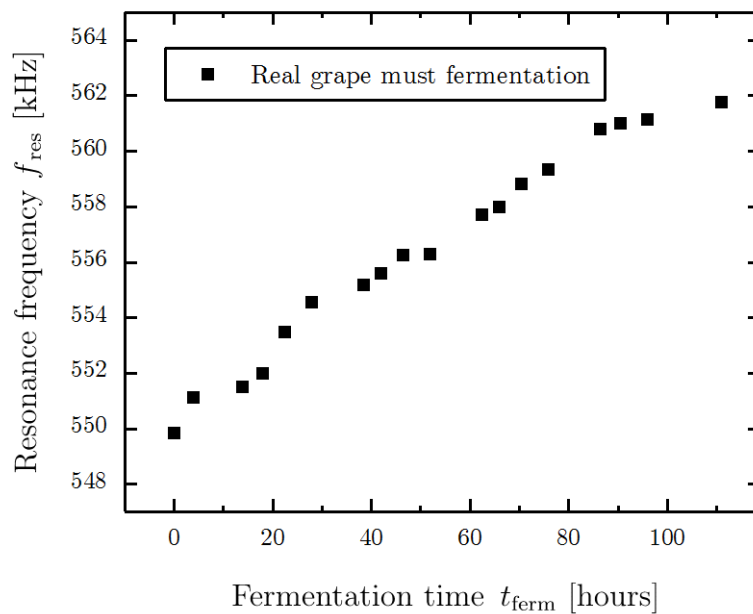


Figure 10.11: Frequency response of the 15-mode in a real grape over fermentation time t_{ferm} at 20°C.

the same geometry is excited in the first roof tile-shaped mode (12-mode). The resonance frequencies in both sets of model solutions amount around 1/4 of the resonance frequency of the 15-mode (~ 160 kHz) and are depicted in Figure 10.8, showing a similar characteristics in the frequency response. Compared to the results presented in Figure 10.6 the absolute change in resonance frequency is also about four times lower, leading to a lower responsivity for the 12-mode. Therefore, all further evaluations are performed using the results from the resonator excited in the 15-mode. In Figure 10.9 the resonance frequencies for both parameter sets (N_{1-9} and S_{1-9}) as a function of the corresponding density values are depicted, showing a linear increase in f_{res} from 567 kHz (N_1) to 582 kHz (N_9), and again a premature stop at ~ 575 kHz for the stuck fermentation. As a next step, the density values of the model solutions are evaluated with a Stabinger SVM3000 viscometer representing a standard measurement technique. The results are listed in Table 10.5 and depicted in Figure 10.10, showing an almost linear decrease for N_{1-9} from 1.081 (N_1) to 0.996 kg/l (N_9) and a premature stop in the density decrease for S_{1-9} with a minimal value of 1.020 kg/l (S_7). Furthermore, the results of the density determination are compared to those from the Stabinger viscometer in Figure 10.10, showing low deviations and the possibility to distinguish between ordinary and stuck fermentations at an early stage of the fermentation process. Finally, the results of the frequency response analysis for real grape must fermentation are presented in Figure 10.11, showing a similar trend in the change of f_{res} , compared to those of the artificially aged solutions presented in Figure 10.7. This indicates the high potential of the presented sensor system to withstand the harsh conditions during the fermentation process even in a real grape must environment.

10.4 Conclusions

In this chapter, an approach to monitor the fermentation processes in winemaking by analyzing the frequency response of a piezoelectric MEMS resonator is presented. The sensor is excited in the 4th-order of the roof tile-shaped mode in several artificially aged grape must model solutions, representing an ordinary and a stuck wine fermentation process. During the artificial fermentation, both an increasing ethanol and a decreasing total sugar concentration reduce the density of the grape must despite the counteracting effect of the increasing

Table 10.5: Determined density values (Res.) for ordinary and stuck/sluggish model solutions and their comparison to reference values (Ref.) obtained with a Stabinger viscometer SVM3000.

Ordinary				Stuck/sluggish			
Sol.	ρ_{fluid} [kg/l]			Sol.	ρ_{fluid} [kg/l]		
-	Ref.	Res.	Dev.	-	Ref.	Res.	Dev.
N_1	1.081	1.082	-0.001	S_1	1.075	1.075	-
N_2	1.065	1.063	0.002	S_2	1.063	1.064	-0.001
N_3	1.032	1.033	-0.001	S_3	1.05	1.05	-
N_4	1.02	1.023	-0.003	S_4	1.031	1.031	-
N_5	1.007	1.01	-0.003	S_5	1.028	1.023	0.005
N_6	0.994	0.994	-	S_6	1.025	1.024	0.001
N_7	0.988	0.989	-0.001	S_7	1.02	1.029	-0.009
N_8	0.985	0.978	0.007	S_8	1.023	1.02	0.003
N_9	0.996	0.995	0.001	S_9	1.021	1.02	0.001

glycerin concentration. This decrease in density leads to higher resonance frequencies. Due to the high quality factor of the MEMS sensor in liquid media (~ 100 in isopropanol), even minor shifts in resonance frequency can be detected with high precision, which enables the possibility to monitor these changes of the physical properties during the fermentation processes. Reproducibility and reusability measurement were performed in three model solutions, showing low standard deviations in the resonance frequencies of $\sim 0.1\%$ and moderate deviations in quality factor ($\sim 11\%$) and conductance peak height ($\sim 12\%$). These results show that the resonance frequency is hardly affected by potential surface contaminates. Due to the fast measurement cycle of ~ 10 s and easy cleaning procedure, contaminates from the environment, such as the deposition of tartaric acid crystals, could be avoided. Nevertheless, minor surface contaminates reduce the precision of the calculated density values leading to a standard deviation of $\sim 1.1\%$. Finally, test measurements in real grape must were performed resulting in similar sensor characteristics compared to the results of the model solutions, demonstrating the high potential of the presented sensor concept for grape must fermentation monitoring.

Chapter 11

Conclusions and Outlook

11.1 Conclusions

High viscous damping effects in resonantly operated MEMS devices are known as most limiting factor when aiming for sensing applications of or in liquids. It was therefore the objective of this thesis to design, realize and characterize piezoelectric excited MEMS resonators to archive highly responsive sensor elements even in highly viscous liquids. Three different design architectures were introduced, all contributing to a performance increase of the sensor element. First approach was, to consider higher order modes to decrease the influence of viscous damping. Secondly, a tailored read-out mechanism is installed for each mode to address a maximal signal to noise ratio SNR. The third optimization mechanism considers a tailored resonator support, enabling a quasi-free vibration.

To validate these concepts experimentally, aluminium nitride actuated MEMS resonators were fabricated in silicon microtechnology and optically and electrically characterized in air and in several liquids. It could be shown, that higher order modes are significantly less effected by viscosity related damping and obtain high quality factors up to about 170 in liquid with a dynamic viscosity of 5 mPa·s. A substantial performance increase in terms of the SNR was archived when resonators operating at higher order modes were designed with a tailored, electronic read-out and an advanced anchor geometry. Additionally, the responsivity and sensitivity in liquids were investigated, showing superior performance for higher order modes. Acoustic energy dissipation effects via the surrounding liquid were observed starting at the 8th order mode, indicating the limit of this

sensing mechanism. In the last chapter of this thesis, it could be shown that these optimization techniques can be combined to one highly optimized sensor element, which is capable to monitor minimal physical changes during wine fermentation and it enables the distinction between ordinary and potential stuck fermentation.

From the results presented within this thesis, design guidelines for future resonator designs can be extracted, which are briefly summarized:

- higher orders of the advanced roof tile shaped mode are less effected by viscosity related damping and obtain higher quality factors
- differently strained (tensile/compressive) surface areas should be read-out separately with a tailored electrode design
- the use of higher order modes in liquids is limited due to acoustic energy dissipation
- quasi-free vibrations can be enabled by a tailored support architecture

11.2 Outlook

The advanced piezoelectric MEMS resonators feature enhanced quality factors and electrical output signals, which facilitate precise sensing of fluid properties even of highly viscous liquids (dynamic viscosity $> 500 \text{ mPa}\cdot\text{s}$). This can be beneficially used to monitor the density and viscosity of engine oils, which are known as two important parameters indicating the status of the lubricant. Furthermore the compact, ultra-low power sensor design allows the integration of the sensor element in a hand-held device, which can be used as light weight, fast and easy to use measurement equipment. Besides the measurement and monitoring of physical fluid properties, this sensing concept is also most promising for any resonator-related mass change detection in liquids. The decreased fluid related damping for higher order modes makes the resonance frequencies in liquid come near to the corresponding resonance frequencies in air. This is a strong indication that the fluid structure interaction decreases and therefore mass changes of the resonator become more effective. This can be beneficially used for the detection of e.g. bio-recognition agents on a specifically functionalized resonator surface in liquids.

Appendix A

Supplemental materials

A.1 Tables of the fluid properties as functions of temperature

In the following tables the kinematic and dynamic viscosity as well as density values are listed for several liquids. The reference values to calculate the unknown parameters K_f , m_f , k_f and d_f are listed in bold.

Table A.1: List of values for the kinematic viscosity, dynamic viscosity, the density and the inverse $\sqrt[3]{\cdot}$ -product of isopropanol in a temperature range from 0°C up to 100°C.

Temperature		Viscosity		Density	inv. $\sqrt[3]{\cdot}$ -product
T		ν_{fluid}	μ_{fluid}	ρ_{fluid}	$(\mu_{\text{fluid}} \rho_{\text{fluid}})^{-0.5}$
[°C]	[°F]	[mm ² /s]	[mPa·s]	[kg/l]	[(mPa·s·kg/l) ^{-0.5}]
0	273	6.80	4.62	0.806	0.18
10	283	4.42	3.08	0.795	0.27
20	293	3.08	2.19	0.785	0.38
30	303	2.27	1.64	0.775	0.52
40	313	1.74	1.28	0.765	0.67
50	323	1.38	1.03	0.754	0.84
60	333	1.12	0.85	0.744	1.02
70	343	0.94	0.72	0.734	1.22
80	353	0.80	0.62	0.724	1.42
90	363	0.69	0.54	0.713	1.63
100	373	0.61	0.48	0.703	1.84

Table A.2: List of values for the kinematic viscosity, dynamic viscosity, the density and the inverse $\sqrt[3]{\cdot}$ -product of viscosity standard N1 in a temperature range from 0°C up to 100°C.

Temperature		Viscosity		Density	inv. $\sqrt[3]{\cdot}$ -product
T		ν_{fluid}	μ_{fluid}	ρ_{fluid}	$(\mu_{\text{fluid}} \rho_{\text{fluid}})^{-0.5}$
[°C]	[°F]	[mm ² /s]	[mPa·s]	[kg/l]	[(mPa·s·kg/l) ^{-0.5}]
0	273	1.79	1.44	0.792	0.93
10	283	1.51	1.19	0.785	1.03
20	293	1.29	1.00	0.777	1.13
30	303	1.12	0.86	0.769	1.23
40	313	0.99	0.75	0.762	1.32
50	323	0.88	0.67	0.754	1.41
60	333	0.79	0.60	0.746	1.50
70	343	0.72	0.54	0.739	1.58
80	353	0.66	0.49	0.731	1.67
90	363	0.61	0.45	0.723	1.74
100	373	0.56	0.42	0.716	1.82

Table A.3: List of values for the kinematic viscosity, dynamic viscosity, the density and the inverse $\sqrt[3]{\cdot}$ -product of viscosity standard D5 in a temperature range from 0°C up to 100°C.

Temperature		Viscosity		Density	inv. $\sqrt[3]{\cdot}$ -product
T		ν_{fluid}	μ_{fluid}	ρ_{fluid}	$(\mu_{\text{fluid}} \rho_{\text{fluid}})^{-0.5}$
[°C]	[°F]	[mm ² /s]	[mPa·s]	[kg/l]	[(mPa·s·kg/l) ^{-0.5}]
0	273	12.72	11.29	0.854	0.32
10	283	8.92	7.67	0.847	0.39
20	293	6.55	5.51	0.840	0.47
30	303	5.00	4.13	0.833	0.54
40	313	3.94	3.21	0.826	0.61
50	323	3.18	2.56	0.820	0.69
60	333	2.63	2.10	0.813	0.77
70	343	2.21	1.75	0.806	0.84
80	353	1.89	1.49	0.799	0.92
90	363	1.64	1.29	0.792	0.99
100	373	1.43	1.13	0.785	1.06

Table A.4: List of values for the kinematic viscosity, dynamic viscosity, the density and the inverse $\sqrt[3]{\cdot}$ -product of viscosity standard N10 in a temperature range from 0°C up to 100°C.

Temperature		Viscosity		Density	inv. $\sqrt[3]{\cdot}$ -product
T		ν_{fluid}	μ_{fluid}	ρ_{fluid}	$(\mu_{\text{fluid}} \rho_{\text{fluid}})^{-0.5}$
[°C]	[°F]	[mm ² /s]	[mPa·s]	[kg/l]	[(mPa·s·kg/l) ^{-0.5}]
0	273	53.89	48.63	0.859	0.15
10	283	32.19	27.97	0.853	0.20
20	293	20.72	17.53	0.846	0.26
30	303	14.17	11.76	0.840	0.32
40	313	10.17	8.33	0.833	0.38
50	323	7.60	6.16	0.827	0.44
60	333	5.88	4.73	0.820	0.51
70	343	4.67	3.74	0.814	0.57
80	353	3.80	3.03	0.807	0.64
90	363	3.15	2.50	0.801	0.71
100	373	2.66	2.11	0.794	0.77

Table A.5: List of values for the kinematic viscosity, dynamic viscosity, the density and the inverse $\sqrt[3]{\cdot}$ -product of viscosity standard N35 in a temperature range from 0°C up to 100°C.

Temperature		Viscosity		Density	inv. $\sqrt[3]{\cdot}$ -product
T		ν_{fluid}	μ_{fluid}	ρ_{fluid}	$(\mu_{\text{fluid}} \rho_{\text{fluid}})^{-0.5}$
[°C]	[°F]	[mm ² /s]	[mPa·s]	[kg/l]	[(mPa·s·kg/l) ^{-0.5}]
0	273	309.92	284.89	0.868	0.06
10	283	153.31	135.08	0.861	0.09
20	293	84.16	71.96	0.855	0.13
30	303	50.29	42.11	0.849	0.17
40	313	32.22	26.59	0.842	0.21
50	323	21.86	17.86	0.836	0.26
60	333	15.55	12.63	0.830	0.31
70	343	11.51	9.30	0.824	0.36
80	353	8.80	7.10	0.817	0.42
90	363	6.92	5.58	0.811	0.47
100	373	5.58	4.49	0.805	0.53

Table A.6: List of values for the kinematic viscosity, dynamic viscosity, the density and the inverse $\sqrt[3]{\nu}$ -product of viscosity standard N100 in a temperature range from 0°C up to 100°C.

Temperature		Viscosity		Density	inv. $\sqrt[3]{\nu}$ -product
T		ν_{fluid}	μ_{fluid}	ρ_{fluid}	$(\mu_{\text{fluid}} \rho_{\text{fluid}})^{-0.5}$
[°C]	[°F]	[mm ² /s]	[mPa·s]	[kg/l]	[(mPa·s·kg/l) ^{-0.5}]
0	273	1617.85	1504.74	0.878	0.03
10	283	687.24	613.37	0.872	0.04
20	293	330.20	286.10	0.866	0.06
30	303	175.63	149.01	0.860	0.09
40	313	101.63	84.98	0.854	0.12
50	323	63.08	52.24	0.848	0.15
60	333	41.52	34.17	0.842	0.19
70	343	28.71	23.54	0.836	0.23
80	353	20.70	16.94	0.830	0.27
90	363	15.45	12.64	0.824	0.31
100	373	11.89	9.72	0.818	0.35

Table A.7: List of values for the kinematic viscosity, dynamic viscosity, the density and the inverse $\sqrt[3]{\nu}$ -product of viscosity standard S200 in a temperature range from 0°C up to 100°C.

Temperature		Viscosity		Density	inv. $\sqrt[3]{\nu}$ -product
T		ν_{fluid}	μ_{fluid}	ρ_{fluid}	$(\mu_{\text{fluid}} \rho_{\text{fluid}})^{-0.5}$
[°C]	[°F]	[mm ² /s]	[mPa·s]	[kg/l]	[(mPa·s·kg/l) ^{-0.5}]
0	273	3464.41	3226.50	0.883	0.02
10	283	1399.91	1254.12	0.877	0.03
20	293	642.10	559.20	0.871	0.05
30	303	327.20	279.24	0.865	0.06
40	313	182.04	153.17	0.859	0.09
50	323	109.02	90.85	0.853	0.11
60	333	69.47	57.53	0.847	0.14
70	343	46.65	38.48	0.841	0.18
80	353	32.75	26.96	0.835	0.21
90	363	23.88	19.65	0.829	0.25
100	373	17.98	14.80	0.823	0.29

Table A.8: List of values for the kinematic viscosity, dynamic viscosity, the density and the inverse $\sqrt[3]{\cdot}$ -product of viscosity standard D500 in a temperature range from 0°C up to 100°C.

Temperature		Viscosity		Density	inv. $\sqrt[3]{\cdot}$ -product
T		ν_{fluid}	μ_{fluid}	ρ_{fluid}	$(\mu_{\text{fluid}} \rho_{\text{fluid}})^{-0.5}$
[°C]	[°F]	[mm ² /s]	[mPa·s]	[kg/l]	[(mPa·s·kg/l) ^{-0.5}]
0	273	4599.71	4277.39	0.884	0.02
10	283	1818.48	1628.37	0.878	0.03
20	293	817.80	712.40	0.872	0.04
30	303	409.39	349.64	0.866	0.06
40	313	224.16	188.80	0.860	0.08
50	323	132.33	110.41	0.854	0.10
60	333	83.24	69.03	0.849	0.13
70	343	55.25	45.65	0.843	0.16
80	353	38.39	31.66	0.837	0.19
90	363	27.73	22.86	0.831	0.23
100	373	20.71	17.08	0.825	0.27

A.2 Electrical conductivity values for artificially aged grape must model solutions

Table A.9: Determined electrical conductivity η_{fluid} of both, ordinary (N_{1-9}) and stuck (S_{1-9}) model solutions at 10 and 20°C. obtained with a WTW LF 323-A conductivity meter. The values in brackets are interpreted as incorrectly executed measurements.

Ordinary			Stuck/sluggish		
Sol.	η_{fluid} [$\mu\text{S}/\text{cm}$]		Sol.	η_{fluid} [$\mu\text{S}/\text{cm}$]	
-	(10°C)	(20°C)	-	(10°C)	(20°C)
N_1	6.9	8.3	S_1	6.6	7.3
N_2	5.9	6.8	S_2	6.6	7.2
N_3	5.2	5.3	S_3	6.0	6.4
N_4	3.8	4.5	S_4	4.5	5.1
N_5	(-9.6)	(-10.8)	S_5	3.8	4.2
N_6	2.3	2.7	S_6	4.0	4.3
N_7	2.0	2.2	S_7	3.6	3.9
N_8	1.8	2.1	S_8	3.6	3.9
N_9	2.4	2.8	S_9	4.1	4.5

A.3 Table collection for Chapter 7

Table A.10: Electrical evaluated parameters of the higher orders of the roof tile-shaped modes in D5 with optimized electrode design (OED).

#	Leissa's Nom.	f_{res} [kHz]	Q [1]	ΔG [mS]	$\Delta G/Q$ [μS]
1	12	55.69	25	0.006	0.24
2	13	162.17	44	0.040	0.90
3	14	338.79	62	0.13	3.73
4	15	593.44	85	0.32	5.81
5	16	918.00	102	0.59	8.13
6	17	1321.70	123	1.00	11.27
7	18	1790.69	129	1.45	13.49
8	19	2372.12	146	1.97	14.24
9	1A	2967.05	138	2.23	16.21
10	1B	3631.54	171	3.03	17.73

Table A.11: Electrical evaluated parameters of the higher orders of the roof tile-shaped modes in N10 with optimized electrode design (OED).

#	Leissa's Nom.	f_{res} [kHz]	Q [1]	ΔG [mS]	$\Delta G/Q$ [μS]
1	12	54.56	14	0.0032	0.23
2	13	160.01	26	0.022	0.85
3	14	335.40	36	0.075	2.12
4	15	589.08	48	0.17	3.63
5	16	911.38	59	0.34	5.88
6	17	1314.15	72	0.57	7.98
7	18	1782.31	80	0.89	11.17
8	19	2362.03	89	1.23	13.84
9	1A	2960.44	92	1.53	16.56
10	1B	3626.38	97	1.89	19.44

Table A.12: Electrical evaluated parameters of the higher orders of the roof tile-shaped modes in S20 with optimized electrode design (OED).

#	Leissa's Nom.	f_{res} [kHz]	Q [1]	ΔG [mS]	$\Delta G/Q$ [μS]
1	12	53.67	10	0.0023	0.22
2	13	158.37	18	0.016	0.91
3	14	332.41	28	0.044	1.59
4	15	585.13	33	0.12	3.76
5	16	906.72	40	0.24	6.00
6	17	1308.80	48	0.30	6.30
7	18	1776.00	55	0.61	11.13
8	19	2355.83	61	0.85	13.98
9	1A	2954.53	65	1.08	16.67
10	1B	3619.96	70	1.24	17.71

Table A.13: Electrical evaluated parameters of the higher orders of the roof tile-shaped modes in N35 with optimized electrode design (OED).

#	Leissa's Nom.	f_{res} [kHz]	Q [1]	ΔG [mS]	$\Delta G/Q$ [μS]
1	12	52.58	7	0.0016	0.22
2	13	156.47	13	0.011	0.90
3	14	3302.33	17	0.037	2.16
4	15	581.46	23	0.089	3.79
5	16	902.14	28	0.17	5.98
6	17	1303.46	34	0.28	8.18
7	18	1769.91	38	0.42	11.07
8	19	2349.08	44	5.78	13.17
9	1A	2947.91	46	0.80	17.21
10	1B	3615.18	47	0.90	19.33

Table A.14: Electrical evaluated parameters of the higher orders of the roof tile-shaped modes in N100 with optimized electrode design (OED).

#	Leissa's Nom.	f_{res} [kHz]	Q [1]	ΔG [mS]	$\Delta G/Q$ [μS]
1	12	50.74	3	0.00093	0.30
2	13	151.88	6	0.0060	1.01
3	14	322.94	8	0.019	2.24
4	15	572.39	11	0.044	4.06
5	16	898.80	13	0.065	4.86
6	17	1289.9	15	0.14	8.96
7	18	1755.93	17	0.22	12.47
8	19	2337.00	20	0.31	15.92
9	1A	2938.62	22	0.36	16.01
10	1B	3602.84	22	0.52	23.39

Table A.15: Electrical evaluated parameters of the higher orders of the roof tile-shaped modes in D500 with optimized electrode design (OED).

#	Leissa's Nom.	f_{res} [kHz]	Q [1]	ΔG [mS]	$\Delta G/Q$ [μS]
1	12	49.01	2	0.00064	0.32
2	13	149.84	3	0.0044	1.28
3	14	318.39	6	0.0132	2.32
4	15	567.42	7	0.031	4.31
5	16	884.64	9	0.059	6.58
6	17	1283.55	11	0.11	9.29
7	18	1748.26	13	0.16	12.78
8	19	2326.66	14	0.23	16.34
9	1A	2927.33	15	0.30	20.33
10	1B	3594.24	16	0.40	24.23

A.4 Program code for sensitivity estimation

```

1 %%-----generate noise-----
2 for nr = 1 : noise.nr
3 for nnr = 1 : noise.steps
4 if(loopSNR ==1)
5     noise.amp = noise.ampgrid(nnr);
6 elseif(loopcSNR == 1);
7     SNRconst = noise.constgrid(nnr);
8     if(nnr>1)
9         nnr;
10    end
11 else
12    noise.amp = noise.amp;
13 end
14 for k = mode_start: mode_max
15     for l = fl_start : fl_max
16         noise.wgn(l,k,:,nr) = wgn(1,points,noise.pw);
17     end
18 end
19 for k = fl_start : fl_max
20     for l = mode_start : mode_max
21         if(SNRconst == 0)
22             noise.wgn(k,l,:,nr) = noise.wgn(k,l,:,nr)
23             *(noise.d+noise.b*data.fr(k,l)
24             +noise.b2*data.fr(k,l).^2)*noise.amp;
25         else
26             noise.wgn(k,l,:,nr) = noise.wgn(k,l,:,nr)*data.dG(k,l)
27             ./SNRconst;
28         end
29     end
30 end
31 noise.G(:,:,,nr) = data.G(:,:,) + noise.wgn(:,:,,nr);
32 noise.B(:,:,,nr) = data.B(:,:,) + noise.wgn(:,:,,nr);
33 end
34 %%-----end-----

1 %Quellcode Matlab

```

List of Figures

1.1	Comparison of the sensor responsivity \mathcal{R} and the actuator potential \mathcal{P} for NEMS, MEMS and macroscopic transducers. . . .	4
2.1	Single degree of freedom system.	8
2.2	Normalized free vibration displacement response of a damped single degree of freedom system with a damping ratio $\zeta = 0.1$. . .	11
2.3	Normalized displacement response of a harmonically excited vibration with various damping ratios ζ	13
2.4	Electro-mechanical analogy of the first order.	14
2.5	Schematic of the first four bending modes for beams with (a) clamped-free, (b) clamped-clamped and (c) free-free support. . .	18
3.1	Simplified Heckmann diagram	21
4.1	Comparison of the velocity v and Reynolds number Re for different objects in air and water [91].	26
4.2	Experimentally estimation of the dominant characteristic length \mathcal{L} for a cantilever beam with a length L_b of 2500 μm , a width W_b of 1200 μm , a fundamental resonance frequency in vacuum of ~ 5 kHz and a speed of sound v_c of ~ 1000 m/s.	28
5.1	Schematical illustration of the process steps, including (a) the SOI substrate, (b) the deposition of the bottom electrode, (c and f) the deposition steps of the two titanium sacrificial layers, (d) the deposition of the piezoelectric AlN thin film, (e) the deposition of the top electrode, (g) the AlN lift-off process, and (h) the front and (i) the back side release.	32

5.2	Optical micrograph of the finished fabricated bi-directional transducers featuring resonators with different dimensions and their non-released counterparts [105].	32
6.1	Picture of the utilized measurement box.	36
6.2	Illustration of the 4-wire measurement technique using an Agilent A294A impedance analyzer, including feed line resistances of the measurement equipment R_{feed} and the high and low potentials HI_{Source} , HI_{Sense} , LO_{Source} and LO_{Sense}	37
6.3	Illustration of a representative frequency response in terms of (a) the electrical conductance G and (b) the electrical susceptance B of a transducer, immersed in a viscosity standard with a density of 0.840 kg/l and a dynamic viscosity $\mu_{\text{fluid}} = 6.55 \text{ mPa}\cdot\text{s}$ at 20°C resulting in a resonance frequency of $f_{\text{res}} \sim 162 \text{ kHz}$	37
6.4	Equivalent electrical circuit of piezoelectric actuated resonator.	39
6.5	Comparison of the frequency responses for two different feed line resistances of $R_s = 10 \Omega$ in (a) and $R_s = 500 \Omega$ in (b).	39
6.6	Illustration of an optical surface scan of a micro structure in (a) and a sample measurement illustration an advanced out-of-plane bending mode in (b).	42
6.7	Block diagram of a laser Doppler vibrometer (LDV).	42
6.8	Picture of a typical laser Doppler vibrometer measurement.	44
7.1	Cross-section illustration of FEM eigenmode analysis for the first ten orders (a-j) of the roof tile-shaped mode of single-side clamped plates ($2524 \times 1274 \times 20 \mu\text{m}^3$).	49
7.2	Illustration of FEM eigenmode analysis for the first ten orders (a-j) of the roof tile-shaped mode of single-side clamped plates ($2524 \times 1274 \times 20 \mu\text{m}^3$) both in front (upper) and top view (lower).	50
7.3	Optical micrograph of a typical die layout ($6 \times 6 \text{ mm}^2$), packaged and wire bonded in a 24-pin dual inline package, containing one single-side clamped plate ($2524 \times 1274 \times 20 \mu\text{m}^3$) with an electrode design optimized for the 10 th order (1B-mode).	51
7.4	Conductance and noise characteristics for the first ten orders of the roof tile-shaped mode in D5 and D500 at 20°C.	51

7.5	Sensor output parameter ($f_{\text{res}}(\text{fluid})/f_{\text{res}}(\text{air})$, quality factor Q and electrical conductance peak ΔG) over the mode order n for all investigated liquids (i.e. D5, N10, N35, N100 and D500) in (a-c) and over the sensor input parameter χ for even order modes in (d-f), respectively.	54
7.6	Relative responsivity grouped into the two resonance frequency regimes (i.e. $f_{\chi=\text{low}}$ and $f_{\chi=\text{high}}$), the quality factor Q and the conductance peak ΔG over the mode order n . The dashed lines serve as guide to the eye.	55
7.7	Frequency response with artificially generated white Gaussian noise for (a) SNR = 1, (b) SNR = 5 and (c) SNR = 100.	56
7.8	Relative standard deviations σ over SNR and quality factor of the resonance frequency in (a), the quality factor in (b) and the conductance peak in (c) and representative histograms at SNR = 200 and $Q = 25$ in (d), (e) and (f).	56
7.9	Sensitivity \mathcal{S} over mode order n for the two resonance frequency regimes ($f_{\chi=\text{low}}$ and $f_{\chi=\text{high}}$), for the conductance peak ΔG and for the quality factor Q in D5 at 20°C. The dashed lines serve as guide to the eye.	58
7.10	Quality factor Q over mode number n in D5 and N1 at 20°C. The dashed lines serve as guide to the eye.	59
7.11	Normalized angular frequency over mode number n in D5 and N1 at 20°C. The dashed lines serve as guide to the eye.	59
8.1	Optical micrographs of piezoelectrically actuated plate-type resonators with a length of $L_{\text{plate}} = 2524 \mu\text{m}$, a width of $W_{\text{plate}} = 1274 \mu\text{m}$, a thickness of $T_{\text{plate}} = 20 \mu\text{m}$ but with three different clamping conditions.	62
8.2	Visualization of the fundamental (a-c) roof tile-shaped modes (X2-modes) and the 2 nd orders (d-e) of the roof tile-shaped mode (X3-modes) for a single-side clamped plate (a, d), a double-side clamped plate (b, e) and a free-free clamped plate (c, f), respectively. The colored areas on the cantilever surface represent the local surface strain distribution.	63

8.3	Top view of the presented roof tile-shaped modes from Figure 8.2, showing (a) the 12-mode, (b) the 22-mode, (c) the 02-mode, (d) the 13-mode, (e) the 23-mode and (f) the 03-mode. The colored areas on the plate surfaces represent the local surface strain distribution. Red indicates areas with tensile strain and blue indicates areas compressive strain, respectively.	64
8.4	Optical (a) and electrical (b) characterization of the X2-and X3-mode in air.	66
8.5	Electrical characterization of the X2- and X3-modes in different liquids represented by the conductance peak ΔG as a function of the inverse viscosity-density square root product.	66
8.6	Piezoelectric response $\Delta G/Q$ over the inverse viscosity-density square root product in different liquids (isopropanol, and viscosity standards D5, N10 N100, D500).	68
9.1	Schematic cross-sectional view of the MEMS resonator illustrating the electrode design and the plate support of the 03-mode. .	70
9.2	Optical micrograph of piezoelectrically excited and resonantly operating plate-type resonators with quasi free-free plate support optimized for (a) the first and (b) the second order of the 0X-modes.	72
9.3	Visualization of the 1 st (02-mode), 2 nd (03-mode), 3 rd (04-mode) and 4 th (05-mode) order of the roof tile-shaped mode (a-d) and the corresponding top views (e-h). The colored areas on the plate surface represent the local surface strain distribution with tensile strain (red) and compressive strain (blue), respectively. The positive (+) and the negative (-) sign indicate, in combination with the black rectangles, the optimized electrode design and the polarity of each electrode stripe.	73
9.4	Nodal analysis of the support boundary conditions for (a) the 02-mode, (b) the 03-mode, (c) the 04-mode and (d) the 05-mode in air, including results from analytical calculations, FEM simulations, LDV measurements and the illustration of the plate-supports indicated by cyan colored areas.	74
9.5	Quality factors of the 0X-modes with and without OED in different liquids.	76

9.6	Electrical characterization of the 0X-modes with and without OED in different liquids represented by the conductance peak ΔG as a function of the resonance frequency.	77
9.7	piezoelectric response $\Delta G/Q$ as a function of the inverse square root viscosity/density product with and without OED in different liquids.	77
10.1	Optical micrograph of the in-house fabricated silicon die ($6 \times 6 \text{ mm}^2$), containing one piezoelectric actuated plate (dimensions: $2524 \times 1274 \times 20 \mu\text{m}^3$) using advanced electrode patterning considering the volume-strain of the modal shape presented in Figure 10.2.	82
10.2	Visualization of the side view in (a) and the top view in (b) for a plate excited in the 4 th order of the roof tile-shaped mode (15-mode). The colored areas on the cantilever surface represent the local volume strain distribution.	82
10.3	Schematic cross-sectional view on the MEMS resonator illustrating the electrode design of the 15-mode.	83
10.4	Reproducibility measurement of two model solutions of an ordinary fermented grape must (N_3 and N_7) in (a), and of a stuck fermented grape must (S_7) in (b) at 22°C.	84
10.5	Electrical output characteristics of the piezoelectric MEMS resonator for an ordinary fermentation process N_{1-9} , starting with N_1 at the bottom and all other model solutions (N_2-N_9) stacked above. The y-axis is scaled as arbitrary unit [a.u.].	87
10.6	Electrical output characteristics of the piezoelectric MEMS resonator for a stuck fermentation process S_{1-9} , starting with S_1 at the bottom and all other model solutions (S_2-S_9) stacked above. The y-axis is scaled as arbitrary unit [a.u.].	88
10.7	15-mode frequency response analysis of an ordinary (N_{1-9}) and a stuck (S_{1-9}) fermentation process in comparison to the nominal ethanol concentration of the investigated model solutions. The inserted lines serve as guide to the eye.	89
10.8	12-mode frequency response analysis of an ordinary and a stuck fermentation process in comparison to the nominal ethanol concentration of the investigated model solutions. The inserted lines serve as guide to the eye.	90

10.9	Correlation between the calculated density and the measured resonance frequency for an ordinary (red) and a stuck (black) fermentation process. The inserted lines serve as guide to the eye.	90
10.10	Density values for ordinary (N_{1-9}) and stuck (N_{1-9}) fermented model solutions evaluated with the presented resonator (unfilled dots) and its reference values obtained with a Stabinger viscometer SVM3000 (filled dots). The inserted dashed lines serve as guides to the eye.	91
10.11	Frequency response of the 15-mode in a real grape over fermentation time t_{ferm} at 20°C.	91

List of Tables

2.1	Electrical and mechanical parameters of the electro-mechanical analogy of the first order.	14
2.2	Boundary values for the solution of the displacement function of beams with clamped-free, clamped-clamped and free-free support. The quotation marks ', ' and ''' represent the first, second and third deviation over x ($\frac{\partial}{\partial x}$, $\frac{\partial^2}{\partial x^2}$ and $\frac{\partial^3}{\partial x^3}$), respectively.	17
2.3	Calculated normalized wavenumber $C_n = \beta_n L_b$ for clamped-free, clamped-clamped and free-free supported beams for arbitrary modal number n	18
3.1	Material related electrical and mechanical properties of sputter deposited lead zirconate titanate (PZT), aluminium nitride (AlN) and zinc oxide (ZnO) thin films [60–75].	23
6.1	Typical values for the electrical components of the motional, parallel and serial part of the advanced equivalent electrical circuit.	40
6.2	Sample measurements of a piezoelectric actuated resonator at different excitation voltage V_{exc} in isopropanol, measured at 20°C.	41
7.1	Mode dependency of the resonance frequency f_{res} , the quality factor Q , the electrical conductance peak ΔG and the ratio $\Delta G/Q$ measured in D5 at 20°C. The values in the last column are reference values taken from Ref. [39]	52
8.1	Summary of quality factor (Q), the electrical conductance peak ΔG and the piezoelectric response $\Delta G/Q$ for resonators excited in the 2 nd order mode with clamped-free, clamped-clamped and quasi free-free support boundary conditions in isopropanol at room temperature.	65

9.1	MEMS resonator designs: Geometrical dimensions for the 02-, 03-, 04- and 05-mode.	71
9.2	Performance of the higher order roof tile-shaped modes in isopropanol with and without OED excitation.	72
10.1	Characterization of the resonator in air. $R_{m,air}$, $L_{m,air}$, and $C_{m,air}$ represent the unperturbed resonator in air.	83
10.2	Chemical composition of model solutions representing a desired wine fermentation process from N_1 (raw grape must) up to N_9 (ordinary fermented model solution) [17]. The measured values are obtained using a R200D microscale from Sartorius.	85
10.3	Chemical composition of model solutions representing a stuck wine fermentation process from S_1 (raw grape must) up to S_9 (stuck fermented model solution) [17]. The measured values are obtained using a R200D microscale from Sartorius.	86
10.4	Electrical parameters of ordinary(N_{1-9}) and stuck(S_{1-9}) model solutions evaluated with Agilent 4294A impedance analyzer.	88
10.5	Determined density values (Res.) for ordinary and stuck/sluggish model solutions and their comparison to reference values (Ref.) obtained with a Stabinger viscometer SVM3000.	93
A.1	List of values for the kinematic viscosity, dynamic viscosity, the density and the inverse ν -product of isopropanol in a temperature range from 0°C up to 100°C.	97
A.2	List of values for the kinematic viscosity, dynamic viscosity, the density and the inverse ν -product of viscosity standard N1 in a temperature range from 0°C up to 100°C.	98
A.3	List of values for the kinematic viscosity, dynamic viscosity, the density and the inverse ν -product of viscosity standard D5 in a temperature range from 0°C up to 100°C.	98
A.4	List of values for the kinematic viscosity, dynamic viscosity, the density and the inverse ν -product of viscosity standard N10 in a temperature range from 0°C up to 100°C.	99
A.5	List of values for the kinematic viscosity, dynamic viscosity, the density and the inverse ν -product of viscosity standard N35 in a temperature range from 0°C up to 100°C.	99

A.6	List of values for the kinematic viscosity, dynamic viscosity, the density and the inverse $\sqrt[3]{\nu}$ -product of viscosity standard N100 in a temperature range from 0°C up to 100°C.	100
A.7	List of values for the kinematic viscosity, dynamic viscosity, the density and the inverse $\sqrt[3]{\nu}$ -product of viscosity standard S200 in a temperature range from 0°C up to 100°C.	100
A.8	List of values for the kinematic viscosity, dynamic viscosity, the density and the inverse $\sqrt[3]{\nu}$ -product of viscosity standard D500 in a temperature range from 0°C up to 100°C.	101
A.9	Determined electrical conductivity η_{fluid} of both, ordinary (N_{1-9}) and stuck (S_{1-9}) model solutions at 10 and 20°C. obtained with a WTW LF 323-A conductivity meter. The values in brackets are interpreted as incorrectly executed measurements.	102
A.10	Electrical evaluated parameters of the higher orders of the roof tile-shaped modes in D5 with optimized electrode design (OED).	103
A.11	Electrical evaluated parameters of the higher orders of the roof tile-shaped modes in N10 with optimized electrode design (OED).	103
A.12	Electrical evaluated parameters of the higher orders of the roof tile-shaped modes in S20 with optimized electrode design (OED).	104
A.13	Electrical evaluated parameters of the higher orders of the roof tile-shaped modes in N35 with optimized electrode design (OED).	104
A.14	Electrical evaluated parameters of the higher orders of the roof tile-shaped modes in N100 with optimized electrode design (OED).	105
A.15	Electrical evaluated parameters of the higher orders of the roof tile-shaped modes in D500 with optimized electrode design (OED).	105

List of Abbreviations

AlN	aluminium nitride
AC	alternating current [A]
ALD	atomic layer deposition
A_1	constant [m]
a_1	constant [s^{-1}]
a_2	constant [s^{-2}]
A	cross section area [m^2]
BAW	bulk acoustic wave
B	electrical susceptance [S]
B_1	constant [m]
β_n	wavenumber [m^{-1}]
β_1	wavenumber for modal number $n = 1$ [m^{-1}]
CMOS	complementary metal–oxide–semiconductor
CO₂	carbon dioxide
C_1	constant [m]
C_2	constant [m]
C_3	constant [m]
C_4	constant [m]

c	damping constant [kg/s]
c_c	critical damping [1]
C_m	equivalent capacitance for the electromechanical analogy of the first order [F]
C	constant [m]
C_p	equivalent capacitance representing the capacity of the piezoelectric layer [F]
C_{m_air}	equivalent capacitance for the electromechanical analogy of the first order in air [F]
C_n	normalized wavenumber [1]
DIP	dual inline package
DRIE	deep reactive-ion etching
$\Delta\varphi$	phase difference [°]
DC	direct current [A]
$\dot{z}(t)$	velocity in z-direction [m/s]
D	electric displacement field [As/m ²]
d	piezoelectric tensor [pm/V]
ΔG	conductance peak [S]
$\Delta G/Q$	piezoelectric response [S]
$\dot{x}(t)$	velocity in x-direction [m/s]
$\ddot{x}(t)$	acceleration in x-direction [m/s ²]
d_1	parameter [$\Omega \cdot l \cdot s \cdot kg^{-1}$]
d_2	parameter [$s \cdot \Omega \cdot (mPa \cdot kg/l)^{0.5}$]
d_f	offset in the linear description of the fluid density [kg/l]

Δoutput	sensor output
Δinput	sensor input
δoutput	relative sensor output
$\delta\mathcal{R}$	relative sensor responsivity
DI-H₂O	deionized water
ε	permittivity [As/Vm]
E	electric field strength [V/m]
e	piezoelectric tensor [pm/V]
η_{fluid}	electrical conductivity of the fluid [S/m]
\mathcal{E}	Young's modulus [1]
FEM	finite element method
f_0	laser frequency [Hz]
f_b	Bragg cell frequency shift [Hz]
f_d	Doppler frequency shift [Hz]
f_{res}	resonance frequency [Hz]
$f_{\text{max}(B)}$	frequency at maximal susceptance [Hz]
$f_{\text{min}(B)}$	frequency at minimal susceptance [Hz]
$F_{\mathbf{k}}$	force proportional to the displacement $x(t)$ [N]
$F_{\mathbf{c}}$	force proportional to the velocity $\dot{x}(t)$ [N]
$F_{\mathbf{m}}$	force proportional to the acceleration $\ddot{x}(t)$ [N]
F_0	amplitude of the exciting force [N]
F_{extern}	external force [N]
F	force [N]

F_{viscous}	viscous forces [N]
F_{inertial}	inertial forces [N]
$f_{\text{vac},1}$	resonance frequency in vacuum for $n = 1$ [Hz]
$f_{\chi=\text{low}}$	resonance frequency regime for low values of χ ($< 0.14 \text{ (mPa}\cdot\text{s}\cdot\text{kg/l)}^{-0.5}$) [Hz]
$f_{\chi=\text{high}}$	resonance frequency regime for high values of χ ($> 0.14 \text{ (mPa}\cdot\text{s}\cdot\text{kg/l)}^{-0.5}$) [Hz]
G	electrical conductance [G]
H_3PO_4	phosphoric acid
HF	hydrofluoric acid
$\Gamma_{\text{i}}(\omega_{\text{fluid}}, n)$	imaginary part of the hydrodynamic function for modal number n
$\Gamma_{\text{r}}(\omega_{\text{fluid}}, n)$	real part of the hydrodynamic function for modal number n
Γ	complex hydrodynamic function
HI_{Source}	high source potential [V]
HI_{Sense}	high sense potential [A]
I_{total}	total intensity of the interferometer [W/m^2]
I_{obj}	intensity of the object beam [W/m^2]
I_{ref}	intensity of the reference beam [W/m^2]
i	complex number [1]
I_{m}	equivalent electrical current for the electromechanical analogy of the first order [A]
\mathcal{I}	momentum of inertia [m^4]
I_{Sensing}	electrical current through the transducers [A]
k	spring constant [kg/s^2]

k_f	gradient in the linear description of the fluid density [$^{\circ}\text{C}\cdot\text{kg}/\text{l}$]
K_f	offset in the non-linear description of the fluid viscosity
λ_{laser}	wavelength of the laser [m]
LDV	laser Doppler vibrometer
LPCVD	low pressure chemical vapor deposition
L_{plate}	plate length [m]
λ	constant [s^{-1}]
$\lambda_{1,2}$	constant [s^{-1}]
λ_1	constant [1]
λ_2	constant [1]
L_m	equivalent inductance for the electromechanical analogy of the first order [H]
$L_{m,\text{air}}$	equivalent inductance for the electromechanical analogy of the first order in air [H]
\mathcal{L}	characteristic length [m]
L_b	length of the beam [m]
λ_{sound}	acoustic wavelength [m]
λ_{beam}	spatial wavelength of the beam [m]
LO_{Source}	low source potential [V]
LO_{Sense}	low sense potential [A]
MSV	microscope scanning vibrometer
MEMS	microelectromechanical system
MBE	molecular beam epitaxy
μ_{fluid}	dynamic viscosity of the fluid [$\text{mPa}\cdot\text{s}$]

m	mass [kg]
μ	dynamic viscosity [mPa·s]
m_f	gradient in the non-linear description of the fluid density
NEMS	nanoelectromechanical system
N_1	artificially aged model solution for ordinary fermentation: N_1
N_2	artificially aged model solution for ordinary fermentation: N_2
N_3	artificially aged model solution for ordinary fermentation: N_3
N_4	artificially aged model solution for ordinary fermentation: N_4
N_7	artificially aged model solution for ordinary fermentation: N_7
N_9	artificially aged model solution for ordinary fermentation: N_9
ν_{fluid}	kinematic viscosity of the fluid [mm ² /s]
N_{1-9}	artificial model solution for ordinary wine fermentation
n	modal number [1]
ν	kinematic viscosity [mm ² /s]
n_{crit}	critical modal number [1]
$n_{\text{nodal_lines}}$	number of nodal lines [1]
$n_{\text{electrodes}}$	number of electrodes [1]
OED	optimized electrode design
PZT	lead zirconate titanate
PECVD	plasma-enhanced chemical vapor deposition
φ	argument [°]
ϕ_n	nominal mode shape for modal number n [1]
Q_{medium}	environmental losses [1]

Q_{clamping}	clamping losses [1]
Q_{other}	other losses [1]
$Q_{\text{intrinsic}}$	intrinsic losses [1]
Q	quality factor [1]
rms	root mean square
r_{obj}	path length of the object beam [m]
r_{ref}	path length of the reference beam [m]
R_{p}	equivalent resistance representing the parallel resistance of the piezoelectric layer [Ω]
R_{s}	equivalent ohmic resistance representing the resistance of the feed lines [Ω]
ρ_{fluid}	density of the fluid [kg/l]
R_{m}	equivalent ohmic resistance for the electromechanical analogy of the first order [Ω]
R	total electrical resistance [Ω]
$R_{\text{m_air}}$	equivalent ohmic resistance for the electromechanical analogy of the first order in air [Ω]
ϱ_{b}	areal mass density of the beam [kg/m ²]
χ	inverse viscosity-density square root product [(mPa·s·kg/l) ^{-0.5}]
$(\rho_{\text{fluid}} \cdot \mu_{\text{fluid}})^{-0.5}$	inverse viscosity-density square root product
$(\text{mPa} \cdot \text{s} \cdot \text{kg}/\text{l})^{-0.5}$	unit of the inverse viscosity-density square root product
Re	Reynolds number [1]
ϱ	mass density [kg/l]
R_{feed}	feed line resistance of the measurement equipment [Ω]
\mathcal{R}	sensor responsivity

\mathcal{P}	actuator potential
SAW	surface acoustic wave
SOI	Silicon On Insulator
SiO₂	silicon dioxide
Si₃N₄	silicon nitride
S	strain [Pa]
s	compliance tensor [1]
S_{1-9}	artificially aged model solution for stuck wine fermentation
SDOF	single degree of freedom
S_1	artificially aged model solution for stuck fermentation: S_1
S_2	artificially aged model solution for stuck fermentation: S_2
S_4	artificially aged model solution for stuck fermentation: S_4
S_7	artificially aged model solution for stuck fermentation: S_7
S_9	artificially aged model solution for stuck fermentation: S_9
σ_{Ethanol}	ethanol concentration [% v/v]
SNR	signal to noise ratio [1]
\mathcal{S}	sensor sensitivity
σ	standard deviation
ϑ	temperature [°C]
T	mechanical stress [Pa]
ϑ_c	Curie-Temperature [°C]
t_{iso}	wafer passivation thickness [m]
t_{AlN}	aluminium nitride thickness [m]

t_{be}	bottom electrode thickness [m]
t_{te}	top electrode thickness [m]
t	time [s]
T_{plate}	plate thickness [m]
t_{ferm}	fermentation time [h]
V_{exc}	excitation voltage [V]
v	velocity [m/s]
v_{c}	speed of sound [m/s]
W_{plate}	plate width [m]
w_{o}	outer electrode width [m]
w_{i}	inner electrode width [m]
ω_{0}	natural angular frequency [Hz]
ω	angular frequency [Hz]
ω_{d}	damped natural angular frequency [Hz]
W	width [m]
ω_{vac}	angular frequency in vacuum [Hz]
ω_{fluid}	angular frequency in the fluid [Hz]
ω_{res}	angular resonance frequency [Hz]
ω_{n}	natural angular frequency for a specific modal number n [Hz]
W_{b}	beam width [m]
$x(t)$	displacement in x-direction [m]
X_{e}	electrical reactance [Ω]
X	amplitude of oscillation [m]

Y	electrical admittance [S]
ZnO	zinc oxide
$z(t)$	displacement in z-direction [m]
z_{avg}	averaged displacement [m]
ζ	damping ratio [1]
Z	total impedance [Ω]
Z_{m}	impedance of the motional part of the equivalent circuit [Ω]
$z(x, t)$	beam deflection [m]
Z_{n}	solution of the displacement function [m]

Bibliography

- [1] G. Pfusterschmied, J. Toledo, M. Kucera, W. Steindl, S. Zemmann, V. Ruiz-Díez, M. Schneider, A. Bittner, J. Sanchez-Rojas, and U. Schmid, “Potential of Piezoelectric MEMS Resonators for Grape Must Fermentation Monitoring,” *Micromachines*, vol. 8, no. 7, p. 200, 2017.
- [2] J. Fraden, *Data Acquisition*, pp. 1–11. Cham: Springer International Publishing, 2016. ISBN: 9783319193038.
- [3] E. Winner, *The Audio Expert: Everything You Need to Know About Audio*. 1 ed., 2012. ISBN: 9780240821009.
- [4] K. E. Petersen, “Silicon as a mechanical material,” *Proceedings of the IEEE*, vol. 70, no. 5, pp. 420–457, 1982.
- [5] G. Shi, C. S. Chan, W. J. Li, K. S. Leung, Y. Zou, and Y. Jin, “Mobile Human Airbag System for Fall Protection Using MEMS Sensors and Embedded SVM Classifier,” *IEEE Sensors Journal*, vol. 9, no. 5, pp. 495–503, 2009.
- [6] R. Urquiza, “The Future of Middle Ear Implants, Ear Transduction and Transducers for the Ear,” *Annals of Clinical Otolaryngology*, vol. 2, no. 1, 2017.
- [7] H.-K. Kim, S. Lee, and K.-S. Yun, “Capacitive tactile sensor array for touch screen application,” *Sensors and Actuators A: Physical*, vol. 165, no. 1, pp. 2–7, 2011.
- [8] B. Robert, “Recent developments in MEMS sensors: a review of applications, markets and technologies,” *Sensor Review*, vol. 33, no. 4, pp. 300–304, 2013.

- [9] G. Meyer and N. M. Amer, “Novel optical approach to atomic force microscopy,” *Applied Physics Letters*, vol. 53, no. 12, pp. 1045–1047, 1988.
- [10] W.-M. Zhang, H. Yan, Z.-K. Peng, and G. Meng, “Electrostatic pull-in instability in MEMS/NEMS: A review,” *Sensors and Actuators A: Physical*, vol. 214, pp. 187–218, 2014.
- [11] F. J. Morin, T. H. Geballe, and C. Herring, “Temperature Dependence of the Piezoresistance of High-Purity Silicon and Germanium,” *Physical Review*, vol. 105, no. 2, pp. 525–539, 1957.
- [12] L. Xinxin, T. Ono, W. Yuelin, and M. Esashi, “Study on ultra-thin NEMS cantilevers - high yield fabrication and size-effect on Young’s modulus of silicon,” in *Technical Digest. MEMS 2002 IEEE International Conference. Fifteenth IEEE International Conference on Micro Electro Mechanical Systems (Cat. No.02CH37266)*, pp. 427–430.
- [13] S. Schmid, G. Villanueva, and M. L. Roukes, *Fundamentals of Nanomechanical Resonators*. Springer, 2016. ISBN: 9783319286891.
- [14] M. Li, H. X. Tang, and M. L. Roukes, “Ultra-sensitive NEMS-based cantilevers for sensing, scanned probe and very high-frequency applications,” *Nature Nanotechnology*, vol. 2, p. 114, 2007.
- [15] M. S. Hanay, S. Kelber, A. K. Naik, D. Chi, S. Hentz, E. C. Bullard, E. Colinet, L. Duraffourg, and M. L. Roukes, “Single-protein nanomechanical mass spectrometry in real time,” *Nature Nanotechnology*, vol. 7, p. 602, 2012.
- [16] I. Dufour, S. M. Heinrich, and F. Josse, “Theoretical Analysis of Strong-Axis Bending Mode Vibrations for Resonant Microcantilever (Bio)Chemical Sensors in Gas or Liquid Phase,” *Microelectromechanical Systems, Journal of*, vol. 16, no. 1, pp. 44–49, 2007.
- [17] J. K. Sell, A. O. Niedermayer, S. Babik, and B. Jakoby, “Real-time monitoring of a high pressure reactor using a gas density sensor,” *Sensors and Actuators A: Physical*, vol. 162, no. 2, pp. 215 – 219, 2010.

- [18] B. Jakoby, R. Beigelbeck, F. Keplinger, F. Lucklum, A. Niedermayer, E. K. Reichel, C. Riesch, T. Voglhuber-Brunnmaier, and B. Weiss, “Miniaturized sensors for the viscosity and density of liquids—performance and issues,” *IEEE transactions on ultrasonics, ferroelectrics, and frequency control*, vol. 57, no. 1, pp. 111–120, 2010.
- [19] B. Jakoby and M. J. Vellekoop, “Physical Sensors for Liquid Properties,” *Sensors Journal, IEEE*, vol. 11, no. 12, pp. 3076–3085, 2011.
- [20] O. Cakmak, E. Ermek, N. Kilinc, G. Yaralioglu, and H. Urey, “Precision density and viscosity measurement using two cantilevers with different widths,” *Sensors and Actuators A: Physical*, vol. 232, pp. 141–147, 2015.
- [21] K. Waszczuk, T. Piasecki, K. Nitsch, and T. Gotszalk, “Application of piezoelectric tuning forks in liquid viscosity and density measurements,” *Sensors and Actuators B: Chemical*, vol. 160, no. 1, pp. 517–523, 2011.
- [22] Y. Liu, R. DiFoggio, K. Sanderlin, L. Perez, and J. Zhao, “Measurement of density and viscosity of dodecane and decane with a piezoelectric tuning fork over 298–448K and 0.1–137.9MPa,” *Sensors and Actuators A: Physical*, vol. 167, no. 2, pp. 347–353, 2011.
- [23] F. R. Blom, S. Bouwstra, M. Elwenspoek, and J. H. J. Fluitman, “Dependence of the quality factor of micromachined silicon beam resonators on pressure and geometry,” *Journal of Vacuum Science and Technology B*, vol. 10, no. 1, pp. 19–26, 1992.
- [24] B. N. Johnson and R. Mutharasan, “Biosensing using dynamic-mode cantilever sensors: A review,” *Biosensors and Bioelectronics*, vol. 32, no. 1, pp. 1–18, 2012.
- [25] N. V. Lavrik, M. J. Sepaniak, and P. G. Datskos, “Cantilever transducers as a platform for chemical and biological sensors,” *Review of scientific instruments*, vol. 75, no. 7, pp. 2229–2253, 2004.
- [26] C. Ziegler, “Cantilever-based biosensors,” *Analytical and bioanalytical chemistry*, vol. 379, no. 7-8, pp. 946–959, 2004.

- [27] I. Dufour and L. Fadel, “Resonant microcantilever type chemical sensors: Analytical modeling in view of optimization,” *Sensors and Actuators B: Chemical*, vol. 91, no. 1, pp. 353–361, 2003.
- [28] T. Ikehara, J. Lu, M. Konno, R. Maeda, and T. Mihara, “A high quality-factor silicon cantilever for a low detection-limit resonant mass sensor operated in air,” *Journal of Micromechanics and Microengineering*, vol. 17, no. 12, p. 2491, 2007.
- [29] M. Godin, A. K. Bryan, T. P. Burg, K. Babcock, and S. R. Manalis, “Measuring the mass, density, and size of particles and cells using a suspended microchannel resonator,” *Applied Physics Letters*, vol. 91, no. 12, p. 123121, 2007.
- [30] M. Khan, S. Schmid, P. E. Larsen, Z. J. Davis, W. Yan, E. H. Stenby, and A. Boisen, “Online measurement of mass density and viscosity of pL fluid samples with suspended microchannel resonator,” *Sensors and Actuators B: Chemical*, vol. 185, pp. 456–461, 2013.
- [31] T. P. Burg and S. R. Manalis, “Suspended microchannel resonators for biomolecular detection,” *Applied Physics Letters*, vol. 83, no. 13, pp. 2698–2700, 2003.
- [32] O. Cakmak, E. Ermek, N. Kilinc, S. Bulut, I. Baris, I. Kavakli, G. Yaralioglu, and H. Urey, “A cartridge based sensor array platform for multiple coagulation measurements from plasma,” *Lab on a Chip*, vol. 15, no. 1, pp. 113–120, 2015.
- [33] B. A. Bircher, L. Duempelmann, K. Renggli, H. P. Lang, C. Gerber, N. Bruns, and T. Braun, “Real-time viscosity and mass density sensors requiring microliter sample volume based on nanomechanical resonators,” *Analytical chemistry*, vol. 85, no. 18, pp. 8676–8683, 2013.
- [34] J. Lee, W. Shen, K. Payer, T. P. Burg, and S. R. Manalis, “Toward attogram mass measurements in solution with suspended nanochannel resonators,” *Nano letters*, vol. 10, no. 7, pp. 2537–2542, 2010.
- [35] S. Sawano, T. Arie, and S. Akita, “Carbon Nanotube Resonator in Liquid,” *Nano Letters*, vol. 10, no. 9, pp. 3395–3398, 2010.

- [36] M. Kucera, *Performance of cantilever-based piezoelectric MEMS resonators in liquid environment*. Intitute for Sensor and Actuator Systems, TU Verlag: TU Wien, 2017. ISBN: 9783903024533.
- [37] M. Kucera, E. Wistrela, G. Pfusterschmied, V. Ruiz-Díez, T. Manzanegue, J. Hernando-García, J. L. Sánchez-Rojas, A. Jachimowicz, J. Schalko, A. Bittner, and U. Schmid, “Design-dependent performance of self-actuated and self-sensing piezoelectric-AlN cantilevers in liquid media oscillating in the fundamental in-plane bending mode,” *Sensors and Actuators B: Chemical*, vol. 200, no. 0, pp. 235–244, 2014.
- [38] M. Kucera, E. Wistrela, G. Pfusterschmied, V. Ruiz-Díez, T. Manzanegue, J. Luis Sánchez-Rojas, J. Schalko, A. Bittner, and U. Schmid, “Characterization of a roof tile-shaped out-of-plane vibrational mode in aluminum-nitride-actuated self-sensing micro-resonators for liquid monitoring purposes,” *Applied Physics Letters*, vol. 104, no. 23, p. 233501, 2014.
- [39] M. Kucera, E. Wistrela, G. Pfusterschmied, V. Ruiz-Díez, J. L. Sánchez-Rojas, J. Schalko, A. Bittner, and U. Schmid, “Characterisation of multi roof tile-shaped out-of-plane vibrational modes in aluminium-nitride-actuated self-sensing micro-resonators in liquid media,” *Applied Physics Letters*, vol. 107, no. 5, p. 053506, 2015.
- [40] J. E. Sader, “Frequency response of cantilever beams immersed in viscous fluids with applications to the atomic force microscope,” *Journal of Applied Physics*, vol. 84, no. 1, pp. 64–76, 1998.
- [41] W. Thomson, *Theory of vibration with applications*. CRC Press, 1996. ISBN: 0748743804.
- [42] B. C. Stipe, H. J. Mamin, T. D. Stowe, T. W. Kenny, and D. Rugar, “Non-contact Friction and Force Fluctuations between Closely Spaced Bodies,” *Physical Review Letters*, vol. 87, no. 9, p. 096801, 2001.
- [43] A. N. Cleland and M. L. Roukes, “External control of dissipation in a nanometer-scale radiofrequency mechanical resonator,” *Sensors and Actuators A: Physical*, vol. 72, no. 3, pp. 256–261, 1999.

- [44] L. B. Freund and G. Herrmann, “Dynamic Fracture of a Beam or Plate in Plane Bending,” *Journal of Applied Mechanics*, vol. 43, no. 1, pp. 112–116, 1976.
- [45] W. Heywang, K. Lubitz, and W. Wersing, *Piezoelectricity: evolution and future of a technology*, vol. 114. Springer Science und Business Media, 2008. ISBN: 3540686835.
- [46] S. Yoshio, N. Tokihiro, Y. Tsuyoshi, U. Masanori, and M. Tsutomu, “Development of Piezoelectric Thin Film Resonator and Its Impact on Future Wireless Communication Systems,” *Japanese Journal of Applied Physics*, vol. 44, no. 5R, p. 2883, 2005.
- [47] S. Moheimani and A. Fleming, *Piezoelectric Transducers for Vibration Control and Damping*. Springer London, 2006. ISBN: 9781846283321.
- [48] A. Gupta and S. Arora, *Industrial Automation and Robotics*. University Science Press, 2009. ISBN: 9788131805923.
- [49] K. K. Shung, J. M. Cannata, and Q. F. Zhou, “Piezoelectric materials for high frequency medical imaging applications: A review,” *Journal of Electroceramics*, vol. 19, no. 1, pp. 141–147, 2007.
- [50] J. Curie and P. Curie, “Développement, par pression, de l’électricité polaire dans les cristaux hémihédres à faces inclinées,” *Comptes rendus*, vol. 91, pp. 294–295, 1880.
- [51] J. Curie and P. Curie, “Contractions et dilatations produites par des tensions électriques dans les cristaux hémihédres à faces inclinées,” *Compt. Rend.*, vol. 93, pp. 1137–1140, 1881.
- [52] W. Hankel, “Ueber die actino- und piezoelectrischen Eigenschaften des Bergkrystalles und ihre Beziehung zu den thermoelectrischen,” *Annalen der Physik*, vol. 253, no. 9, pp. 163–175, 1882.
- [53] C. Constantin and L. Paul, “Production of submarine signals and the location of suemarine objects.” Patent, 1923.
- [54] M. D. Williams, B. A. Griffin, T. N. Reagan, J. R. Underbrink, and M. Sheplak, “An AlN MEMS Piezoelectric Microphone for Aeroacoustic

- Applications,” *Journal of Microelectromechanical Systems*, vol. 21, no. 2, pp. 270–283, 2012.
- [55] R. Elfrink, T. M. Kamel, M. Goedbloed, S. Matova, D. Hohlfeld, Y. v. Anandel, and R. v. Schaijk, “Vibration energy harvesting with aluminum nitride-based piezoelectric devices,” *Journal of Micromechanics and Microengineering*, vol. 19, no. 9, p. 094005, 2009.
- [56] N. Sinha, G. E. Wabiszewski, R. Mahameed, V. V. Felmetzger, S. M. Tanner, R. W. Carpick, and G. Piazza, “Piezoelectric aluminum nitride nanoelectromechanical actuators,” *Applied Physics Letters*, vol. 95, no. 5, p. 053106, 2009.
- [57] C. HeeChan, U. SoonChul, Y. ManSoon, and Y. SeungHwan, “Dependence of material properties on piezoelectric microspeakers with AlN thin film,” in *Nano/Micro Engineered and Molecular Systems 2008*. NSPEC Accession Number: 9964109.
- [58] G. Heckmann, *Die Gittertheorie der festen Körper*, pp. 100–153. Springer, Berlin, Heidelberg, 1925. ISBN: 9783642938597.
- [59] L. Fu and C. L. Kane, “Topological insulators with inversion symmetry,” *Physical Review B*, vol. 76, no. 4, p. 045302, 2007.
- [60] F. Martin, P. Muralt, M. A. Dubois, and A. Pezous, “Thickness dependence of the properties of highly c-axis textured AlN thin films,” *J. Vac. Sci. Technol. A*, vol. 22, no. 2, pp. 361–365, 2004.
- [61] P. Muralt, J. Antifakos, M. Cantoni, R. Lanz, and F. Martin, “Is there a better material for thin film BAW applications than AlN?,” in *IEEE Ultrasonics Symposium, 2005.*, vol. 1, pp. 315–320.
- [62] X. Song, R. Fu, and H. He, “Frequency effects on the dielectric properties of AlN film deposited by radio frequency reactive magnetron sputtering,” *Microelectronic Engineering*, vol. 86, no. 11, pp. 2217–2221, 2009.
- [63] N. D. Patel and P. S. Nicholson, “High frequency, high temperature ultrasonic transducers,” *NDT International*, vol. 23, no. 5, pp. 262–266, 1990.

- [64] S.-R. Jian and J.-Y. Juang, "Indentation-induced mechanical deformation behaviors of AlN thin films deposited on c-plane sapphire," *J. Nanomaterials*, vol. 2012, pp. 36–36, 2012.
- [65] S. Hiboux and P. Muralt, "Piezoelectric and dielectric properties of sputter deposited (111), (100) and random-textured $\text{Pb}(\text{Zr}_x\text{Ti}_{1-x})\text{O}_3$ (PZT) thin films," *Ferroelectrics*, vol. 224, no. 1, pp. 315–322, 1999.
- [66] X. B. Wang, C. Song, D. M. Li, K. W. Geng, F. Zeng, and F. Pan, "The influence of different doping elements on microstructure, piezoelectric coefficient and resistivity of sputtered ZnO film," *Applied Surface Science*, vol. 253, no. 3, pp. 1639–1643, 2006.
- [67] M.-Y. Han and J.-H. Jou, "Determination of the mechanical properties of r.f.-magnetron-sputtered zinc oxide thin films on substrates," *Thin Solid Films*, vol. 260, no. 1, pp. 58–64, 1995.
- [68] K. Yim and C. Lee, "Dependence of the electrical and optical properties of sputter-deposited ZnO:Ga films on the annealing temperature, time, and atmosphere," *Journal of Materials Science: Materials in Electronics*, vol. 18, no. 4, pp. 385–390, 2007.
- [69] S. Watanabe, T. Fujiu, and T. Fujii, "Effect of poling on piezoelectric properties of lead zirconate titanate thin films formed by sputtering," *Applied Physics Letters*, vol. 66, no. 12, pp. 1481–1483, 1995.
- [70] M. Sakata, S. Wakabayashi, H. Goto, H. Totani, M. Takeuchi, and T. Yada, "Sputtered high $|d_{31}|$ coefficient PZT thin film for microactuators," in *Proceedings of Ninth International Workshop on Micro Electromechanical Systems 1996*, pp. 263–266.
- [71] F. S. Mahmood, R. D. Gould, A. K. Hassan, and H. M. Salih, "D.c. properties of ZnO thin films prepared by r.f. magnetron sputtering," *Thin Solid Films*, vol. 270, no. 1, pp. 376–379, 1995.
- [72] I. T. Tang, Y. C. Wang, W. C. Hwang, C. C. Hwang, N. C. Wu, M.-P. Houn, and Y.-H. Wang, "Investigation of piezoelectric ZnO film deposited on diamond like carbon coated onto Si substrate under different sputtering conditions," *Journal of Crystal Growth*, vol. 252, no. 1, pp. 190–198, 2003.

- [73] I. B. Kobiakov, "Elastic, piezoelectric and dielectric properties of ZnO and CdS single crystals in a wide range of temperatures," *Solid State Communications*, vol. 35, no. 3, pp. 305–310, 1980.
- [74] N. Ledermann, P. Muralt, J. Baborowski, S. Gentil, K. Mukati, M. Cantoni, A. Seifert, and N. Setter, "(100)-textured, piezoelectric $\text{Pb}(\text{Zr}_x\text{Ti}_{1-x})\text{O}_3$ thin films for MEMS: integration, deposition and properties," *Sensors and Actuators A: Physical*, vol. 105, no. 2, pp. 162–170, 2003.
- [75] J. Gardeniers, Z. Rittersma, and G. Burger, "Preferred orientation and piezoelectricity in sputtered ZnO films," *Journal of Applied Physics*, vol. 83, no. 12, pp. 7844–7854, 1998.
- [76] S. Tadigadapa and K. Mateti, "Piezoelectric MEMS sensors: state-of-the-art and perspectives," *Measurement Science and Technology*, vol. 20, no. 9, p. 092001, 2009.
- [77] O. Ambacher, "Growth and applications of Group III-nitrides," *Journal of Physics D: Applied Physics*, vol. 31, no. 20, p. 2653, 1998.
- [78] M. N. Yoder, "Wide bandgap semiconductor materials and devices," *IEEE Transactions on Electron Devices*, vol. 43, no. 10, pp. 1633–1636, 1996.
- [79] B. Stefan, B. Mats, C. Manolis, O. Christian, and O. J. Kjell, "Applications of Aluminium Nitride Films Deposited by Reactive Sputtering to Silicon-On-Insulator Materials," *Japanese Journal of Applied Physics*, vol. 35, no. 8R, p. 4175, 1996.
- [80] S. Strite and H. Morkoç, "GaN, AlN, and InN: A review," *Journal of Vacuum Science and Technology B: Microelectronics and Nanometer Structures Processing, Measurement, and Phenomena*, vol. 10, no. 4, pp. 1237–1266, 1992.
- [81] S. Kasap and P. Capper, *Springer Handbook of Electronic and Photonic Materials*. Springer, 2006. ISBN: 9780387291857.
- [82] W. Zhong Lin, "Zinc oxide nanostructures: growth, properties and applications," *Journal of Physics: Condensed Matter*, vol. 16, no. 25, p. R829, 2004.

- [83] M. J. Madou, *Fundamentals of Microfabrication: The Science of Miniaturization*. CRC Press, 2003.
- [84] A. L. Kholkin, N. A. Pertsev, and A. V. Goltsev, *Piezoelectricity and Crystal Symmetry*, pp. 17–38. Boston, MA: Springer US, 2008. ISBN: 9780387765402.
- [85] M.-A. Dubois and P. Muralt, “Properties of aluminum nitride thin films for piezoelectric transducers and microwave filter applications,” *Applied Physics Letters*, vol. 74, no. 20, pp. 3032–3034, 1999.
- [86] H. P. Loeb, C. Metzmacher, R. F. Milsom, P. Lok, F. van Straten, and A. Tuinhout, “RF Bulk Acoustic Wave Resonators and Filters,” *Journal of Electroceramics*, vol. 12, no. 1, pp. 109–118, 2004.
- [87] R. C. Turner, P. A. Fuierer, R. E. Newnham, and T. R. Shrout, “Materials for high temperature acoustic and vibration sensors: A review,” *Applied Acoustics*, vol. 41, no. 4, pp. 299 – 324, 1994.
- [88] B. Abdallah, S. Al-Khawaja, and A. Alkhawwam, “Electrical characteristics of insulating aluminum nitride MIS nanostructures,” *Applied Surface Science*, vol. 258, no. 1, pp. 419–424, 2011.
- [89] M. Bosund, T. Sajavaara, M. Laitinen, T. Huhtio, M. Putkonen, V. M. Airaksinen, and H. Lipsanen, “Properties of AlN grown by plasma enhanced atomic layer deposition,” *Applied Surface Science*, vol. 257, no. 17, pp. 7827–7830, 2011.
- [90] M.-A. Dubois and P. Muralt, “Stress and piezoelectric properties of aluminum nitride thin films deposited onto metal electrodes by pulsed direct current reactive sputtering,” *Journal of Applied Physics*, vol. 89, no. 11, pp. 6389–6395, 2001.
- [91] M. Salta, J. A. Wharton, P. Stoodley, S. P. Dennington, L. R. Goodes, S. Werwinski, U. Mart, R. J. K. Wood, and K. R. Stokes, “Designing biomimetic antifouling surfaces,” *Philosophical Transactions of the Royal Society A: Mathematical, Physical and Engineering Sciences*, vol. 368, no. 1929, pp. 4729–4754, 2010.

- [92] R. W. Fox, P. J. Pritchard, and A. T. McDonald, *Fox and McDonald's introduction to fluid mechanics*. Hoboken, NJ; Chichester: John Wiley and Sons, Inc. ; John Wiley, 2011. ISBN: 9780470547557.
- [93] C. A. Van Eysden and J. E. Sader, "Frequency response of cantilever beams immersed in compressible fluids with applications to the atomic force microscope," *Journal of Applied Physics*, vol. 106, no. 9, p. 094904, 2009.
- [94] U. S. Lindholm, D. D. Kana, W.-H. Chu, and H. N. Abramson, "Elastic Vibration Characteristics of Cantilever Plates in Water," *Journal of Ship Research*, vol. 9, no. 11, 1965.
- [95] W.-H. Chu, "Report No. 2," report, Southwest Research Institute, 1963.
- [96] C. A. V. Eysden and J. E. Sader, "Compressible viscous flows generated by oscillating flexible cylinders," *Physics of Fluids*, vol. 21, no. 1, p. 013104, 2009.
- [97] J. E. Sader, I. Larson, P. Mulvaney, and L. R. White, "Method for the calibration of atomic force microscope cantilevers," *Review of Scientific Instruments*, vol. 66, no. 7, pp. 3789–3798, 1995.
- [98] J. W. M. Chon, P. Mulvaney, and J. E. Sader, "Experimental validation of theoretical models for the frequency response of atomic force microscope cantilever beams immersed in fluids," *Journal of Applied Physics*, vol. 87, no. 8, pp. 3978–3988, 2000.
- [99] M. K. Ghatkesar, T. Braun, V. Barwich, J.-P. Ramseyer, C. Gerber, M. Hegner, and H. P. Lang, "Resonating modes of vibrating microcantilevers in liquid," *Applied Physics Letters*, vol. 92, no. 4, p. 043106, 2008.
- [100] C. Seeton, "Viscosity–temperature correlation for liquids," *Tribology Letters*, vol. 22, no. 1, pp. 67–78, 2006.
- [101] M. Kucera, F. Hofbauer, E. Wistrela, T. Manzanque, V. Ruiz-Díez, J. L. Sánchez-Rojas, A. Bittner, and U. Schmid, "Lock-in amplifier powered analogue Q-control circuit for self-actuated self-sensing piezoelectric MEMS resonators," *Microsystem Technologies*, vol. 20, no. 4-5, pp. 615–625, 2014.

- [102] MicroChemicalsGmbH, “Processing image reversal resist,” 2003.
- [103] S. Sze, *Semiconductor devices, physics and technology*. Wiley, 1985. ISBN: 9780471143239.
- [104] MicroChemicalsGmbH, “Lift-off Processes with Photoresists,” 2013.
- [105] G. Pfusterschmied, M. Kucera, E. Wistrela, T. Manzanque, V. Ruiz-Díez, J. L. Sánchez-Rojas, A. Bittner, and U. Schmid, “Temperature dependent performance of piezoelectric MEMS resonators for viscosity and density determination of liquids,” *Journal of Micromechanics and Microengineering*, vol. 25, no. 10, p. 105014, 2016.
- [106] M. Schneider, *Einfluss der Schichtdicke und der Substratvorbehandlung auf die elektro-mechanischen Eigenschaften von gesputterten Aluminiumnitrid-Dünnschichten*. TU Wien: Verlag Dr.Hut, 2014. ISBN: 9783843915694.
- [107] E. Wistrela, M. Schneider, A. Bittner, and U. Schmid, “Impact of the substrate dependent polarity distribution in c-axis oriented AlN thin films on the etching behaviour and the piezoelectric properties,” *Microsystem Technologies*, vol. 22, no. 7, pp. 1691–1700, 2016.
- [108] W. J. Marshall and G. A. Brigham, “Determining equivalent circuit parameters for low figure of merit transducers,” *Acoustics Research Letters Online*, vol. 5, no. 3, pp. 106–110, 2004.
- [109] G. Pfusterschmied, M. Kucera, V. Ruiz-Díez, A. Bittner, J. L. Sánchez-Rojas, and U. Schmid, “Multi roof tile-shaped vibration modes in mems cantilever sensors for liquid monitoring purposes,” in *Micro Electro Mechanical Systems (MEMS), 2015 28th IEEE International Conference on Micro Electro Mechanical Systems (MEMS)*, pp. 718–721, 2015.
- [110] I. Dufour, E. Lemaire, B. Caillard, H. Debéda, C. Lucat, S. M. Heinrich, F. Josse, and O. Brand, “Effect of hydrodynamic force on microcantilever vibrations: Applications to liquid-phase chemical sensing,” *Sensors and Actuators B: Chemical*, vol. 192, no. 0, pp. 664–672, 2014.

- [111] M. Heinisch, T. Voglhuber-Brunnmaier, E. K. Reichel, I. Dufour, and B. Jakoby, “Reduced order models for resonant viscosity and mass density sensors,” *Sensors and Actuators A: Physical*, vol. 220, pp. 76–84, 2014.
- [112] J. Toledo, V. Ruiz-Díez, G. Pfusterschmied, U. Schmid, and J. L. Sánchez-Rojas, “Calibration procedure for piezoelectric MEMS resonators to determine simultaneously density and viscosity of liquids,” *Microsystem Technologies*, vol. 24, no. 3, pp. 1423–1431, 2018.
- [113] A. W. Leissa, “The free vibration of rectangular plates,” *Journal of Sound and Vibration*, vol. 31, no. 3, pp. 257–293, 1973.
- [114] J. L. Sanchez-Rojas, J. Hernando, A. Donoso, J. C. Bellido, T. Manzaneeque, A. Ababneh, H. Seidel, and U. Schmid, “Modal optimization and filtering in piezoelectric microplate resonators,” *Journal of Micromechanics and Microengineering*, vol. 20, no. 5, p. 055027, 2010.
- [115] C. A. Van Eysden and J. E. Sader, “Frequency response of cantilever beams immersed in viscous fluids with applications to the atomic force microscope: Arbitrary mode order,” *Journal of Applied Physics*, vol. 101, no. 4, p. 044908, 2007.
- [116] G. Pfusterschmied, M. Kucera, E. Wistrela, W. Steindl, V. Ruiz-Diez, A. Bittner, J. L. Sanchez-Rojas, and U. Schmid, “Piezoelectric response optimization of multi roof tile-shaped modes in MEMS resonators by variation of the support boundary conditions,” in *18th International Conference on Solid-State Sensors, Actuators and Microsystems (TRANSDUCERS)*, pp. 969–972, 2015.
- [117] G. Pfusterschmied, M. Kucera, W. Steindl, T. Manzaneeque, V. Ruiz Díez, A. Bittner, M. Schneider, J. L. Sánchez-Rojas, and U. Schmid, “Roof tile-shaped modes in quasi free-free supported piezoelectric microplate resonators in high viscous fluids,” *Sensors and Actuators B: Chemical*, vol. 237, pp. 999–1006, 2016.
- [118] T. Manzaneeque, J. Hernando, L. Rodríguez-Aragón, A. Ababneh, H. Seidel, U. Schmid, and J. L. Sánchez-Rojas, “Analysis of the quality factor of AlN-actuated micro-resonators in air and liquid,” *Microsystem Technologies*, vol. 16, no. 5, pp. 837–845, 2010.

- [119] G. Pfusterschmied, M. Kucera, J. Toledo, W. Steindl, V. Ruiz Díez, A. Bittner, M. Schneider, J. L. Sanchez-Rojas, and U. Schmid, “Wine Fermentation Monitoring using piezoelectric MEMS Resonators,” in *20th International Conference on Miniaturized Systems for Chemistry and Life Sciences (μ TAS)*, pp. 1380–1381, 2016.
- [120] G. H. Fleet, *Wine microbiology and biotechnology*. CRC Press, 1993. ISBN: 0415278503.
- [121] F. Larue and S. Lafon-Lafourcade, “Survival factors in wine fermentation,” *Alcohol toxicity in yeasts and bacteria*, pp. 193–215, 1989.
- [122] E. Munoz and W. M. Ingledew, “Yeast hulls in wine fermentations—a review,” *Journal of Wine Research*, vol. 1, no. 3, pp. 197–209, 1990.
- [123] N. El Haloui, D. Picque, and G. Corrieu, “Alcoholic fermentation in wine-making: on-line measurement of density and carbon dioxide evolution,” *Journal of Food Engineering*, vol. 8, no. 1, pp. 17–30, 1988.
- [124] E. Nerantzis, P. Tataridis, I. Sianoudis, X. Ziani, and E. Tegou, “Wine-making process engineering on line fermentation monitoring—sensors and equipment,” *Sci. Technol.(e-JST)*, vol. 5, pp. 29–36, 2007.
- [125] K. Koukolitschek, “Verfahren und Vorrichtung zur präzisen Bestimmung der Alkoholkonzentration in Flüssigkeiten,” *German patent DE*, vol. 41, no. 38, p. 419, 1993.
- [126] M. A. Pérez, R. Muñiz, C. De La Torre, B. García, C. E. Carleos, R. Crespo, and L. M. Cárcel, “Impedance spectrometry for monitoring alcoholic fermentation kinetics under wine-making industrial conditions,” in *Proceedings of XIX IMEKO World Congress-Fundamental and Applied Metrology*, pp. 2574–2578, 2009.
- [127] R. Crespo, L. Cárcel, M. Pérez, I. Nevares, and M. Del Álamo, “Suitable at-line turbidity sensor for wine fermentation supervision,” in *Proceedings of International Conference on Food Innovation*, pp. 1–4, 2010.
- [128] N. Lamberti, L. Ardia, D. Albanese, and M. Di Matteo, “An ultrasound technique for monitoring the alcoholic wine fermentation,” *Ultrasonics*, vol. 49, no. 1, pp. 94–97, 2009.

- [129] P. Resa, L. Elvira, F. M. De Espinosa, R. González, and J. Barcenilla, “On-line ultrasonic velocity monitoring of alcoholic fermentation kinetics,” *Bioprocess and biosystems engineering*, vol. 32, no. 3, pp. 321–331, 2009.
- [130] J. M. Acevedo, J. D. Gandoy, A. Del Río Vázquez, C. M.-P. Freire, and M. L. Soria, “Plastic optical fiber sensor for real time density measurements in wine fermentation,” in *Instrumentation and Measurement Technology Conference Proceedings*, pp. 1–5, 2007.
- [131] C. Q. Graña and J. M. Acevedo, “Experiences in measuring density by fiber optic sensors in the grape juice fermentation process,” *Fundamental and Applied Metrology*, pp. 2579–2582, September, 2009.
- [132] A. Boisen, S. Dohn, S. S. Keller, S. Schmid, and M. Tenje, “Cantilever-like micromechanical sensors,” *Reports on Progress in Physics*, vol. 74, no. 3, p. 036101, 2011.
- [133] J. Toledo, T. Manzanque, V. Ruiz-Díez, F. Jiménez-Márquez, M. Kucera, G. Pfusterschmied, E. Wistrela, U. Schmid, and J. L. Sánchez-Rojas, “Out-of-plane piezoelectric microresonator and oscillator circuit for monitoring engine oil contamination with diesel,” in *SPIE Microtechnologies 2015*, vol. 9517, pp. 95170C–95170C–9, 2015.
- [134] J. Toledo, V. Ruiz-Díez, G. Pfusterschmied, U. Schmid, and J. L. Sánchez-Rojas, “Flow-through sensor based on piezoelectric MEMS resonator for the in-line monitoring of wine fermentation,” *Sensors and Actuators B: Chemical*, vol. 254, pp. 291–298, 2018.
- [135] J. Toledo, F. Jiménez-Márquez, J. Úbeda, V. Ruiz-Díez, G. Pfusterschmied, U. Schmid, and J. Sánchez-Rojas, “Piezoelectric MEMS resonators for monitoring grape must fermentation,” in *Journal of Physics: Conference Series 2016*, vol. 757, p. 012020, IOP Publishing.
- [136] F. Jiménez-Márquez, J. Vázquez, J. Úbeda, and J. L. Sánchez-Rojas, “High-resolution low-cost optoelectronic instrument for supervising grape must fermentation,” *Microsystem Technologies*, vol. 20, no. 4-5, pp. 769–782, 2014.